DEPARTMENT OF
LIFE SCIENCES

NOVA SCHOOL OF
SCIENCE & TECHNOLOGY

Cristina Mediavilla Tris Freitas
BSc in Biochemistry

Towards Differential Stroke Diagnostic at Point-Of-Care Based on Surface-Enhanced Raman Spectroscopy (SERS) Analysis

Master in Molecular Genetics and Biomedicine
NOVA University Lisbon
September, 2024

NOVA SCHOOL OF SCIENCE & TECHNOLOGY

DEPARTMENT OF LIFE SCIENCES

Towards Differential Stroke Diagnostic at Point-Of-Care Based on Surface-Enhanced Raman Spectroscopy (SERS) Analysis

Cristina Mediavilla Tris Freitas

BSc in Biochemistry

Supervisors: José Ricardo Ramos Franco Tavares
Associate Professor, NOVA University Lisbon
Helena Luísa de Araújo Vieira
Assistant Professor, NOVA University Lisbon

Examination Committee:

Chair: Name of the committee chairperson,
Full Professor, FCT-NOVA

Rapporteurs: Name of a rapporteur,
Associate Professor, Another University
Name of another rapporteur,
Assistant Professor, Another University

Adviser: Name of the adviser present in defense,
Associate Professor, University

Members: Yet another member of the committee,
Full Professor, Another University
Yet another member of the committee,
Assistant Professor, Another University

Master in Molecular Genetics and Biomedicine
NOVA University, Lisbon
September, 2024

Towards Differential Stroke Diagnostic at Point-Of-Care Based on Surface-Enhanced Raman Spectroscopy (SERS) Analysis

Para minha mãe, cujo amor e apoio deram-me asas para seguir os meus sonhos.

ACKNOWLEDGMENTS

I want to express my deepest gratitude to my supervisor, Professor Ricardo Franco, for welcoming me into his lab and for his unwavering support throughout this journey. Your guidance and encouragement have been fundamental in helping me complete this thesis with such passion and motivation. I am forever grateful for the time spent in your lab, where I not only grew academically but also learned the true value of working in harmony with others.

I would also like to extend my sincere thanks to my co-supervisor, Professor Helena Vieira. Although I spent less time in your lab, I always felt warmly welcomed, and every question I had was met with openness and care.

To both of you, thank you for being a fundamental part of my academic growth and for trusting me with this project. Your constructive feedback and guidance have been essential in pushing me to improve and strive for excellence. Every meeting was a valuable learning experience, and I am especially thankful for the opportunities beyond the thesis, such as attending conferences and becoming a lab advisor. These experiences taught me invaluable skills and offered insight into the hard work behind the scenes. The student who entered your labs leaves not only with more knowledge and critical thinking but also with a profound understanding of collaboration and teamwork.

I also want to thank my colleagues in the Bionano Lab: Nuno Ferreira and Simão Caracho from the master's program, Raquel L. Carvalho and Hugo Marques from undergraduate studies, and our Erasmus colleague, Oana Biro. The time we spent together was filled with constructive conversations that pushed me to grow and to bring out the best version of myself. Thank you for being more than just collaborators, for creating an environment where we could work productively while still finding time to share a laugh and enjoy each other's company. Even in the shorter interactions, I learned so much from each of you, both academically and culturally.

A special thanks also goes to the Molecular Disease Mechanisms Lab, for always welcoming me with smiles and jokes whenever I needed a break, and for being attentive and helpful whenever I needed.

My heartfelt gratitude goes to Dra. Maria Enea for synthesizing the silver nanostars and for always being available whenever we encountered any issues. I am also grateful to Professor Eulália Pereira, both from the LAQV REQUIMTE at University of Porto, for the invaluable feedback on my presentations and poster, always encouraging me to improve.

I would like to extend my thanks to Professor Hugo Águas for allowing me to use the Renishaw inVia™ confocal Raman microscope and for sharing his expertise, which helped me better understand the equipment. My gratitude also goes to Dra. Maíza Ozório for producing

the paper substrates and for always being available to answer any questions I had about the technique and substrates, offering helpful tips to improve my work.

I also deeply appreciate Professor César Laia and Nuno Basilio for granting us access to the Horiba DLS/Zeta equipment and ensuring its smooth operation. My thanks also extend to everyone I crossed paths with, specially at CENIMAT and at Lab 407, where the DLS is housed, for the helpful conversations and their constant availability whenever I needed assistance.

I would also like to thank Master Flávia Freitas and Professor Marco Silva for allowing me to use the PCA software and for taking the time to explain how this statistical world works.

I would also like to acknowledge the professors from these past years and present (from IEL to NOVA-FCT), who have shown me just how fascinating and curious life can be. Your passion for teaching and your help during my academic years have been a driving force in my journey, and as I near the completion of my master's degree, I carry each of you with me in this moment of accomplishment.

Finally, I want to express my deepest thanks to my Spanish and Portuguese family, and my friends. Even when I seemed calm, they understood my nerves and always had encouraging words to help me push forward. A special thanks to my mum—without her unwavering support, not just over this past year but throughout my entire life, none of this would have been possible. She understood every low moment and helped me through them, even during my most stressful times. If I've made it this far, it's because of her love, generosity, and her strength, helping me face my fears and conquer them.

.

"The meaning of life is to find your gift. The purpose of life is to give it away." (Pablo Picasso)

Abstract

Stroke presents a critical medical challenge, impacting cerebral arteries and disrupting essential blood flow. As the second leading cause of death worldwide, stroke affects around 12 million individuals annually. Accurate diagnosis of stroke type (ischemic and hemorrhagic) is crucial due to varying therapeutic approaches and misdiagnosis can lead to fatal outcomes. Moreover, differential diagnostic is only possible in hospital environment with imaging examens, which delays therapy onset. Given these challenges, there is increasing interest in developing rapid, reliable, and cost-effective diagnostic techniques for stroke for pre-hospital use. Surface-Enhanced Raman Spectroscopy (SERS) has emerged as a promising method for stroke diagnosis based on patient plasma. By utilizing silver nanostars (AgNS) to create intense Raman signals at 'hot spots', SERS enables sensitive detection of unique plasma sample fingerprints, offering a promising avenue for accurate diagnosis.

This study aims to lay the groundwork for a faster stroke diagnostic method using SERS, with the ultimate goal of developing a point-of-care test (PoCT) for stroke diagnosis through blood samples. The method involved mixing plasma samples with microliter volumes of AgNS colloid to form bioconjugates, which are then analyzed using SERS to generate distinct spectral fingerprints. Principal Component Analysis (PCA) was used to extract relevant features from the SERS spectra.

The first successful result was the optimization of bioconjugates formation, which was confirmed by increased hydrodynamic size and changes in electrophoretic mobility. Additionally, the characteristic spectral features of plasma bioconjugates were not masked by human serum albumin (HSA), the most abundant protein in plasma. Various substrates for bioconjugate application for SERS measuring, were also tested and optimized, with aluminium foil and photocopy paper producing the most reliable and intense signals. Optimization of parameters, including the plasma-to-AgNS ratio, resulted in improved spectral patterns, namely: narrow bands, low background noise, and clearly measurable peak areas. Notably, 15 minutes of incubation of AgNS and plasma was sufficient for generating spectrum, highlighting the potential of this approach for rapid diagnostics. This was also observed when samples containing varying levels of Glial Fibrillary Acidic Protein (GFAP), a hemorrhagic stroke biomarker. PCA successfully distinguished between plasma, HSA and plasma albumin-free samples.

Overall, these findings provide a solid foundation for advancing SERS-based diagnostics in pre-hospital settings, ultimately improving patient outcomes through timely and accurate stroke identification.

Keywords: Bioconjugates, Human Serum Albumin (HSA), Surface-Enhanced Raman Spectroscopy (SERS), Human plasma, Stroke, Silver Nanostars (AgNS), Protein corona.

Resumo

O acidente vascular cerebral (AVC) apresenta um desafio médico crítico, afetando as artérias cerebrais e interrompendo o fluxo sanguíneo essencial. Sendo a segunda causa de morte em todo o mundo, o AVC afeta cerca de 12 milhões de indivíduos anualmente. Um diagnóstico preciso do tipo de AVC (isquémico e hemorrágico) é crucial devido às diferentes abordagens terapêuticas, e um diagnóstico incorreto pode levar a desfechos fatais. Além disso, o diagnóstico diferencial só é possível em ambientes hospitalares com recurso a exames de imagem, o que retarda o início da terapia. Dadas estas dificuldades, existe um interesse crescente no desenvolvimento de técnicas de diagnóstico rápidas, fiáveis e custo-efetivas para o AVC, destinadas a uso pré-hospitalar. A Espectroscopia de Raman Aumentada por Superfície (SERS) surgiu como um método promissor para o diagnóstico de AVC baseado em plasma de pacientes. Ao utilizar nanoestrelas de prata (AgNS) para criar sinais Raman intensos em "pontos quentes", SERS permite a deteção sensível de impressões digitais únicas em amostras de plasma, oferecendo uma via promissora para um diagnóstico preciso.

Este estudo tem como objetivo estabelecer as bases para um método de diagnóstico mais rápido para o AVC, com a meta final de desenvolver uma plataforma de teste de rastreio (PoCT) utilizando amostras de sangue. O método consistiu na mistura de amostras de plasma com volumes, na ordem dos microlitros, de AgNS para formar bioconjugados, que foram depois analisados usando SERS para gerar impressões digitais espectrais distintas. A Análise de Componentes Principais (PCA) foi utilizada para extrair características relevantes dos espectros SERS.

O primeiro resultado bem-sucedido foi a otimização da formação de bioconjugados, confirmada pelo aumento do tamanho hidrodinâmico e por mudanças na mobilidade eletroforética. Além disso, as características espectrais distintas dos bioconjugados de plasma não foram ocultas pela albumina sérica humana (HSA), a proteína mais abundante no plasma. Foram testados e otimizados vários substratos para a aplicação de bioconjugados na medição SERS, sendo que o papel de alumínio e o papel de fotocópia produziram os sinais mais fiáveis e intensos. A otimização de parâmetros, incluindo a razão plasma, resultou em padrões espectrais melhorados, caracterizados por bandas estreitas, baixo ruído de fundo e áreas de picos claramente mensuráveis. Notavelmente, 15 minutos de incubação de AgNS com plasma foram suficientes para gerar espectros, destacando o potencial desta abordagem para diagnósticos rápidos. Isso também foi observado em amostras contendo níveis variados de proteína ácida glial fibrilar (GFAP), um biomarcador de AVC hemorrágico. A PCA consegui distinguir com sucesso entre amostras de plasma, HSA e a plasma sem albumina.

De um modo geral, estes resultados fornecem uma base sólida para o avanço de diagnósticos baseados em SERS em contextos pré-hospitalares, melhorando, em

última análise, os resultados dos pacientes através da identificação oportuna e precisa de acidentes vasculares cerebrais.

Palavras-chaves: Bioconjugados, Albumina sérica humana (HSA), Espectroscopia de Raman aumentada pela superfície (SERS), Plasma humano, Acidente vascular cerebral (AVC), Nanoestrelas de prata (AgNS), Coroa proteica.

CONTENTS

List of Figures

List of Tables

ACRONYMS

AGE	Agarose Gel Electrophoresis
AI	Artificial Intelligence
AIS	Acute Ischemic Stroke
AgNPs	Silver Nanoparticles
AgNSs	Silver Nanostars
APS	Ammonium Persulfate
AuNS	Gold Nanostars
AVMs	Arteriovenous Malformations
BBB	Blood Brain Barrier
BCA	Bicinchoninic Acid
CCD	Charge-Coupled-Device
CM	Chemical Mechanism
CNN	Convolutional Neural Networks
CT	Computed Tomography
DA	Discrimination Analysis
DLS	Dynamic Light Scattering
EF	Enhancement Factor
EM	Electromagnetic Mechanism
EVT	Endovascular Therapy
GFAP	Glial Fibrillary Acidic Protein
HS	Hemorrhagic Stroke
HSA	Human Serum Albumin
ICH	Intracerebral Hemorrhage
IS	Ischemic Stroke
KPB	Potassium Phosphate Buffer
MBA	Mercaptobenzoic acid

MM	Molecular Markers
ML	Machine Learning
MRI	Resonance Imaging
MW	Molecular Weight
LMWM	Lower Molecular Weight Markers
LSPR	Localized Surface Plasmon Resonance
PCA	Principal Component Analysis
PDI	Polydispersity Index
PoC	Point-of-care
PLS-DA	Partial Least Squares- Discriminant Analysis
ROS	Reactive Oxygen Species
SAH	Subarachnoid Hemorrhage
SD	Standard Deviation
SDS-PAGE	Sodium Dodecyl-Sulfate PolyAcrylamide Gel Electrophoresis
SERS	Surface Enhanced Raman Spectroscopy
SM	Stroke Mimics
SPR	Surface Plasmon Resonance
SVMs	Support Vector Machine
TAE	Tris-acetate-EDTA
TEM	Transmission Electron Microscope
TBI	Traumatic Brain Injury
TEMED	TEtraMethylEthyleneDiamine
TIA	Transient Ischemic Attack
tPA	Tissue Plasminogen Activator

SYMBOLS

Δμ	Variations relative to the maximum mobility band
E	Electrical field
ε	Extinction molar coefficient
K_D	Dissociation constant
V	Velocity
$D(h)$	Hydrodynamic diameter
k	Boltzmann constant
T	Absolute temperature
n	Viscosity
Dt	Translational diffusion coefficient

1. Introduction

1.1 Stroke

When considering the complexity of human brain, stroke arises as a significant medical concern affecting vessels and blood perfusion. The brain is responsible for the control of motor actions, memory, cognition, hormones, including emotional regulation, speech, and manages essential functions such as breathing, digestion, among others. The brain relies on a continuous supply of oxygen and nutrients carried through the bloodstream [1]. However, stroke disrupts this essential supply when cerebral arteries/arterioles become either blocked (ischemic stroke) or ruptured (hemorrhagic stroke). This leads to a reduction or cessation of brain blood perfusion, affecting the brain's proper function. [1], [2]

1.1.1 Impact of stroke

Stroke is the second most prevalent cause of death worldwide, affecting approximately 12 million people annually. [3], [4] It significantly contributes to both mortality and morbidity rates in developing as well as developed countries. [5] Moreover, stroke ranks as the primary cause of adult-acquired disability. The extent and location of brain injury crucially affect the prognosis of stroke in terms of neurological impairments and long-term outcomes, such as impacting patients' functional recovery, quality of life and survival. [4], [5], [6] As the global population ages, the stroke burden is expected to rise, particularly in emerging nations due to the growing number of elderly individuals. [5], [7]

Figure 1 illustrates the critical steps in responding to stroke, emphasizing the importance of time. It begins at home, where stroke symptoms are first recognized. The next step is to call an ambulance for rapid transport to a hospital. A brain scan is necessary upon hospital arrival to accurately diagnose the type and extent of the brain injury and to determine the most appropriate treatment. The overlaid clock on the brain symbolizes urgency, as each step must be completed swiftly to improve patient outcomes. Beyond the health impact, stroke also poses significant socioeconomic burdens and challenges in healthcare management. [5], [6]

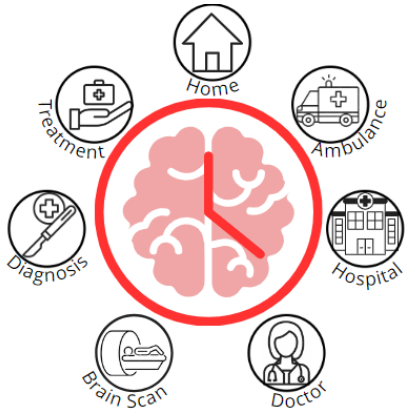

Figure 1. Importance of timely intervention in stroke care. This figure illustrates the essential steps: recognizing stroke symptoms, contacting an ambulance, transporting the patient to emergency care at the appropriate hospital, consulting with a doctor, undergoing a brain scan for diagnosis, and initiating treatment. Created in Canva.com.

Beyond the broader global context, the situation in Portugal offers a significant example of stroke's impact. According to a study conducted by *Sousa-Uva et al.* published in the '*Boletim Epidemiológico*' of the '*Instituto Nacional de Saúde, Doutor Ricardo Jorge*,' crucial insights were revealed. [8] Notably, in Portugal, stroke stands as the primary cause of death and disability (Figure 2). Every hour, three individuals in Portugal experience a stroke, with one not surviving, and half of those who do face severe consequences, making stroke a significant contributor to adult disability in the country. This positions stroke as a significant contributor to adult disability in Portugal, mirroring the global trend of stroke as a major driver of disability due to cerebral infarction. This highlights the need for increased awareness and effective healthcare strategies to mitigate its impact. [8], [9]

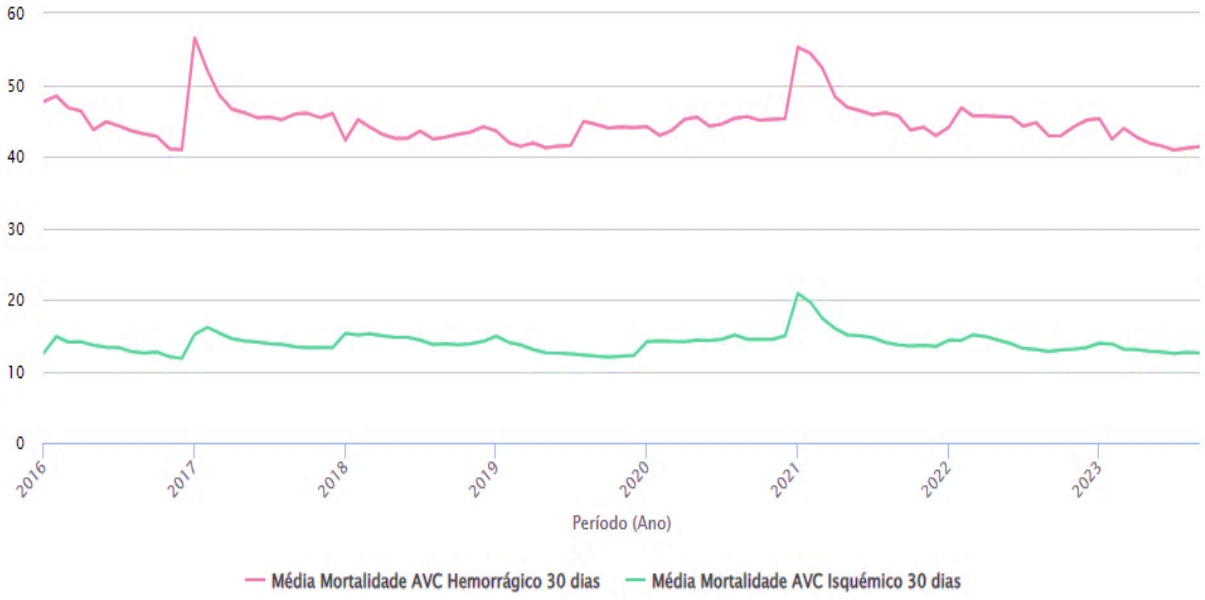

Figure 2. Average mortality from hemorrhagic and ischemic stroke each month from January 1, 2016, to October 29, 2023. The death rate from hemorrhagic stroke (pink) is higher and more irregular, with peaks in 2017 and 2021. The mortality rate from ischemic stroke (green) is lower and more consistent, with a notable peak in 2021. Peaks in 2021 are mostly related to the COVID-19 pandemic. Adapted from [10].

As highlighted by the statistics, it is important to promote the development of improved methods for diagnosis and therapy. The likelihood of experiencing a stroke increases the risk of subsequent occurrences. [11] This underscores the necessity of developing point-of-care testing (PoCT) solutions for stroke diagnosis in ambulances, which can facilitate timely and effective treatment. Importantly, 80% of strokes are preventable through effective management of risk factors. [1], [12] Thus, recognizing and controlling these risk factors is essential for lowering the incidence of stroke and enhancing patient outcomes.

1.1.2 Causes of stroke

Understanding the causes of stroke is essential for effective prevention and management, as both modifiable and non-modifiable factors significantly influence stroke risk and prognosis. For instance, the risk of stroke increases progressively every ten years after the age of 55. [1], [6], [13] In addition to these non-modifiable factors, several modifiable factors (Figure 3) such as hypertension, diabetes mellitus, atrial fibrillation, hypercholesterolemia, excessive alcohol consumption, and smoking, can increase the risk of stroke. Hypertension, for example, impairs vascular function and blood flow regulation, thereby elevating stroke risk. Similarly, diabetes increases risk due to high blood glucose levels, inflammation, and arterial wall damage, which can lead to the development of thrombotic lesions in the brain. [1], [6], [13]

Figure 3. Some risk factors for Stroke, including high blood cholesterol, obesity, high blood pressure, stress, diabetes, smoking, alcohol, and certain medications. Created in Canva.com.

1.1.3 Types of Stroke

There are two primary types of Stroke, determined by what is obstructing the flow of blood to the brain: ischemic and hemorrhagic (Figure 4). Nearly 85% of strokes are ischemic strokes (IS), a condition where blood clots or plaque (fatty deposits in artery walls) block or reduce the blood supply to the brain. [1], [2] In IS, blood clot can form in the neck vessels, break off, and obstruct brain blood vessels. The most common causes of IS are embolism, intracranial atherosclerosis, cervical artery dissection, and arterial inflammation. [6]

IS can be classified in three primary types based on the underlaying mechanisms of obstruction: thrombus, embolus, and atherosclerosis. Thrombus formation occurs when a blood clot develops in response to vessel injury or the presence of atherosclerotic lesions. This clot obstructs blood flow, thereby precipitating a stroke. Embolus refers to a blood clot or other fragments that travels from a distant part of the body to the brain, where it lodges in a cerebral artery. Emboli can originate from various sources, including cardiac, aortic, arterial, or peripheral circulation, and can also have an unknown origin. Embolic strokes are often considered the most severe form of IS due to their abrupt onset and potential for extensive brain damage. [2], [6] Atherosclerosis involves the progressive development of atherosclerotic plaques within the large arteries, such as the carotid artery. These plaques cause the narrowing of the arteries and are often caused due to the buildup of cholesterol or other substances.

[14], [15] Atherosclerosis of the carotid artery is a major cause of IS, accounting for 87% of all ischemic strokes. Acute Ischemic Stroke (AIS) refers to the early phase of IS, typically within the first 24-48 hours after the onset of stroke symptoms. AIS is characterized by immediate and severe symptoms, as wells as high risk of complications. [16]

Following AIS, one of the serious complications is hemorrhagic conversion, which can occur after the initial ischemic event or secondary to venous thrombosis, with reported rates of between 18 and 42%, respectively. [16], [17] Diagnosing this type of stroke can sometimes be challenging, as symptoms may overlap with those of other stroke types.

In contrasts to IS, hemorrhagic stroke (HS) constitutes the remaining 15% of stroke cases. [1] These strokes involve bleeding in or around the brain, usually due to the rupture or leakage of cerebral artery. HS can be further classified into two main types: subarachnoid hemorrhage (SAH) and intracerebral hemorrhage (ICH). [2]

A SAH happens when blood vessels on the brain's surface rupture and bleed into the space between the brain and the arachnoid membrane. SAH often results from a ruptured aneurysms or arteriovenous malformations (AVMs). In contrast, ICH occurs when blood vessels rupture within the brain tissue, often due to conditions that weaken the blood vessels, namely high blood pressure, anticoagulant therapy, diabetes, and aging. Hypertension-related deep perforating vasculopathy is a significant cause of ICH, where prolonged high blood pressure leads to the weakening and rupture of small penetrating arteries. This results in the accumulation of blood within the cerebral parenchyma, leading to mass effect, increased intracranial pressure, and subsequent neurological deficits. Both subtypes increase pressure on brain cells, leading to damage and death. [2], [6], [12]

Moreover, HS can occur due to traumatic brain injury (TBI). TBI-related strokes involve the physical disruption of blood vessels and brain tissue, potentially leading to sever complications and neurological deficits.

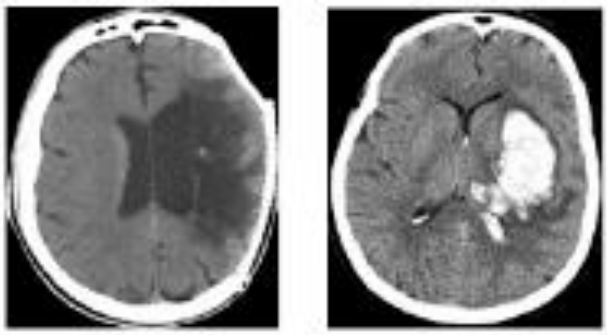

Figure 4. CT scan images showing a hemorrhagic stroke (left), indicated by a dark area, and ischemic stroke (right), indicated by a bright white area. Adapted from [18].

Furthermore, there is a related condition called Transient Ischemic Attack (TIA), which results in a brief disruption of blood supply to the brain, causing a mini-stroke.

TIAs can last for a few minutes to up to 24 hours, during which the blood clot either breaks up or a new path opens, restoring blood flow to the brain without causing permanent damage. Clinically, TIAs present stroke-like symptoms, such as sudden weakness or numbness on one side of the body, difficulty speaking, or visual disturbances. [2] Although the symptoms resolve completely within 24 hours, TIAs often indicate an increased risk of a full-blown stroke, they require immediate medical attention. Approximately 10-15% of patients with TIA will experience a major stroke within three months, half of these occurring the first 48 hours. [15], [19]

As demonstrated, the multifactorial nature of stroke etiology underscores the complexity inherent in its diagnosis and management, with various causes contributing to the condition. Moreover, distinguishing between actual strokes and stroke mimics (SM) is crucial in clinical practice due to the significant differences in their underlying causes and appropriate treatments. SM are conditions that present with symptoms similar to those of a stroke but are not caused by cerebrovascular events. SM refers to false-positive strokes, accounting for 30-40% of suspected stroke cases. In recent years, the incidence of mimics has risen, potentially due to an increased intake of suspected strokes in the new era of revascularization therapy. [20] Strokes primarily manifesting with visual symptoms are susceptible to misdiagnosis as mimics, such as migraine aura or ocular disorders. Similarly, early recognition of mimics is essential for ensuring timely and appropriate treatment. [20] Understanding the differences between various stroke types and distinguishing them from SM is essential for accurate diagnosis and ensuring that patients receive the correct treatment.

1.1.3.1 Cellular Consequences of Stroke

Several molecular pathways linked to stroke, including oxidative stress and inflammation, are involved in both hemorrhagic and ischemic types. [6], [12] Inflammation plays a critical role, particularly during acute and chronic phases (Figure 5), by activating various cell types such as astrocytes, microglia, leukocytes, and endothelial cells. Although this neuroinflammatory response aims to clear damaged cells and promote tissue healing, it can also exacerbate brain damage, hinder recovery, and increase the risk of complications like cognitive impairment and mobility issues. [6], [19]

Concurrently, oxidative stress, characterized by the excessive production of free radicals, significantly contributes to brain ischemia and reperfusion injury. The influx of calcium leads to an overproduction of reactive oxygen species (ROS), exacerbating cellular damage and disrupting the blood-brain barrier (BBB) through cell death. [6]

In the ischemic process, excitotoxicity and calcium overload further lead to neuronal death, with stressors such as plasma membrane breakdown and organelle swelling compounding the injury. Key pathological processes include inflammation, increased intracellular calcium, and the release of excitatory amino acids, all of which elevate ROS levels and contribute to mitochondrial dysfunction. [21], [22]

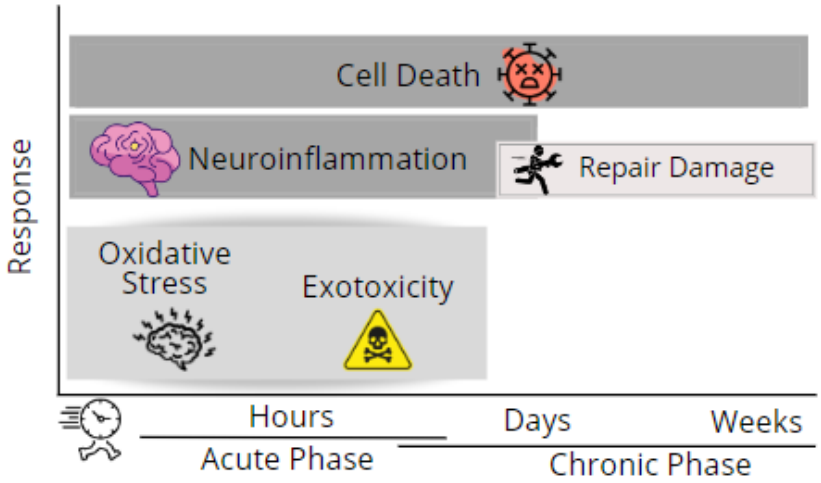

Figure 5. Cellular consequences of acute and chronic phase after a Stroke event. Created in Canva.com.

1.1.4 Treatment for Stroke patients

Immediate medical care is critical for a stroke patient, as delays in initiating treatment are associated with increased disability and mortality. [1] Several factors can cause delays, including failure to recognize stroke symptoms, ambulance transport delays, and the challenges in accurately diagnosing stroke types, which often require brain imaging techniques.

The treatment approach for stroke depends on whether the patient is experiencing an IS or a HS. For IS, the primary goal is to restored blood flow to the brain as quickly as possible. This can be achieved through intravenous thrombolysis with medications like recombinant tissue plasminogen activator (tPA) or endovascular therapy (EVT). These interventions must be administered within a specific time, 4.5 hours for tPA and 6 hours for EVT, to be effective. [6], [23] Certain treatments are only beneficial when delivered within a few hours of stroke onset, underscoring the importance of rapid diagnosis and intervention. [24], [25] In some cases, the time window for intervention can be extended if surrounding brain tissue remains viable. However, rapid reperfusion carries risks, including reperfusion injury and hemorrhagic conversion. For HS, the goal is to stop the bleeding and reduce brain pressure, requiring surgical interventions, particularly in SAH. [26], [27]

Accurate and swift diagnosis for differentiating between IS, HS and SMs is crucial for effective treatment. Non-contrast computed tomography (CT) is used to exclude HS from thrombolysis treatment, but it is often unavailable in prehospital settings and primary care hospitals. While MRI is more sensitive for detecting IS, its accessibility is often limited. [27], [28]

Misidentifying stroke types can result in inappropriate treatments and resource misallocation, highlighting the need for alternative diagnostic tests with high sensitivity and specificity. Early identification would enable emergency services to direct

patients to appropriate facilities, thereby improving outcomes and minimizing long-term disabilities associated with strokes. Point-of-care testing (PoCT) technology offers a potential solution, providing rapid results from blood samples within 5-20 minutes, which can be conducted in ambulances (Figure 6). [29], [30]

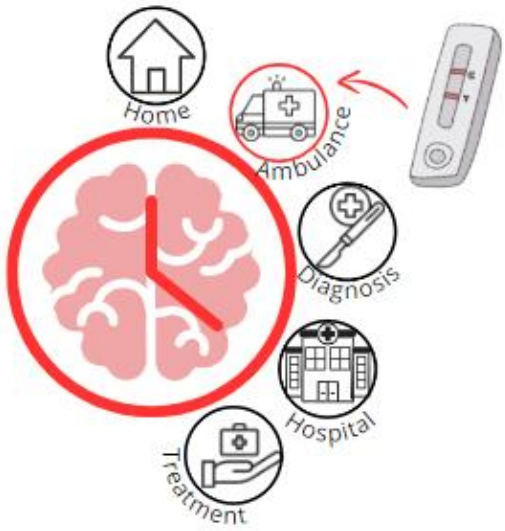

Figure 6. Timely intervention in stroke care can significantly reduce stoke diagnosis to 15-20 minutes. This figure illustrates the essential steps with the use of a PoCT available in the ambulance: recognizing stroke symptoms, contacting an ambulance, diagnosing the stroke type in the ambulance, transporting the patient to the appropriate hospital, and initiating treatment. Created in Canva.com.

Stroke is not just a one-time occurrence; the likelihood of experiencing another episode is higher after initial event. Stroke survivors may continue to suffer long-term neurological complications. [1] According to a study published by '*The American Heart Association, in conjunction with the National Institutes of Health*', 1 in 4 stroke survivors have another stroke within 5 years. [15], [16] It's also crucial to consider that the risk of having a stroke after a TIA is 17% higher. [15], [17] Moreover, stroke survivors require ongoing monitoring, as they have higher risk of subsequent strokes and long-term neurological complications. [15] Recent developments in stroke are still in fundamental and clinical research, exploring new avenues for treatment, including activity-based, drug-based, and cell-based therapies, along with rehabilitation and preventive measures. [6] Despite these advancements, further research into the underlying mechanisms, risk factors, and effective stroke diagnosis to ensure the correct stroke therapies is still needed.

1.1.5 Diagnosis

Given the significant burden of stroke, accurate and rapid diagnosis is essential, as treatments like reperfusion and endovascular therapy are highly time-dependent.

The concept “Time is brain” highlights the critical need for swift action, as delays in diagnosis can lead to worse outcomes. [23], [24]

Differentiating between IS and HS is essential, as misdiagnosing HS and administering treatments designed for IS, such as thrombolytics, can severely worsen the patient's condition and pose life-threatening risks. Incorrect treatment may exacerbate hemorrhaging, leading to catastrophic consequences. [26], [27]

Imaging modalities, including computed tomography (CT) and magnetic resonance imaging (MRI), are the most reliable methods for determining stroke type and etiology. [1], [12], [34] CT scans are typically the initial imaging step, critical for detecting hemorrhages, assessing stroke locations, and ruling out ICH early. However, CT has limitations, including reduced spatial resolution and contrast, which can result in underestimating infarct size, particularly in the early stages of ischemic stroke when lesions are less detectable. [24] While CT has an 89% sensitivity for hemorrhagic stroke, its sensitivity for ischemic stroke in the early stages is only 16%. [35]

MRI provides more detailed brain images and is often used in complex cases where the extent of damage is unclear. [36] However, MRI is slower and less practical in urgent situations due to its high cost, limited availability, and longer scan times. Around 20% of ischemic strokes may go undetected by MRI in early stages. [35]

Distinguishing between IS and HS is necessary to ensure appropriate treatment and efficient resource allocation. Routine diagnostics, such as CT and MRI scans, are the single accurate manner to differentiate between stroke types [37]. Although CT scans are frequently the first line of imaging, they have limitations in terms of early detection of IS and differentiating them from SMs. [38] MRIs, on the other hand, provide more detailed information but is less available and take longer to produce results. These challenges underscore the need for advanced diagnostic methods and broader access to these technologies in medical facilities.

Many hospitals, particularly in Portugal, face significant hurdles, including limited access to advanced diagnostic equipment and pathways such as ‘Via Verde’ that would enable prompt and accurate diagnosis. Furthermore, there is a shortage of specialized professionals, including neurologists and neuroradiologists (Figure 7). [39] This issue emphasizes the necessity of having a dispositive on hand in ambulances to identify the type of stroke and facilitate timely intervention.

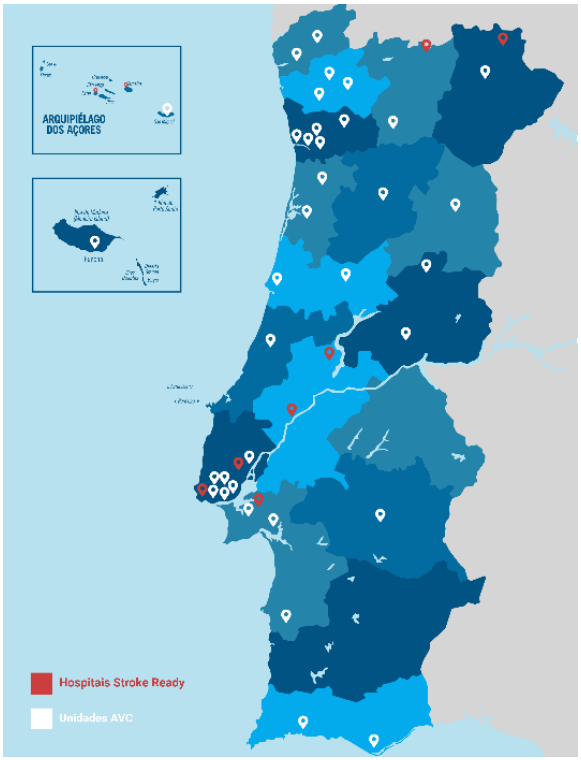

Figure 7. Map of Stroke Units and Stroke Ready Hospitals in Portugal. Stroke Units (white) are specialized hospitals areas with advanced resources and multidisciplinary teams for stroke care. Stroke Ready Hospitals (red) can diagnose and provide initial treatment for stroke but transfer patients needing specialized care. Adapted from [39].

Early diagnosis in the ambulance allows for more efficient patient management, ensuring that only those with confirmed strokes are sent to central hospitals, thereby optimizing resource allocation. Additionally, a future advantage could involve initiating treatment, such as thrombolytic therapy, directly in the ambulance, significantly reducing time to treatment and potentially improving patient outcomes. By starting therapy before hospital arrival, valuable time could be gained. This is crucial given the time-sensitive nature of stroke management, as previously emphasized by the saying 'Time is brain'. This concept underscores the critical importance of timely intervention, as approximately 1.9 million neurons and 14 billion synapses are lost every minute after stroke onset. Considering the neuronal loss induced by normal ageing, the brain ages by 3.6 years every hour following an artery occlusion. [23], [24], [38]

Despite the serious consequences of prompt medical intervention, developments in diagnostic technology, such as Raman spectroscopy, are essential to improving our capacity to handle situations like these.

1.2 Surface-Enhanced Raman Spectroscopy (SERS)

1.2.1 Principles of Raman Spectroscopy

Before exploring Surface-Enhanced Raman Spectroscopy (SERS), it is important to understand the foundational principles of Raman spectroscopy. In Raman spectroscopy, a monochromatic laser beam is directed at the sample, causing light to scatter in various directions. [40] While most photons undergo elastic (Rayleigh) scattering, retaining the same frequency as the incident light, Raman scattering involves a small percentage of photons gaining or losing energy due to interactions with molecular vibrations, resulting in frequency shifts related to molecular structure and sample composition. [40], [41], [42]

However, Raman spectroscopy has low sensitivity due to the small scattering cross-section of a single molecule, which refers to how likely a molecule is to scatter light. This limitation was overcome by the discovery of Surface-Enhanced Raman Spectroscopy (SERS), which significantly enhances sensitivity by amplifying Raman signals from molecules near conductive nanostructures (Figure 8). [40], [43], [44]

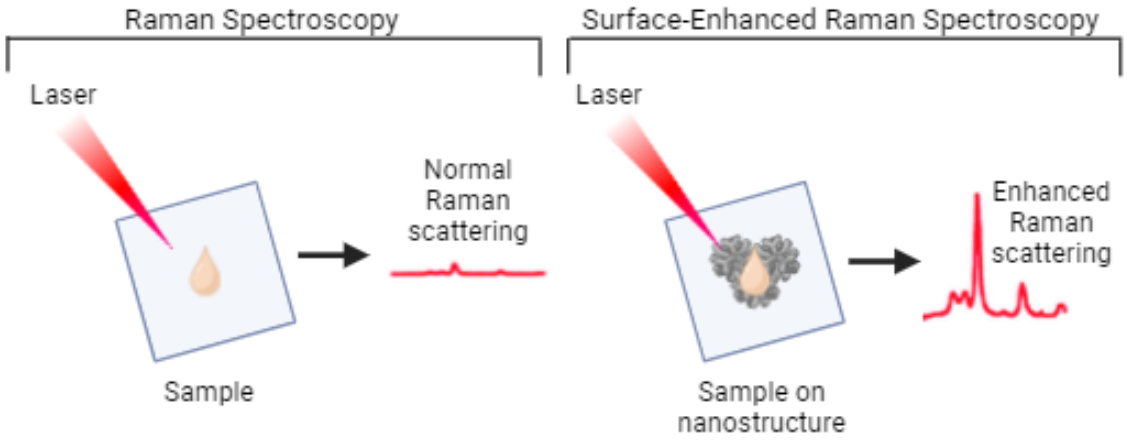

Figure 8. Comparison between Raman Spectroscopy and Surface-Enhanced Raman Spectroscopy. Enhanced Raman scattering derives from the metal nanostructures in direct contact with the sample. Created in Biorender.com.

1.2.2 Enhancements Mechanisms in SERS

Surface-Enhanced Raman Spectroscopy (SERS) significantly enhances Raman scattering of molecules adsorbed on nanostructured metallic surfaces, such as gold, silver, and cooper (Figure 9). [40], [45] This ultrasensitive, label-free analytical technique is very useful for detecting minimal quantities of materials, and finds application across a variety of areas, such as material science [46], environmental analysis [47], and biomedical diagnostics [48], [49].

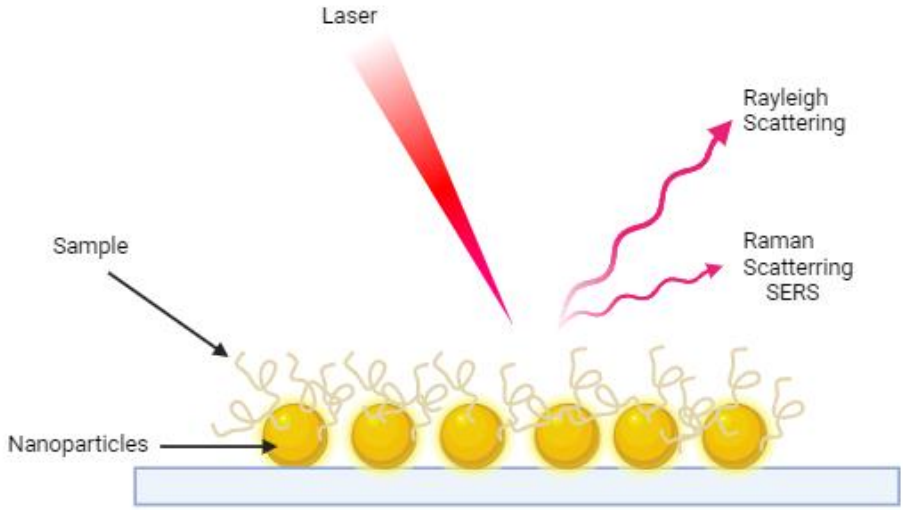

Figure 9. General representation of the SERS effect. Created in Biorender.com.

The intensity of Raman signals depends on factors such as the size, shape, and surface roughness of plasmonic nanostructures. [48] It is possible to synthesize and utilize a variety of nanoparticle morphologies, including nanorods, nanocubes, nanostars and nanospheres, to obtain SERS signals. [40] Each morphology may offer distinct advantages depending on the specific application, allowing for tailored approaches to enhance signal detection in SERS experiments.

SERS employs two mechanisms for signal enhancement: the electromagnetic mechanism (EM) and the chemical mechanism (CM) (Figure 10). EM is associated with surface plasmon resonances (SPRs), particularly with localized surface plasmon resonance (LSPR). LSPR occurs when the collective oscillation of valence electrons in a metal nanoparticle resonates with the frequency of incident light (Figure 10A). [41] This resonance concentrates electromagnetic energy near nanostructures, expanding the molecules' absorbance and emission cross-sections. [40], [50] When the frequency of incident light matches the oscillation of surface electrons, it creates a strong localized electric field, amplifying Raman scattering signals from molecules adsorbed onto or near the nanostructure surface. [41], [43], [44], [51], [52] SERS predominantly occurs at micro/nanometer-scale interstices or sharp features of materials, the so-called "hot spots". These hot spots, or nanogaps, utilize near-field scattering and LSPR to concentrate incident light into a very strong local electric field. [40], [48], [53] In addition, nanoparticle junctions and flat metal surfaces that enable plasmon resonances can also generate hot spots. The gap distance and other geometrical parameters have a significant influence on the resulting intensity of the Raman signal, with an approximate inverse relationship between the gap distance and the amplitude of the electromagnetic field. [44], [54]

The chemical mechanism (CM) involves charge transfer resonances, where adsorbed molecules experience changes in polarizability (Figure 10B). [40], [50] This shift induces charge transfer, particularly transitions between the lowest unoccupied

molecular orbital (LUMO) to the highest occupied molecular orbital (HOMO), enhancing the Raman signal. [54] Essentially, the interaction between the molecule and the metal surface facilitates charge transfer, which modifies the electronic structure of the adsorbed molecules, leading to an enhanced Raman signal, normally in the formation of a metal-molecule bond. [44], [54]

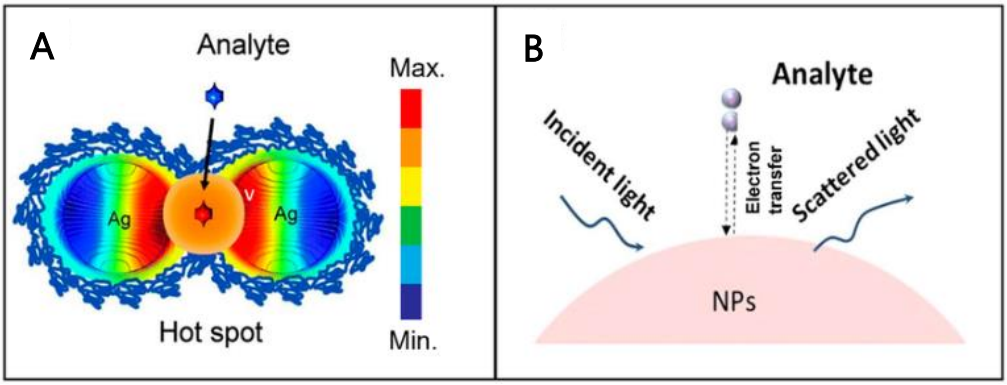

Figure 10. Mechanisms of SERS enhancement. **A.** Electromagnetic mechanism (EM): a "hot spot" is formed in the gap between two closely spaced nanoparticles, which leads to electromagnetic amplification in SERS-active silver nanoparticles. **B.** Chemical mechanism (CM) resulting from interactions between analytes and the surface of nanoparticles via electron transfer. Adapted from [55].

The overall enhancement factor (EF) of SERS is directly proportional to the intensity of the local electromagnetic field, which is determined by the nanogap distance between two metal nanoparticles, generating a significant EM hotspot when the EM's EF reaches an extremely high level. This EF is many orders of magnitude greater than the CM's EF, thereby affecting the performance of SERS devices. [45] The EF equation (Equation 1) is presented below:

$$EF = \frac{ISERS/CSERS}{IRaman\ /CRaman} \qquad \text{Equation 1}$$

where I_{SERS} and I_{Raman} represent the intensities of the SERS and Raman signals, respectively, and c_{SERS} and c_{Raman} denote the concentrations of molecules in the SERS and Raman experiments, respectively. [44], [56] The efficiency of this technique is reliant on the precise fabrication of nanostructures, as the EF of the Raman signal is influenced by the size and morphology of these nanostructures. [40]

1.2.3 Applications of SERS in Biomedical Diagnostics

SERS is a powerful technique for biomedical diagnostics, offering high sensitivity and flexibility in detecting and measuring biomolecules within complex biological samples. It can identify a wide range of biomolecules, including proteins, nucleic acids, and small metabolites, at low concentrations. This capability is important for the early detection of illnesses, as it allows for the identification of low-abundance biomarkers

in biological fluids such as blood, urine, and saliva, even amid interfering substances. [57], [58]

A significant challenge for global healthcare systems is the need for rapid diagnosis of medical conditions. SERS offers a promising solution to these challenges by enabling direct biomarker detection, making it an invaluable diagnostic tool. [48], [57] Its success has been particularly notable in identifying cancer biomarkers, which aids in early tumor detection and characterization. Additionally, SERS facilitates the monitoring of treatment effectiveness by providing real-time feedback on therapeutic progress. [57], [59]

However, challenges remain in the reproducibility and standardization of the SERS signal, which are closely related to the performance of SERS nanostructures. Developing reliable and sensitive SERS nanostructures that amplify Raman signals while minimizing background noise is particularly challenging in complex biomedical samples. Advancements in artificial intelligence (AI) and machine learning (ML) techniques are expected to improve detection limits, enable multiplex detection, and accelerate data analysis. [57], [60]

Moreover, the high sensitivity and rapid processing capabilities of SERS make it particularly suitable for point-of-care testing (PoCT). PoCT is characterized by quality-assured diagnostic services and analytical devices positioned near patients, as opposed to centralized equipped laboratories. The need for quick and reliable health assessments highlights the importance of easy-to-use PoCT solutions. Portable SERS devices enable on-site diagnostics, reducing the need for large laboratory settings. Advances in nanotechnology and microfabrication have facilitated the integration of diagnostic tools, allowing for real-time diagnosis and continuous monitoring. Point-of-care (PoC) diagnostics are critical for improving health outcomes, especially in resource-limited settings where access to hospitals or laboratory facilities is restricted. [61]

The role of nanomaterials in enhancing SERS signals and their applications in stroke diagnosis using plasma as a biofluid will be covered in more detail in the sections that follow.

1.3. Nanomaterials in SERS

1.3.1 Role of Nanomaterials in SERS

Nanomaterials, particularly those constructed from plasmonic metals, are responsible for the sensitivity and specificity of SERS. These nanostructures amplify Raman scattering signals from molecules adsorbed on their surfaces, enabling the detection of analytes at very low concentrations at room temperature. This capability makes SERS a powerful technique for structural analysis and detection across various fields,

including catalysis, biological molecule detention, drug delivery, photothermal therapy, and imaging. [62], [63]

Metallic nanoparticles (NPs), specifically gold (Au) and silver (Ag), are commonly used in SERS due to their LSPR properties. These properties can be fine-tuned by adjusting factors such as shape, size, composition, interparticle interactions and surface coatings, thereby enhancing Raman signal amplification. [64] These generates high electromagnetic fields necessary for advanced spectroscopy techniques. [65] For instance, silver nanostars (AgNS) colloid solutions can achieve EF on the order of 10^4 to 10^6. [44].

While spherical nanoparticles have been used to achieve large SERS enhancements, their performance can be limited without aggregation. Aggregation creates interparticle gaps that induce significant field intensifications but can reduce reproducibility. An alternative approach involves using anisotropic metal nanoparticles, such as nanostars, which exhibit strong plasmonic properties and do not require aggregation. [66] Nanostars, with their anisotropic shapes and sharp tips, generate multiple hot spots and exhibit broad SPR, making them particularly well-suited for biodiagnostics and chemical detection. [67], [53] Given these advantages, this Thesis employs an experimental setup utilizing plasma adsorbed to citrate-covered silver nanostars (Figure 11).

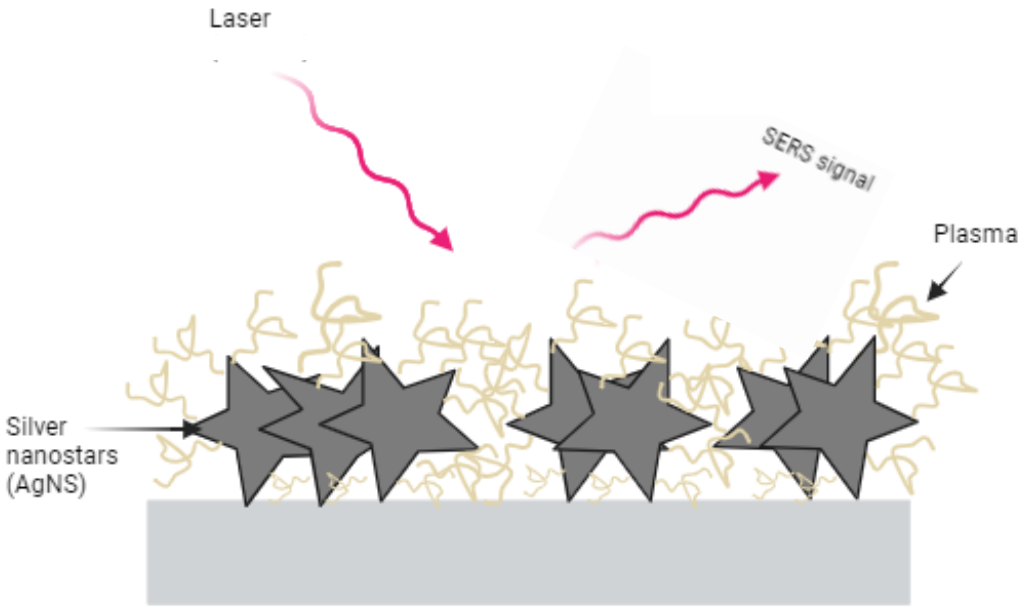

Figure 11. Schematic representation of SERS using AgNS for detection of biomarkers contained in blood plasma, the experimental setup studies in the present dissertation. Created in Biorender.com.

1.3.2 Silver Nanostars: Synthesis and Properties

Silver nanostars (AgNS) have emerged as highly effective SERS nanostructures due to their unique structural and plasmonic properties. Characterized by multiple

sharp branches or "arms", AgNS exhibit intense LSPR effects that significantly enhance the Raman signals of molecules adsorbed on their surfaces. [68], [69], [70]

Synthesis of AgNS typically involves chemical reduction processes that allow for precise control over the size, shape, and morphology of the nanoparticles. A common method is where silver nitrate ($AgNO_3$) serves as the precursor, releasing silver ions (Ag^+) into the solution. Reducing agents like trisodium citrate ($Na_3C_6H_5O_7$), which also acts as a stabilizer, facilitate the formation of silver nanoparticles. [69], [71] Other reducing agents such as $NaBH_4$, hydrazine, and ascorbate can also be used, with stronger reductants producing smaller, more uniform particles. [72]

The morphology of nanoparticles can be controlled by adjusting the temperature, pH, or reactant concentration, by adding complementary surfactants, or by exposing nanoparticles to various external stimuli including light, heat, and magnetic field. These factors significantly influence the EF of Raman signals. [69] Nanoparticles with sharp edges or angles can intensify the electric filed in high curvature regions, theoretically providing extra SERS enhancement (Figure 12B). [40]

The central spherical core of AgNS serves as an electron reservoir, while the acute tips concentrate the electromagnetic field at their apexes, creating "hot spots" that amplify SERS signals (Figure 12A). Aggregation of AgNS enhances SERS intensity [65], [68], [70], and their suitability for SERS applications is confirmed through the characterization of size, shape, and surface morphology. [68]

In this study [56], a significant EF of approximately 10^6 for the nanoplasmonic cardboard SERS substrate with a silver (Ag) mass thickness of 6 nm was achieved. This substantial enhancement is attributed to the optimal spectral alignment of the LSPR, which matches the excitation wavelength used in the SERS measurements. Notably, the localized near-field enhancement produced by AgNS is substantially higher than that of AgNPs. This is due to the overlapping near-field regions between adjacent AgNS, which significantly boosts the electric field intensity around the analyte molecules, thus increasing the SERS signal.

Additionally, coatings are used to prevent nanoparticle aggregation through electrostatic, steric, or electrostatic repulsive forces [69], [71]. The star-shaped morphology of AgNS, with their sharp tips, rough surfaces, and nanogaps, further enhances their plasmonic properties, especially around the 400 nm region, making them highly effective for biosensing and chemical detection applications. [73], [74]

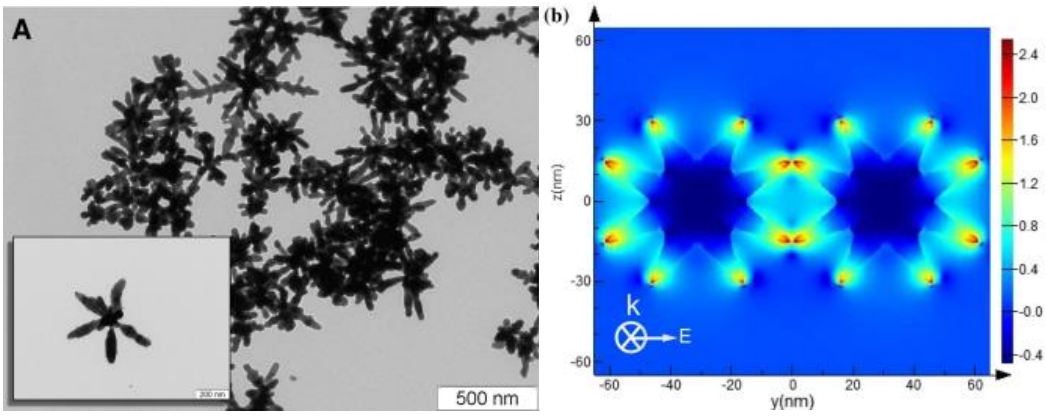

Figure 12. **A**. Silver nanostars colloid characterization by Transmission Electron Microscopy (TEM) micrographs. Adapted from [68]. **B**. Electromagnetic field distribution of nanostar dimer using 3D-FDTD method under 633 nm laser illumination. E: electric field; k: wave vector of incident light. Adapted from [75].

1.3.3 Substrates for Sample Measurement

In this work, we have employed innovative substrates for sample placement in SERS measurements that will improve the SERS signal and enhance the sensitivity of molecule detection. These are especially important parameters to improve for measurements in complex media like plasma.

Cellulose paper is emerging as a promising SERS substrate, offering a sustainable alternative to conventional rigid supports like glass, silicon wafers, and aluminium films. Its advantages include recyclability, biodegradability, and accessibility from renewable sources. Paper-based SERS devices benefit from paper's wicking capabilities, flexibility, porosity, and sample storage potential. Studies have shown that office paper provides better nanoparticle distribution and ink retention compared to filter paper (Whatman No. 1), leading to higher EF values. Cardboard has also been explored for efficient nanoplasmonic SERS applications. [53], [56]

When nanoparticles are drop-casted onto paper, its porous structure allows for uniform nanoparticle diffusion, enhancing SERS performance by creating hot spots. Office/Photocopy paper, with nanoparticles mainly on its surface, suppresses endogenous fluorescence and enhances sensitive SERS detection. Moreover, office paper coated with silver nanostars (AgNSs) is easy to produce, stable for long-term storage, and cost-effective, making it suitable for on-site diagnostics and environmental monitoring [53]

In contrast to traditional SERS methods, where liquid samples are deposited onto rigid substrates, recent advancements use inkjet printing to fabricate SERS substrates by depositing silver nanostructures onto paper. This method provides significant enhancement factors while maintaining the flexibility and cost advantages of paper. [76]

Paper-based microfluidics, which combine the simplicity of paper strip tests with the capabilities of lab-on-a-chip devices, are ideal for point-of-care diagnostics. These devices are inexpensive, easy to use, and well-suited for global healthcare due to their low cost and rapid on-site detection capabilities. [77] Additionally, filter paper-based SERS allows rapid processing of large analyte volumes by trapping and concentrating nanoparticles, significantly improving detection sensitivity compared to traditional techniques. [77]

In addition to these benefits, filter SERS allows for the rapid processing of large volumes of trace analyte samples, significantly increasing the number of analyte molecules that interact with the SERS-active surface. The filter membranes trap and concentrate nanoparticles from a colloid solution, improving detection performance by orders of magnitude compared to traditional methods. [78]

1.4. Biofluids in Diagnostic applications

Biofluids play a crucial role in medical diagnostics, offering a non-invasive or minimally invasive means to gather extensive information about an individual's health status. Commonly analyzed biofluids include entire blood, plasma, serum, urine, saliva, and cerebrospinal fluid. These fluids contain biomarkers that can provide insights into various physiological and pathological conditions, aiding in disease diagnosis; monitoring progression, and evaluating therapeutic outcomes. [60], [79], [80], [81], [82]

1.4.1 Biomarkers in Biofluids

Biomarkers are measurable indicators of biological states or conditions present in biofluids, encompassing proteins, nucleic acids, metabolites, and lipids. [57] Proteins, such as enzymes and antibodies, can serve as indicators of various health conditions. Nucleic acids, including DNA, RNA, and micro RNAs, reveal genetic and epigenetic changes associated with diseases. Metabolites, as small molecules, provide insights into metabolic health and disease states, while lipids changes are often linked to cardiovascular and metabolic disorders. [38], [83], [84]

The intricate makeup of biofluids makes it difficult to identify and quantify biomarkers, so, finding biomarkers that can be evaluated accurately, consistently, and dependably is crucial. [84] Even in patients without symptoms, biomarker screening can provide early identification. [57], [83]

For example, surface-enhanced Raman signals for biomarkers have been obtained from blood and urine for renal function evaluation. These Raman signals were classified according to function using a machine learning algorithm, demonstrating the potential for advanced diagnostic techniques. [82]

1.4.1.1 Blood Plasma

Plasma, the liquid component of blood, is highly valuable in diagnostic applications due to its accessibility and rich array of biomarkers, including proteins, lipids, hormones, electrolytes, and metabolic waste products. These components provide crucial insights into various conditions, such as cardiovascular disease, metabolic disorders, infectious diseases, and cancers. To ensure biomarker integrity, proper collection of plasma is essential, typically achieved through centrifugation, which separates plasma from cellular components. [14], [81], [85]

The minimally invasive nature of blood collection makes plasma a convenient diagnostic medium. Its use in techniques like Surface-Enhanced Raman Spectroscopy (SERS), which enhances signal detection due to the high concentration of target molecules, facilitating rapid, real-time analysis suitable for point-of-care (PoC) applications. [84] For instance, SERS has been successfully utilized for cancer detection by analyzing plasma-derived exosomes, enabling early diagnosis in lung and breast cancers, among others. Additionally, SERS has shown promise in detecting viral infections, such as hepatitis and influenza, through plasma or whole blood samples. [86], [87], [88]

Despite advancements in SERS applications for various diseases, there remains a significant gap in research focused on stroke diagnostics using plasma as a biofluid. This highlights the importance of further investigation in this area. The potential of SERS to identify stroke-related biomarkers, combined with its proven sensitivity, could lead to rapid stroke diagnosis, addressing a critical unmet need in healthcare diagnostics.

Identifying effective diagnostic biomarkers for IS could enhance existing PoC technologies, enabling swift diagnosis that benefits healthcare systems globally. A blood-based biomarker test could complement neuroimaging, improving the early management of IS. Recent technological advancements have produced plasma biomarkers that require minimal expertise for sample collection. These biomarkers are cost-effective and suitable for large-scale clinical applications, making them easier to implement compared to those derived from other biofluids. [84], [85]

Plasma is particularly valuable for studying stroke-related biomarkers due to its direct involvement in vascular complications. Stroke biomarkers can be categorized into three types: diagnostic (to distinguish stroke from mimics), differentiating (to identify stroke types), and predictive (to forecast hemorrhagic transformation of ischemic stroke). Notably, variations in protein levels, such as glial fibrillary acidic protein (GFAP), can indicate hemorrhagic stroke. [38], [83]

Blood-based biomarkers present a potential alternative for early and rapid stroke diagnosis. Accurate differentiation between IS, ICH, and SM could improve pre-hospital pathways and referral systems, allowing for earlier treatment administration. However, no biomarker or biomarker panel with clinically significant predictive accuracy for IS or ICH diagnosis has yet been validated. [83]

1.4.1.1.1 Human Serum Albumin (HSA) as an interferent on biomarker detection in plasma

Human serum albumin (HSA) is the most abundant protein in blood plasma, constituting over 60% of the total plasma protein content. It has typical physiological concentration of approximately 40 mg/mL and a molecular weight of 66,500 Daltons (Da). HSA exhibits a long half-life of 19 days in blood circulation. Moreover, HSA demonstrates remarkable resistance to chemical modifications and stability within a broad pH range (4-9) and temperatures up to 60ºC for 10 hours. [89], [90]

Functionally, albumin plays an important role in maintaining colloid osmotic pressure, serving as carriers of small molecules, including most drugs, and may influence microvascular integrity, as well as various aspects of the inflammatory pathway, including neutrophil adhesion and the activity of cell signaling molecules. [89], [91]

Structurally, albumin molecules in mammals, such as human serum albumin (HSA) in humans and bovine serum albumin (BSA) in cattle, has a heart-shaped configuration composed of three homologous domains (I, II, and III), each containing two subdomains (A and B) with similar structural motifs (Figure 13). The subdomains IIA and IIB contain hydrophobic cavities primarily responsible for ligand binding. Human serum albumins are characterized by a helical tertiary structure and a specific pattern of 17 disulfide bridges formed by 35 cysteine residues. [89], [91]

Colloidally, HSA is a globular protein with a negative charge at neutral pH. Albumin is widely utilized in studies of protein adsorption, protein-protein interactions, and crystallization. [89], [90]

Figure 13. Domain organization of human serum albumin. Domain I (red), domain II (blue), and domain III (green). The 3-D model was generated by PyMOL using 1AO6 PDB file. https://www.rcsb.org/structure/1AO6

When nanoparticles, such as silver nanostars, enter biological environments, they encounter a complex mixture of biomolecules, leading to the formation of a protein corona at the surfaces (Figure 14). This process is driven by the high surface free energy of nanoparticles, which attracts and adsorbs biomolecules from the surrounding biological fluids, such as blood, thereby reducing the overall surface energy and promoting nanoparticle dispersion. The protein corona is not merely a random

accumulation of proteins but consists of distinct layers with unique properties: the hard corona and the soft corona. [92]

The hard corona is a near-monolayer of biomolecules that bind tightly to the nanoparticle surface, with slow exchange rates that render it relatively stable over extended periods, ranging from hours to days. This layer is typically composed of only a small fraction of the biomolecules available in the biological milieu, and its composition is determined by factors such as nanoparticle surface properties, including size, shape, charge, and surface chemistry. Notably, the proteins found in the hard corona are not necessarily the most abundant proteins in the environment, nor are they always those with the highest affinity for the nanoparticle surface; rather, they are those that achieve a stable interaction through a combination of binding strength and kinetic stability. An exception to this is observed in plasma, where albumin, the most abundant protein, is commonly found in the hard corona. Once formed, the hard corona can exhibit a sort of "memory" of the nanoparticle's previous environment, as subsequent exposure to different biological conditions may only partially displace the existing corona components (Figure 14). [92], [93], [94]

Overlying the hard corona is the soft corona, a more loosely associated layer of biomolecules characterized by rapid exchange dynamics with the surrounding medium. The soft corona forms and dissipates on timescales of seconds to minutes, reflecting the immediate composition of the surrounding environment. The boundary between the hard and soft coronas is critical, as it often dictates the initial biological interactions of the nanoparticle, including its recognition and processing by cells and tissues (Figure 14). [92], [93], [94]

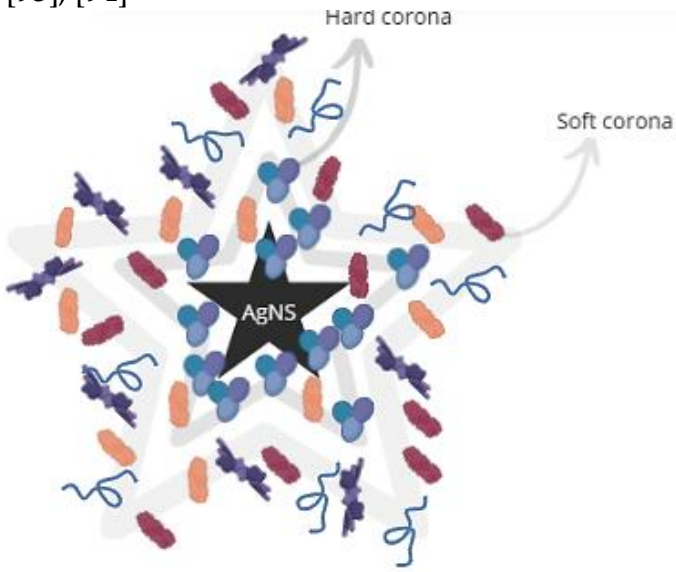

Figure 14. Schematic distribution of hard and soft protein coronas on a AgNS. The different shapes represent different proteins adsorbed to the AgNS. Created in Canvas.com and Biorender.com.

The interactions leading to protein corona formation involve various weak, non-covalent forces such as van der Waals forces, electrostatic interactions, hydrogen

bonds, and hydrophobic effects. These interactions are sufficient to cause conformational changes in both the proteins and at the nanoparticle-protein interface. In cases of strong interactions, such as with proteins containing sulphur groups, which can form robust bonds with silver surfaces, these conformational changes can be significant and may alter the protein's secondary and tertiary structures. For example, human serum albumin (HSA), a major component of the protein corona on silver nanostars, has been shown to undergo structural rearrangements, including reductions in α-helices and increases in β-sheets upon adsorption to citrate-coated silver nanoparticles. [95], [96] These modifications not only impact the stability and biological function of the nanoparticles but are also particularly relevant for our study, as the binding of biomarkers to albumin can hinder their detection at the surface of the AgNS. Therefore, it is crucial to address this issue to ensure that our biomarkers remain accessible for accurate detection.

The specific composition and stability of the protein corona on silver nanostars are influenced by various factors, including the nanoparticle's size, shape, and surface characteristics, as well as the concentration and type of proteins in the surrounding fluid. Analytical techniques such as SERS have been utilized to study these interactions, with findings indicating that the protein corona can significantly stabilize silver nanoparticles against aggregation and influence their dissolution rates. Moreover, the phenomenon known as the Vroman effect plays a role in corona dynamics; initially adsorbed proteins with lower affinities are often replaced by others with higher affinities over time, reflecting a dynamic and competitive binding environment. [97] In this context, it is essential to recognize that albumin is the primary constituent of the protein corona, particularly during the initial stages. This predominance can obstruct access to biomarkers at the surface of the AgNS, thereby hindering their detection and necessitating strategies to mitigate this effect for accurate diagnostic outcomes.

Given the potential challenges posed by albumin's presence in the protein corona, we are committed to investigating its impact on our assays by comparing conditions with and without albumin. This approach will allow us to assess how the presence of albumin affects biomarker accessibility and detection.

1.4.1.2 GFAP as a Biomarker of Hemorrhagic Stroke

Glial Fibrillary Acidic Protein (GFAP) is a proteolytic enzyme (Figure 15) predominantly expressed in astrocytes, where it plays a crucial role in cell-cell communication, astrocyte-neuron interactions, and the maintenance of the blood-brain barrier (BBB). The rupture of the BBB leads to astrocyte apoptosis and the subsequent release of GFAP into the bloodstream. GFAP is also involved in reparative processes within the central nervous system following injury. During ICH, the rupture of astrocytic cells leads to a rapid release of GFAP into the bloodstream. This contrasts with the slower increase in GFAP blood levels observed in AIS, making GFAP a potential biomarker for differentiating between ischemic and hemorrhagic strokes. [98] The concentration

of GFAP in the blood has been shown to correlate with hematoma size, demonstrating good sensitivity and specificity in distinguishing between stroke types, particularly in cases involving large hematomas. [38]

Figure 15. Crystal structure of the human glial fibrillary acidic protein 1B domain. The 3-D model was generated by PyMOL using 6A9P PDB file. https://doi.org/10.2210/pdb6A9P/pdb

Among the biomarkers studied for distinguishing these stroke types, GFAP is one of the most extensively researched. In IS, BBB rupture typically occurs due to ATP depletion and dysfunction of the Na/K pump, resulting in endothelial and astrocyte apoptosis. In contrast, ICH causes a more rapid and mechanical breakdown of the BBB, leading to a quicker and higher concentration of GFAP in the blood. This characteristic makes GFAP a more reliable marker for ICH compared to IS. [38] HS patients exhibit significantly higher levels of GFAP than those with IS during the first 24 hours, which may be attributed to the earlier disruption of the BBB in HS patients compared to IS patients (Table 1). Moreover, the diagnostic performance of GFAP varies depending on the timing of measurement, highlighting the importance of considering timing when evaluating the diagnostic potential of biomarkers. [84]

Given the complexity of stroke pathology, relying on a single biomarker like GFAP may not be sufficient for accurate diagnosis. A panel of biomarkers with complementary characteristics is likely necessary for the differentiation and prediction of stroke outcomes. However, our study will focus exclusively on GFAP as a single biomarker to model the plasma profiles of IS and HS. SERS could prove valuable in identifying distinct spectral profiles based on stroke type, further enhancing diagnostic accuracy.

Table 1. GFAP levels in the plasma when a ACI and HS has occurred. Adapted from [99].

				Diagnosis group						
				Acute cerebral ischemia (ACI)			Hemorrhagic stroke (HS)			
Biomarker	Sampling timepoint	*n* (ACI)	*n* (HS)	Median concentration (pg/mL)	IQR		Median concentration (pg/mL)	IQR		*P* value
GFAP	Initial prehospital sample, <1 hour	111	37	156.4	97.3 -	294.7	361.7	189.4 -	604.1	<0.001
	Initial prehospital sample, <3 hour	178	59	178.2	99.7 -	295.1	468.9	197.7 -	1188.2	<0.001
	Secondary sample, <3 hour	166	57	189.6	110.1 -	310.2	563.1	301.3 -	1625.3	<0.001
	Next morning	203	60	622.7	241.3 -	2297.4	19 300.7	3055.0 -	57 593.7	<0.001

1.5. Machine Learning and Data Analysis

The integration of machine learning (ML) with Surface-Enhanced Raman Spectroscopy (SERS) enhances the analytical power of this technique. By employing ML algorithms, researchers can efficiently manage and interpret complex datasets, uncovering patterns and relationships within Raman Spectra that may not be apparent to human analysis. This capability improves both the sensitivity and specificity of diagnostic applications.

1.5.1 Overview of Machine Learning in Spectroscopy

Machine Learning (ML) has become increasingly vital in spectroscopy due to its ability to handle high-dimensional data and identify subtle patterns that traditional methods might miss. In the context of SERS, ML algorithms such as Support Vector Machines (SVM), Random Forests, and Neural Networks are commonly used to classify spectral data, predict outcomes, and perform unsupervised clustering for exploratory analysis. Classical statistical methods, including Principal Component Analysis (PCA) and multivariate analysis, are also employed to differentiate information from target analytes by considering the full spectral fingerprint. For example, SERS fingerprinting followed by PCA analysis has been successfully applied to discriminate tea varieties, [100] although it has yet to be widely explored for distinguishing wines from different regions. [68]

The application of ML in spectroscopy allows for automated data processing, feature extraction, and predictive modelling, significantly speeding up the analytical workflow. Automated data analysis through artificial intelligence (AI) has garnered attention for Raman signal analysis, especially with advancements in high-sensitivity signal acquisition technologies. AI methods such as deep neural networks can support classification based on complex patterns in SERS data, including the detection of metabolites, though these classifiers are often considered "black boxes." Careful curation

of training data is crucial to avoid bias and ensure clinical relevance. On the other hand, deterministic classifiers like SVMs, known for their robustness against overfitting, are useful for their precise decision boundaries, though they require careful kernel selection to optimize performance. [59], [101]

1.5.2 Principal Component Analysis (PCA) in SERS

Principal Component Analysis (PCA) is a widely used statistical technique in SERS for dimensionality reduction and noise reduction, making complex spectral datasets more manageable and interpretable. PCA transforms the original spectral data into a set of orthogonal components, known as principal components (PCs), that capture the most significant variance in the data. This technique helps in highlighting the most relevant features of the spectra, allowing for easier visualization and identification of patterns, clusters, or outliers. For example, in cancer detection, PCA has been used as an initial step to identify orthogonal principal components that capture the correlated spectral variance between measurements, facilitating clustering and categorization by diagnosis. [59], [102]

PCA is often combined with other methods to enhance classification accuracy. For example, when paired with discriminant analysis (DA), PCA serves to reduce data dimensionality along axes that maximize correlated variance, improving the differentiation of cancer spectra. Moreover, PCA followed by DA has proven effective in minimizing class variance while maximizing between-class differences, a crucial factor in diagnostic applications. Despite PCA's utility, it does not always fully separate datasets when used alone, necessitating the combination with other techniques like DA or partial least squares discriminant analysis (PLS-DA), which can outperform PCA in certain discrimination tasks. [59], [102]

1.5.3 Stroke Diagnosis Using SERS and Machine Learning

The combination of SERS and ML has shown promise in the diagnosis of stroke by enabling the rapid and accurate analysis of patterns of biomarkers present in bodily fluids. For instance, SERS can detect subtle changes in the biochemical composition of blood, which are indicative of stroke. ML algorithms, such as Convolutional Neural Networks (CNNs) and SVMs, can then analyze the spectral data to classify the stroke subtype or predict the onset and severity of the stroke. This approach offers a non-invasive, quick, and reliable diagnostic tool that could significantly improve patient outcomes by enabling timely interventions.[103], [104]

1.6. Objectives

The final and future aim is to develop a pre-hospital point-of-care test (PoCT) for rapid and accurate stroke diagnosis by leveraging bioconjugates of patient plasma

and silver nanostars (AgNS), combined with Surface-Enhanced Raman Spectroscopy (SERS), to effectively differentiate between ischemic and hemorrhagic strokes. The research is structured on several specific objectives.

The first goal is to optimize the bioconjugation of AgNS with human serum albumin (HSA), with commercial human plasma or with plasma depleted from HSA, in order to identify distinct spectral fingerprints using SERS. This technique is only sensitive to proteins which are directly in contact with the surface of AgNS, and so, a significant part of this objective is to determine whether the bioconjugation process favours relevant plasma proteins. Moreover, bioconjugates of plasma spiked with different Glial Fibrillary Acidic Protein (GFAP) levels were also analysed by SERS. GFAP is a glial protein released to blood following brain lesion. Early after stroke onset, high concentrations of circulating GFAP indicate haemorrhagic stroke, while low levels in the blood are associated with ischemic stroke.

Another critical objective is to evaluate the potential interference of HSA, the most abundant protein in plasma, which could mask SERS signals from other important plasma proteins. This involves a thorough analysis of the SERS spectra to determine whether albumin interferes with the detection of other important stroke biomarkers. Spin columns were used to deplete albumin from plasma samples, followed by a comparative analysis of the SERS signals from both albumin-depleted and non-depleted samples.

In addition to bioconjugation and protein detection, this research also focuses on the optimization of experimental conditions to maximize SERS signal quality. This includes the evaluation of various substrates for sample placement, namely aluminium and photocopy paper. Photocopy paper have proven in previous studies to be a practical substrate for sample placement for SERS analysis, namely due to its fluorescence-quenching properties. Another aspect of optimization involves testing different incubation times to ensure that the protein corona forms around the AgNS as quickly as possible, allowing for an almost immediate SERS reading. Rapid diagnostic capability is essential for stroke management, making the speed of the diagnostic tool a critical factor.

Human plasma spiked with different concentrations of GFAP will be tested under varying incubation times to determine whether GFAP can be reliably detected using SERS.

Finally, advanced data analysis techniques, including Principal Component Analysis (PCA), will be employed to identify relevant spectral differences or patterns between samples. This statistical approach will also serve as a foundation for the future integration of machine learning algorithms, which could enhance diagnostic precision and enable the automation of stroke classification.

The workflow of this project is represented in Figure 16.

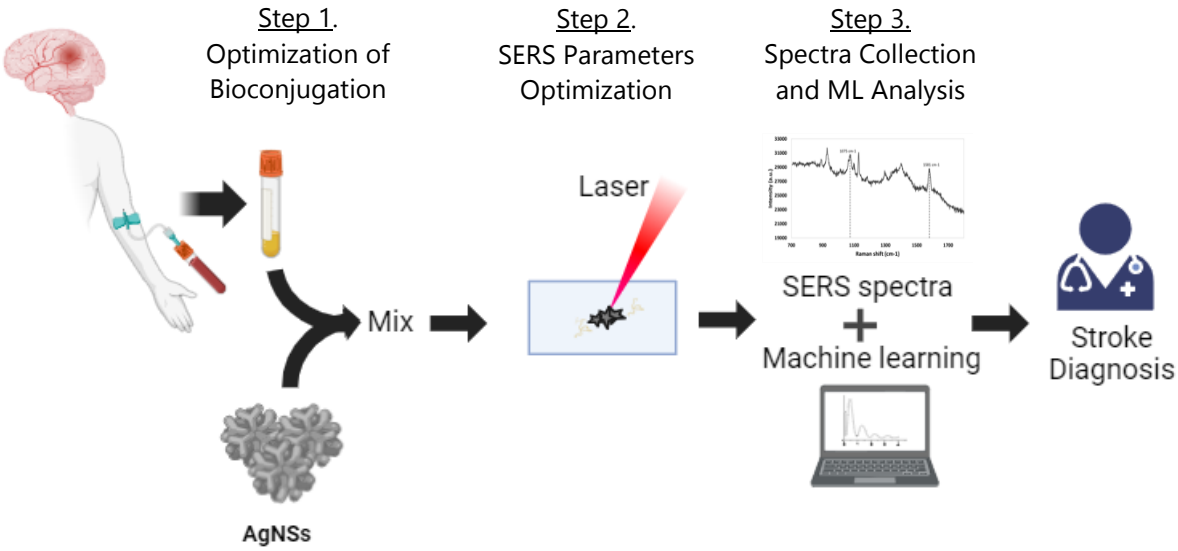

Figure 16. Stroke diagnosis using SERS detection of biomarkers patterns using AgNS-plasma bioconjugates and machine learning for data analysis.

2. MATERIALS AND METHODS

2.1 Materials

The following reagents and materials were used throughout the experiments: potassium phosphate buffer (KPB), human serum albumin (HSA), and human plasma (referred to as "plasma" throughout this dissertation), all purchased from Sigma-Aldrich (St. Louis, MO, USA). Human plasma was resuspended in 1 mL of ultrapure water (H_2O, 18.2 MΩ·cm at 25ºC, MilliQ®) and stored in aliquots in liquid nitrogen. For later use, aliquots were diluted 1:1 with ultrapure water. Glial Fibrillary Acidic Protein (GFAP), obtained from HyTest, Finland, was diluted to a concentration of 0.1 mg/mL in phosphate-buffered saline (PBS, 1x, pH 7.4, Sigma-Aldrich, St. Louis, MO, USA), prepared with distilled water. The general equipment utilized included stirring rods, syringes, flasks, tips, thermometers, Falcon tubes and Eppendorf tubes.

For protein determination using the bicinchoninic acid (BCA) method, a kit from Sigma-Aldrich, (St. Louis, MO, USA) was employed. This kit included a 4% (w/w) cooper (II) sulfate solution and BCA solution. The standard used for this assay was 2.0mg/mL of bovine serum albumin (BSA) from Thermo Fisher Scientific (Waltham, USA).

Agarose gel electrophoresis involved the use of Ultrapure™ Agarose from Bio-Rad, along with Tris-acetate EDTA (TAE) buffer from Sigma Aldrich (St. Louis, MO, USA). For SDS-PAGE, the following reagents were used: N,N,N′,N′-Tetramethyl ethylenediamine (TEMED, >98%) from Tokyo Chemical Industry (TCI, Japan), glycine (> 98.5 %) from Carlo Erba, ammonium persulphate (APS, 10% w/v), β-mercaptoethanol (>99.0%), sodium dodecyl sulphate (SDS, >98.5%), and Brilliant Blue R-250, all from Sigma-Aldrich (St. Louis, MO, USA). Additionally, glycerol (99.5%) and bromophenol blue were sourced from Panreac AppliChem (Gatersleben, Germany). The preparation of SDS-PAGE was using a 30% (w/v) acrylamide/bisacrylamide solution and the SDS-PAGE Mini-PROTEAN system kit from Bio-Rad. A low molecular weight (LMW) protein marker from NZYtech, Portugal was also used.

Colloids of silver nanostars (AgNSs) were obtained through a collaboration with Dr. Maria Enea at LAQV/REQUIMTE at the laboratory of Prof. Eulália Pereira, from LAQV/REQUIMTE and the Department of Chemistry and Biochemistry of the Faculty of Sciences, University of Porto.

2.2 Equipment

Cold storage of 4°C was necessary for several reagents as well as the biological samples, such as BSA and HSA, using a SANYO Medicool refrigerator.

For general laboratory procedures, an analytical balance from RADWAG, a circulator heated water bath from Bioblock scientific, a vortex mixer from VELP Scientifica and a Centurion Scientific K3 Series centrifuge were employed. Additionally, a stirring and heating plate from P Selecta, as well as Bio-Rad's agarose gel electrophoresis mold and electrode kit were utilized to create an agarose gel electrophoresis (AGE). Uv-Vis Spectra of AgNSs were acquired using a Varian Cary 50 Bio.

Dynamic light scattering (DLS), and zeta potential measurements were performed using a 10 mW Horiba nanopartica SZ-100V2 Series. This device uses classical single scattering to measure particle sizes (0.3 nm to 10 μm). A diode-pumped frequency-doubled laser with a 532 nm wavelength and 173º scattering angle was used. Samples were prepared in a temperature-controlled cuvette holder and diluted to prevent multiple scattering effects. DLS was conducted using equipment provided by Professor César Laia and Nuno Basílio, from the Chemical Department of NOVA School of Science and Technology and LAQV/REQUIMTE. [105]

Spectral acquisition for Surface-Enhanced Raman Spectroscopy (SERS) was performed using a Renishaw inVia™ confocal Raman microscope with air-cooled device (CCD). Samples were placed on substrates such as glass plates, aluminium foil (Aluminium 20x0.29 m, thickness 12 μm, Continente), Whatman No. 1 paper (WT; Whatman Internacional Ltd., Florham Park, NJ), photocopy paper (FC, 300%, Portucel Soporcel, Setúbal, Portugal), WT with AgNP deposition and FC with deposition of 100 nm of molybdenum (Mo). The SERS equipment and paper substrates for sample placement result from a partnership with CENIMAT|i3N and the Material Sciences Department of NOVA School of Science and Technology, respectively, with Professor Hugo Águas and Dra. Maíza Ozório.

2.3 Methods

2.3.1 Total protein quantification of HSA and commercial plasma

The bicinchoninic acid (BCA) assay was used to quantify total proteins in HSA and human plasma, modified from Sigma Aldrich [106] and Pierce [107] protocols. This colorimetric technique utilizes peptide bonds reacting with cooper ions, reducing Cu^{2+} to Cu^{+}, facilitating protein quantification. The reaction, known as the biuret reaction, induces a color change when bicinchoninic acid interacts with the cuprous ion complex. The vivid blue color formed is detected at 562 nm, and the intensity of the color change correlates directly with the amount of protein in the sample. [108]

A developing reagent was prepared by mixing BCA and cooper sulfate in 5:1 ratio (Figure 17). Following, 10μL or 20μL samples were mixed with 1mL of the determination reagent in Eppendorf tubes. After adding either the BSA standard or the sample, each tube was briefly vortexed. The tubes were then incubated in a water bath at 37ºC for 30 min. After cooling, the absorbance of each sample at 562 nm was measured using a UV-Vis spectrophotometer. A calibration curve was created using the absorbance values of standards (ranging from 0

to 50 μg of BSA standard (Sigma Aldrich, St. Louis, MO, USA) on the y-axis versus their known concentration on the x-axis. Sample concentrations were determined by comparing their absorbance readings to this calibration curve.

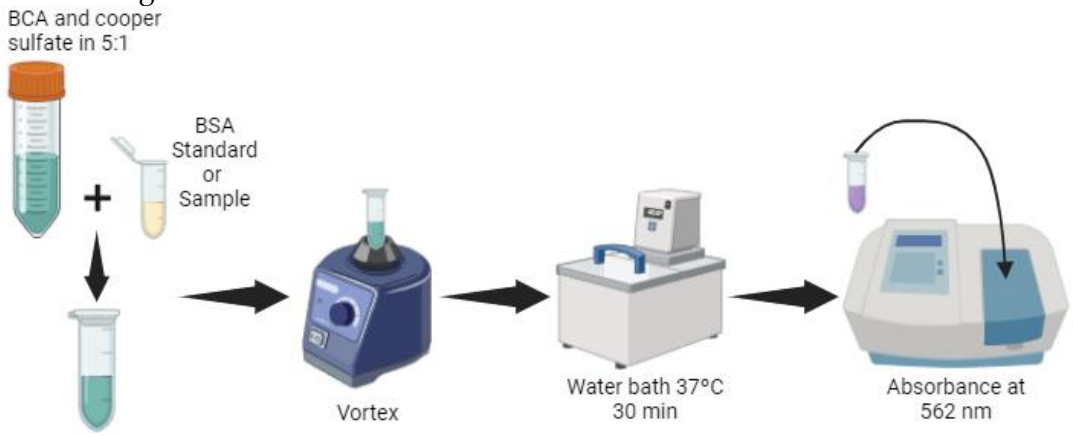

Figure 17. Process of the Bicinchoninic Acid (BCA) Protein Assay. Created in Biorender.com.

2.3.2 Bioconjugation of silver nanostars with HSA or commercial plasma

Silver nanostars (0.05 nM – 0.07 nM) were bioconjugated with HSA (35-45 mg/mL) or human plasma (35-40 mg/mL) by incubating aliquots overnight at 4°C. Bioconjugates were prepared by diluting HSA in 20 mM KPB and human plasma in ultrapure water to various concentrations, so that different concentrations could be studied. Depending on the intended measurements, samples were centrifuged at 2500 g for 10 min, the supernatant was removed, and the pellets were resuspended in 20 mM KPB for HSA and ultrapure water for human plasma. Following this preparation, samples underwent characterization, including electrophoretic mobility and Surface-Enhanced Raman Spectroscopy (SERS) (Figure 18).

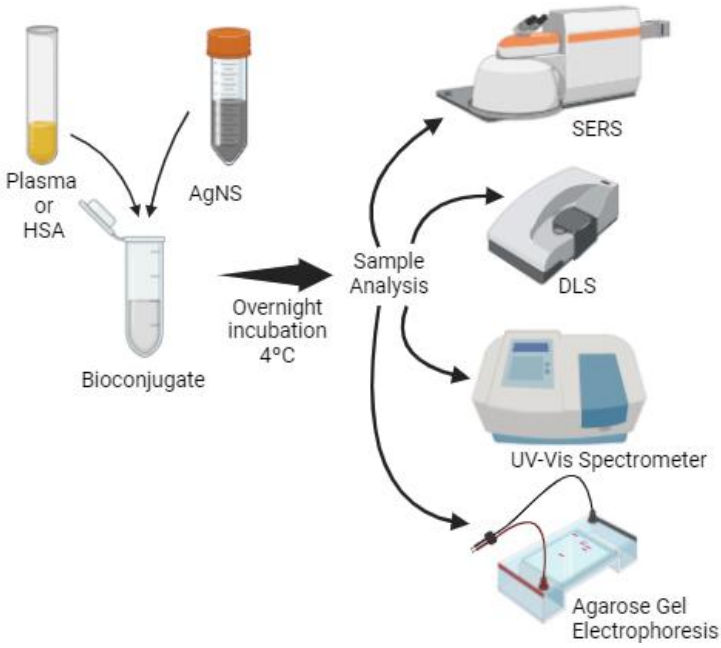

Figure 18. Workflow of characterization measurements after bioconjugate preparation. Created in Biorender.com.

For the bioconjugation of spiked plasma with GFAP, a preliminary step was also necessary before adding the AgNSs (Figure 19). GFAP was diluted with PBS 1x to achieve concentrations relevant to hemorrhagic stroke scenarios: 0.1 ng/mL (initial hours of HS), 0.5 ng/mL and 1 ng/mL (after 3 hours of HS) [109]. The diluted GFAP was then added to plasma and allowed to interact for 15-20 min. After this incubation period, AgNSs were added to the mixture.

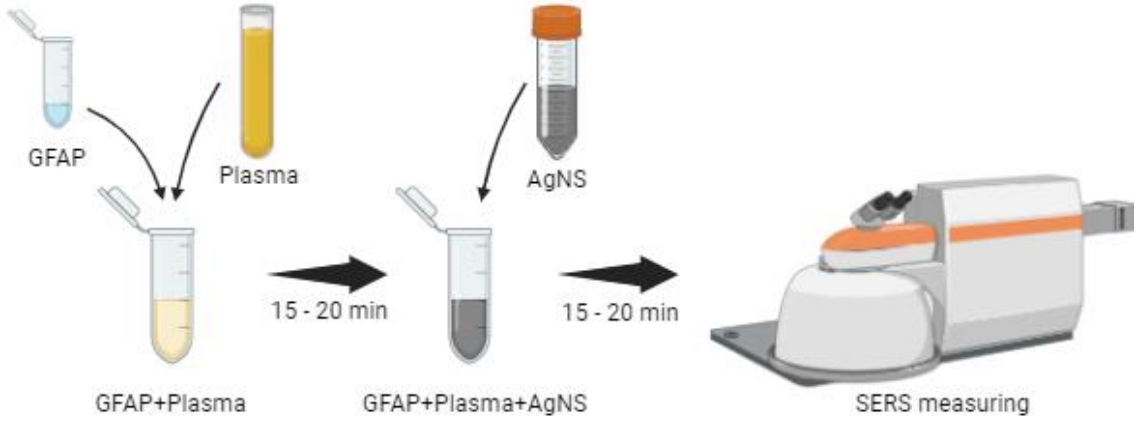

Figure 19. Schematic preparation of plasma samples spiked with GFAP and preparation of bioconjugates with AgNS. Created in Biorender.com.

2.3.2.1 Production of albumin-free human plasma

For the bioconjugation of AgNSs with plasma without albumin, an initial step was undertaken to eliminate albumin prior to the mixing process with AgNSs. This

was accomplished using an AlbuminOUT column kit (G-Biosciences), adhering to the protocol outlined in reference [110] (Figure 20). This kit is particularly effective, capable of removing over 98% of albumin from plasma samples, thereby ensuring that the resulting plasma solution is predominantly free of this protein.

After albumin removal, the processed plasma underwent a subsequent step involving concentration using a concentration column (Amicon® Ultra Centrifugal Filter, 30kDa MWCO). This step is necessary because the use of different reagents for albumin depletion can dilute the sample. Following concentration, the plasma without albumin was mixed with the AgNSs to create bioconjugates.

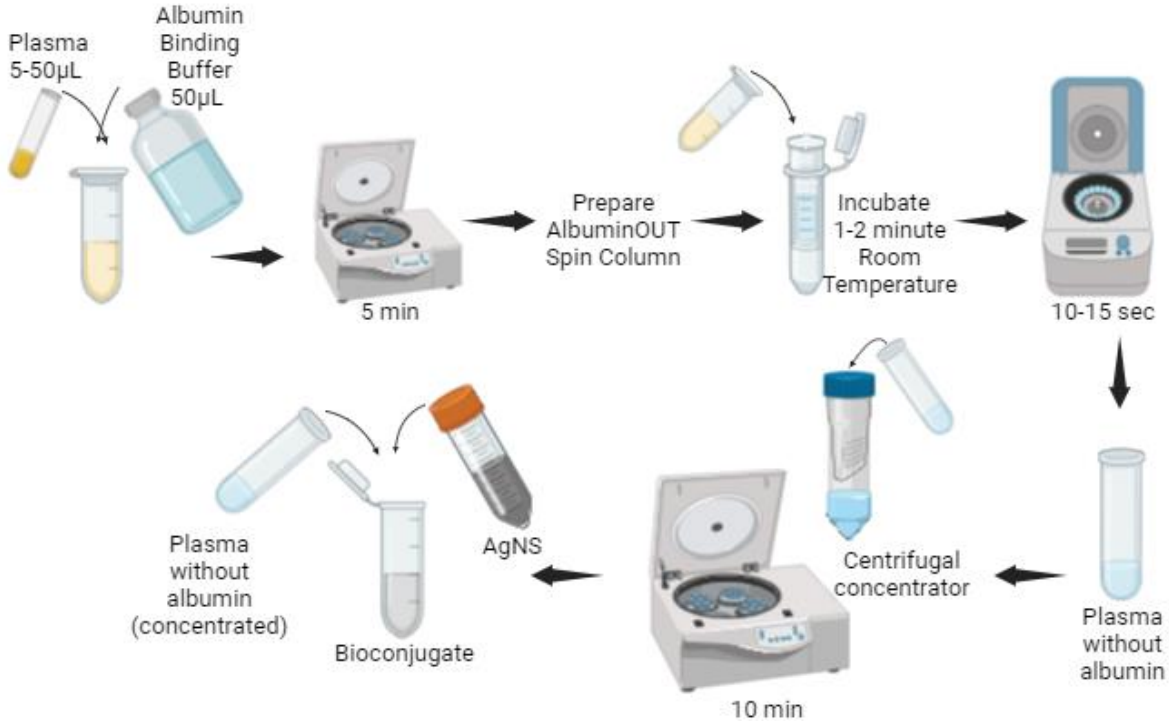

Figure 20. Schematic process of plasma without albumin bioconjugates preparation. Created In Biorender.com

2.2.3 UV-Visible Spectroscopy

UV-Vis was initially employed to check stability of AgNSs from their synthesis at the University of Porto until their arrival at University of NOVA, monitoring any change in the optical properties of the AgNSs. Additionally, UV-Vis spectra were collected over a 40-day period to monitor the stability of AgNSs in solution, stored in both a glass bottle and plastic Falcon tube.

For these stability experiences, the AgNSs were diluted 1:10 for UV-vis measurements, compared against ultrapure water with a baseline correction. The spectral range was from 300 nm to 800 nm, featuring a localize surface plasmon resonance (LSPR) peak for silver nanoparticles (AgNPs) at approximately 380-385 nm, depending on the AgNSs batches [66]. One spectrum corresponds to the day the AgNSs arrived (day 1), and there are five UV-Vis spectra from the AgNSs stored in plastic and

five for those in glass (days 7, 14, 21, 28, and 40), in duplicates. Spectra were obtained using quartz cuvette.

For control measurements, the UV-Vis spectrum of HSA was obtained in a spectral range from 200 nm to 900 nm with a 1:10 dilution, using KPB 20 mM pH 7.4 as the baseline correction. Similarly, the human plasma control was measured using the same spectral range and a 1:10 dilution, with ultrapure water for baseline correction. Both spectra were acquired using a quartz cuvette.

2.2.4 Surface-Enhanced Raman Spectroscopy

The preparation of bioconjugate samples for SERS begins with centrifugation at 2500 g for 10 minutes at 4°C. The resulting pellet is then resuspended in 15μL of KPB 20 mM pH 7.4 and 15 μL of ultrapure water for plasma:AgNSs bioconjugates. Controls for HSA, plasma or AgNSs (0.07 nM) required no additional preparation (Figure 21).

SERS spectra were acquired using a He-Ne laser at 633 nm, with a power of 32 mW, 1800 nm/l gratings, and a 20x objective lens. Spectra were collected from 700 cm^{-1} to 1800 cm^{-1}, with three spectral accumulations of 10 seconds each. This SERS system has a spectral resolution of 0.3 cm^{-1}. Raw data were collected using WiRE 5.6 software.

For analysis, at least five spectra were obtained. Different substrates were tested for sample placement to improve SERS signal: aluminium foil, Whatman No.1 paper, photocopy paper, Whatman No. 1 with AgNP wells and photocopy with deposition of 100 nm of molybdenum (Mo). During different Raman sessions, the spectrograph was calibrated using the Raman peak of an internal silicon wafer at 520.7 cm^{-1} to minimize any potential variations in the Raman system.

PeakFit software was used for spectral analysis, employing baseline correction and Gaussian deconvolution to identify vibrational levels via the Lorentzian area. This provided details on SERS lines and their corresponding areas, used for the PCA evaluation.

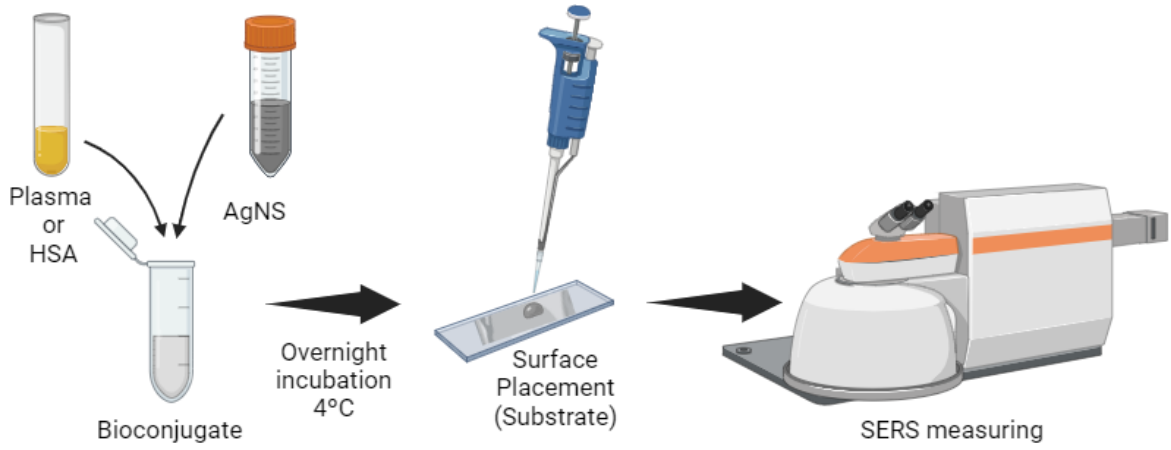

Figure 21. Schematic illustration of a general procedure for SERS measurement. Created in Biorender.com.

2.2.4.1 Substrates for Surface Sample's Placement

The substrate fabrication process involved: (1) formation of wells with hydrophobic barriers (wax) for the Whatman No. 1 paper and photocopy paper (Figure 22A and 22B) and (2) deposition of AgNPs for the wells on Whatman No. 1 paper.

For well formation, the layout was designed using Adobe Illustrator and printed with a wax printer (Xerox Corporation, Norwalk, CT, USA). This printer uses solid wax ink to create hydrophobic regions according to the layout. The wells had a diameter of 3 mm. After printing, the papers were placed on a heating plate at 140 °C for 2 minutes, allowing the wax to melt and diffuse vertically throughout the paper, creating a hydrophobic barrier. These substrates were used for SERS detection.

For Whatman No. 1 paper substrate with AgNP wells (Figure 22C), AgNPs were deposited into the unwaxed regions using electron beam evaporation (e-beam). This method involves materials under vacuum to create thin films. An electron beam targets the material, evaporating it onto the substrate to form a uniform thin film. This approach improves film uniformity and allows precise control over the thickness, size, and shape of the nanoparticles. The Whatman paper substrate was placed on a glass plate and covered with a Kapton® mask with 3 mm diameter circles. The substrate was maintained at 150 °C during evaporation at a pressure of 10^{-5} mbar and a deposition rate of 0.07 nm/s. Deposition stopped when a thickness of 6 nm was reached. After deposition, the e-beam evaporated AgNP substrates were used for SERS detection.

Other substrates were use for this project, such as photocopy paper with molybdenum deposition (Figure 22D) and aluminium foil (Figure 22E).

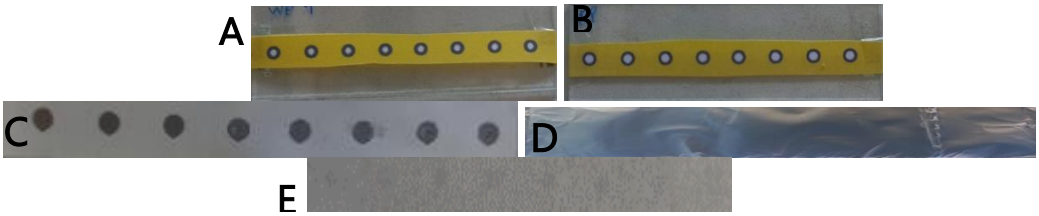

Figure 22. Front view of the different substrates: **A**. Whatman No. 1 paper **B**. Photocopy paper **C**. Whatman No. 1 paper with AgNP wells deposition **D**. Photocopy paper with Mo deposition **E**. Aluminium foil.

2.2.5 Dynamic light scattering (DLS)

Dynamic light scattering (DLS) is a technique for measuring the size of nanoparticles by analyzing their hydrodynamic diameter. It examines the velocity of Brownian motion, random particle movement caused by thermal agitation. Larger particles move more slowly and cause slower fluctuations in light intensity (Figure 23). In DLS, a laser beam shines on the sample, and scattered light is detected at a specific angle. The resulting intensity fluctuations are used to calculate the autocorrelation function, which is related to the translational diffusion coefficient. This coefficient, through the Stokes-Einstein equation (Equation 1), allows the determination of the particles' hydrodynamic radius. [111], [112] In addition to measuring particle size, DLS provides the polydispersity index (PDI), which indicates the degree of size distribution within the nanoparticle sample. A lower PDI value signifies a more uniform size distribution, while higher values indicate greater variability in particle size. The PDI is crucial for assessing the homogeneity of nanoparticles, as a narrow size distribution is often desirable for reproducible results and reliable nanoparticle performance in applications.

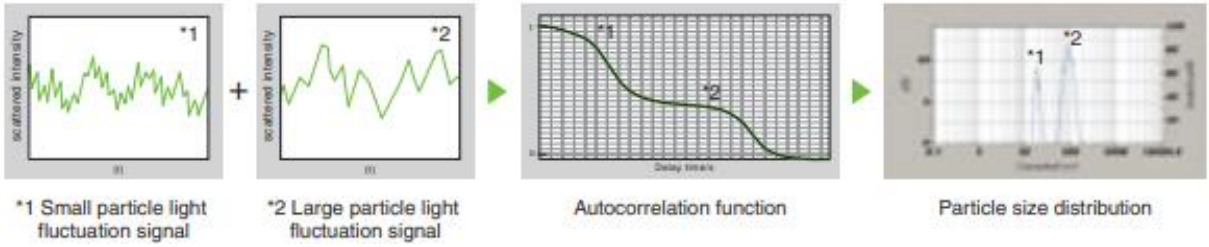

Figure 23. Particle size calculated from the diffusion coefficient using the Stokes-Einstein equation. Adapted from [112].

$$D(h) = \frac{kT}{3\pi\eta Dt} \qquad \text{Equation 2}$$

Where *D(h)* is the hydrodynamic diameter, *k* is the Boltzmann constant, *T* is the absolute temperature, η is the viscosity of the medium, and *Dt* is the translational diffusion coefficient.

Zeta potential, a key parameter in nanoparticle stability, refers to the electrical potential at the shear plane of a nanoparticle, which is the boundary where the surrounding fluid begins to move with the particle. It is a measure of the surface charge

of the nanoparticles and can be determined by observing particle movement in response to an applied electric field. The velocity of this movement, calculated using the Doppler shift in scattered light, is then used to determine the zeta potential (Figure 24). For the silver nanostars (AgNSs) in this study, the charge is typically negative, which plays a critical role in attracting biomolecules and forming a protein corona around the nanostars. [111], [112], [113]

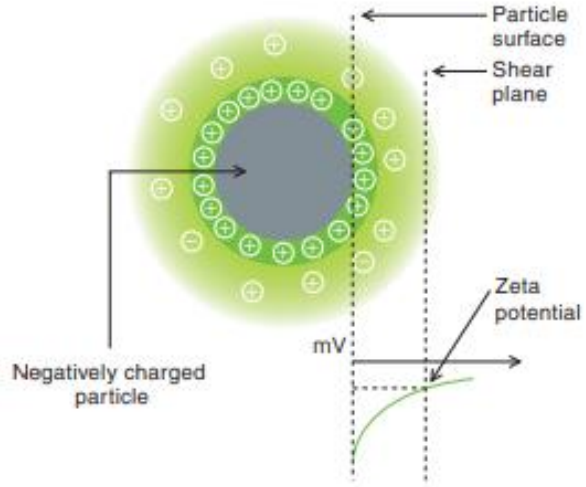

Figure 24. Zeta potential measurement principle (Laser Dopler Electrophoresis). Adapted from [112].

In the experimental setup, bioconjugate samples were diluted 1:2 with distilled water filtered through an inorganic membrane (diameter 13 mm, pore size 0.2 μm, Cat. FFL/MLL Acrylic Blue Membrane from GVS Dist. Sterile). DLS measurements for hydrodynamic size (nm) and PDI were conducted at an angle of 173º, with 30-second noise cut to remove background noise. Zeta potential measurements used a monodisperse calculation calibrated with the refractive index of silver nanoparticles (AgNPs) and a water dispersion medium, applying the Smoluchowski coefficient. Each sample underwent five measurements of each data type, and the average values were used for analysis.

2.2.7 Agarose gel electrophoresis

To prepare the 0.3% (w/v) agarose gel, we used 0.5x Tris-acetate-EDTA (TAE) buffer (pH 8) to dissolve powered agarose (Ultrapure™ Agarose from Bio-Rad Bio-Rad). The agarose mixture was heated to 75°C and stirred at 600 rpm until it became transparent. The hot agarose solution was poured into a gel tray with a comb to create the wells for sample loading. Before loading the samples into the wells of the agarose gel, centrifugation at 9500 g for 10 minutes at 4°C was performed to pellet the denser AuNP-containing bioconjugates. The pellets were then resuspended in 13.5 μL KPB 5 mM and 1.5 μL glycerol. Each well was loaded with 15 μL of sample.

The agarose gel was run in 0.5x TAE Buffer chamber at 80 V for two hours. After this period, the distance migrated by the samples from the well to the end of the

gel was measured using ImageJ software (National Institutes of Health, https://imagej.nih.gov/ij/). AGE was used to measure the electrophoretic mobility of samples and assess the binding of proteins to AgNSs, which can increase their size and reduce their movement through the gel. Additionally, as AgNSs become covered with proteins, their charge decreases, resulting in reduced migration towards the positive pole. These two phenomena, size and charge, result in the bioconjugate bands appearing closer to the wells, or starting point, on the gel.

2.2.8 SDS-PAGE

SDS-PAGE gels were prepared with 12.5% (v/v) acrylamide for the separation gel and 5% (w/v) for the stacking gel, enabling separation of approximately 12 to 60 kDa. [114] SDS-PAGE gels were run for 1.5 hours at 150 V with 15 μL of the prepared samples and the LMW protein marker, coated in 1:10 running buffer. The gels were stained with 2% (w/v) Coomassie Blue R-250 for two hours, and then the staining was removed until the protein bands were visible.

A 1:100 dilution of the HSA and human plasma was used as control. Plasma:AgNSs bioconjugates were prepared by allowing the bioconjugates to incubate for three hours, with some left overnight for comparison. Equal volumes of sample and sample buffer were mixed and heated to 100°C for two minutes, followed by a rapid centrifugation for fifteen seconds. The distance from the wells to the samples that ended in the center of the strongest band, was measured using ImageJ (National Institutes of Health, https://imagej.nih.gov/ij/).

2.2.8.1 Plasma concentration determination

Through the SDS-PAGE experiment (section 3.5.3) , we assessed the concentration of plasma proteins. The BCA assay provided the total protein concentration in mg/mL. Using SDS-PAGE, we determined the molecular weight (MW) of individual plasma proteins. By identifying the concentration of each specific protein and their percentage contributions to the total plasma composition, albumin (60%), globulins (35%), and fibrinogen (4%), we could estimate their respective nanomolar (nM) values.

Summing these individual protein concentrations allowed us to calculate the overall molarity concentration for the entire plasma sample, facilitating a direct comparison with the concentration of AgNSs in molarity too. This comparison enhances our understanding of the relative interactions and potential binding dynamics between these components.

However, it is important to note that this estimation process may be subject to biases and errors due to the complex and heterogeneous nature of the plasma proteome, particularly in cases of health disorders.

2.2.9 PCA Analysis

Spectra for PCA were obtained using SERS on aluminium foil for sample placement, with a 20x objective, a laser power of 50 mV, and an exposure time of 5 seconds. The concentrations used for each sample correspond to the ten ratios discussed in sections 3.4, 3.5, and 3.5.4 for albumin, plasma, and plasma without albumin, respectively. Peak fit software was employed to obtain the area corresponding to the SERS lines, and these values were used for the PCA analysis (section 3.6).

3. Results and discussion

3.1 Colloidal stability of silver nanostars over time

Understanding the long-term stability of silver nanostars (AgNS) is important, particularly in the context of extended storage for future point-of-care testing (PoCT) applications. AgNS are distinguished by their star-like morphology with sharp edges and points, unlike the more commonly studied spherical nanoparticles. [63], [115], [116] These sharp features give AgNS distinctive optical properties, namely providing "hot spots" without the need for nanoparticle aggregation, a highly valuable feature for SERS. However, their morphology also makes them more susceptible to changes such as aggregation or the rounding of sharp edges, which can lead to a gradual transformation into a more spherical shape if their stability is compromised. Such changes can significantly reduce their effectiveness in PoCT applications by negatively affecting their optical properties. [117], [118]

Additionally, it is important to assess any changes that may occur during transportation. Since the AgNS employed for this project were synthesized at the University of Porto and subsequently transported to NOVA University - FCT for further analysis and application, they may have been exposed to environmental conditions such as mechanical agitation or temperature fluctuations during transport. These factors can promote unwanted aggregation or morphological transformations.

To assess the stability of AgNS, we employed UV-Vis spectroscopy, focusing on localized surface plasmon resonance (LSPR) as an indicator of morphological integrity (section 1.2.2). LSPR is sensitive to changes in the size, shape, and environment of nanoparticles, making it a reliable tool for monitoring stability. A blue shift (to shorter wavelengths), is when the LSPR peak signals a transition towards a more spherical shape, indicating a loss of the star-like structure, which can diminish the optical properties necessary for diagnostic applications. Conversely, a red shift (to longer wavelengths), suggests particle aggregation, which is detrimental for bioconjugates formation. By continuously monitoring LSPR, we can evaluate the effects of various conditions, such as storage and stabilizing agents employed, on the stability of AgNS. This approach not only helps to understand the factors affecting stability but also provides valuable insights for optimizing synthesis, handling, and storage methods to preserve AgNS functionality in PoCT systems.

For this project, citrate was used as a stabilizing agent during the synthesis of AgNS, playing a role in preventing unwanted aggregation and maintaining the star-like morphology. [69] The negative charge of citrate enhances colloidal stability by promoting electrostatic repulsion between particles, avoiding aggregation. Moreover,

because citrate binds weakly to the surface of AgNS, it can be replaced by molecules with a higher affinity, ensuring long-term stability under different conditions. This makes citrate a good stabilizer for AgNS, maintaining both initial stability and subsequent modifications necessary for specific PoCT applications. [69]

To assess the stability of AgNS (0.05 nM) overtime, we first monitored their optical properties by measuring absorbance spectra at various time points. Figure 25 displays the absorbance spectra of AgNS over time, with 'P' denoting samples stored in plastic vials and 'G' for those in glass vials. The initial measurement (Day 0) corresponds to the day of synthesis in Porto, with all samples stored in plastic. From Day 8 onwards, AgNS were stored in both plastic and glass containers to investigate any potential influence of the storage material on the stability of the nanoparticles. The AgNS were stored at room temperature and shielded from light to minimize any external influences on stability. The UV-Vis spectra (Figure 25) show a peak at 380 nm across all experiments and time points, with minimal variation in wavelength (1-3 nm), indicating stable nanoparticle morphology over time. This stability suggests that the AgNS maintained their star-like morphology throughout the storage period. However, there are more noticeable changes in the absorbance values, which could be attributed to a decreasing concentration of AgNS in the vials as the colloidal solution was used for various tests. It is, therefore, recommended to mix the solution thoroughly before each use to ensure homogeneity and reproducibility of the results.

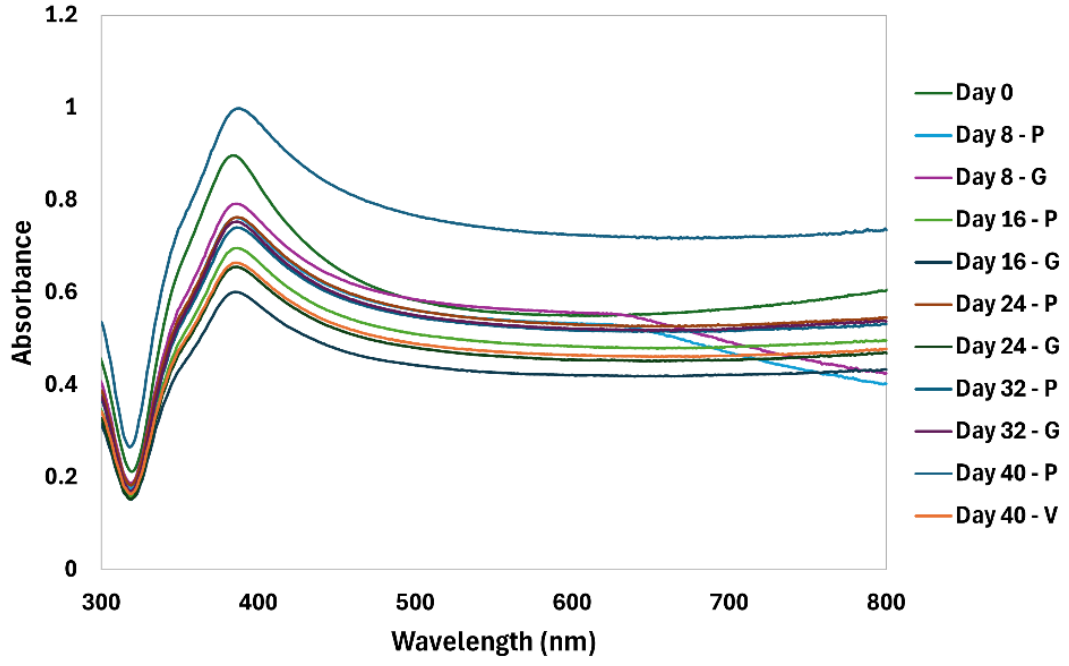

Figure 25. UV-Vis spectra of AgNS over a 40-day period in plastic (P) and glass (G) vials.

The LSPR peak positions over time (Figure 26) for both storage conditions exhibit minimal variations (1-3 nm). The LSPR peak positions remained consistent across storage conditions, indicating that both plastic and glass vials preserved AgNS

stability. For future PoCT applications, this suggests that either type of vial is suitable for storage, offering two possible options for handling and storage.

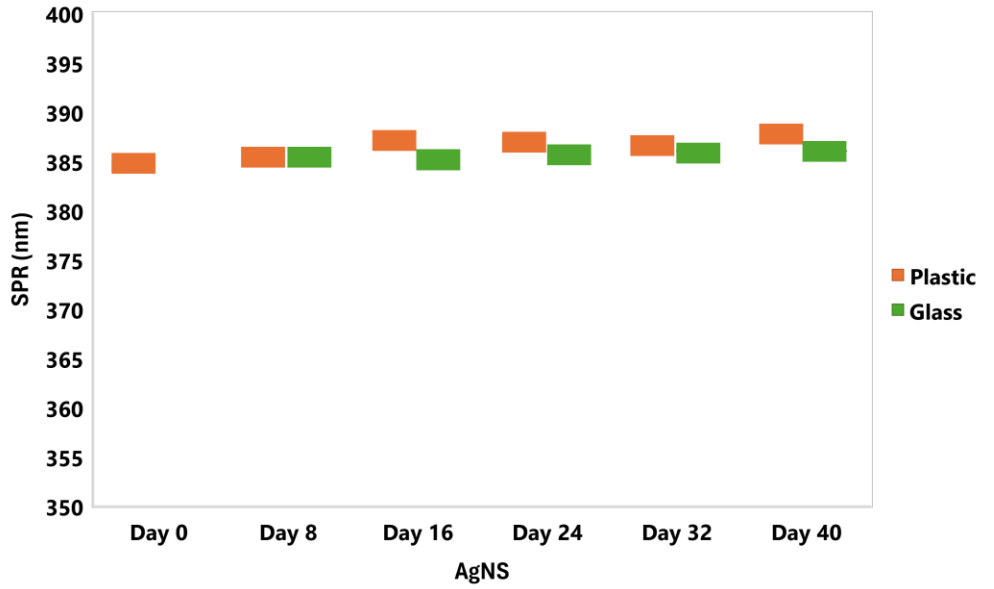

Figure 26. LSPR peak position of AgNS over time in plastic and glass vials.

Despite the overall stability observed in the AgNS stored in both vials, we noted some issues with aggregation in certain batches. Specifically, upon arrival at our laboratory, a noticeable red shift in the LSPR peak was observed, moving from 380 nm at synthesis to 385 nm, as shown in Figure 27. This red shift indicates an increase in particle size or clustering, which is consistent with nanoparticle aggregation. This was further supported by increased absorbance (yellow (b) and green line (c)) at longer wavelengths (400 to 700 nm), reflecting enhanced plasmonic interactions between aggregated particles.

The observed behavior in that batch may be attributable to a synthesis issue, a potential contamination problem. One plausible explanation is contamination with 4-Mercaptobenzoic acid (MBA), a Raman probe commonly used in the same laboratory to functionalize gold nanostars (AuNS) for labelled-SERS applications, that uses the same materials and equipment as the preparation of AgNS. If the AgNS batch was unintentionally contaminated with MBA, it could have altered the surface chemistry and stability of the silver nanostars. Given MBA's strong affinity for metal surfaces, it might have replaced citrate, the intended stabilizing agent, contributing to the observed aggregation. This possibility was also confirmed through SERS spectrum for this batch (see section A.1 in appendix A) where MBA signals (1079 cm^{-1} and 1583 cm^{-1}) appear to be present.

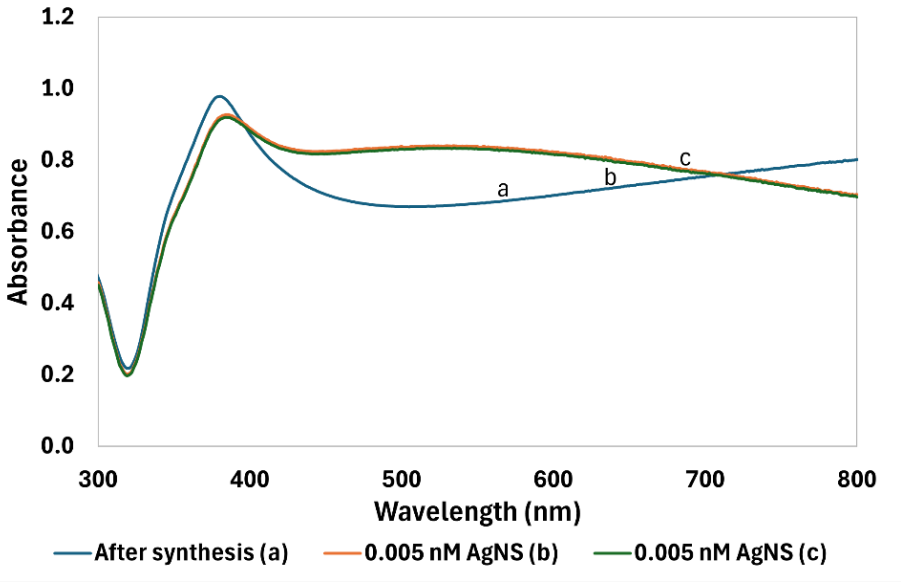

Figure 27. UV-Vis spectra of AgNS after synthesis and upon arrival at the laboratory. This figure compares the absorbance spectra of a new batch of AgNS measured after synthesis (a) and (b-c) upon arrival at the laboratory.

In conclusion, the colloidal stability of silver nanostars (AgNS) has been assessed over a 40-day period, demonstrating that they remain stable in both plastic and glass vials. Despite some aggregation observed in specific batches, likely due to contamination issues, the overall results suggest that the AgNS can effectively maintain their star-like morphology and optical properties during storage. This finding supports their potential for reliable applications in PoCT.

3.2 Optimization of HSA:AgNS Bioconjugates Ratios for SERS

To start exploring the potential use of the SERS technique in future PoC diagnostics, we focused on human serum albumin (HSA), the most prevalent protein in plasma. Testing a solution containing HSA allows refining SERS parameters and sample conditions more effectively, as it involves only a single protein, unlike plasma, which is a complex mixture of proteins.

For these experiments, we conjugated HSA with AgNS and incubated the mixture at 4°C overnight to facilitate AgNS-HSA interactions, protein corona formation, and protein stability. Biochemical characterization (DLS and AGE) of these HSA:AgNS bioconjugates are necessary for optimizing SERS detection parameters. This characterization simplifies the optimization of sample preparation and spectroscopy parameters, such as HSA concentration and bioconjugate stability, which are key for developing reliable PoC testing methods. Focusing on HSA also enables a detailed evaluation of HSA interactions, setting the stage for future research with other proteins and biomarkers.

In this chapter, six distinct ratios of HSA:AgNS bioconjugates were characterized by SERS, DLS and AGE analysis. The HSA:AgNS bioconjugates covered a wide range of concentrations, from 130:1 to 1.3E7:1 HSA:AgNS. These ratios were selected based on the HSA concentration found in blood (35 to 50 mg/mL), which corresponds to the highest ratio of 1.3E7:1. Starting with this ratio, we performed successive dilutions to identify where significant differences in the SERS spectra appeared.

3.2.1 SERS analysis

Following overnight incubation, samples were centrifuged for 10 minutes at 2500 g and 4°C to remove any unbound HSA and isolate the HSA:AgNS bioconjugates. The pellets were then resuspended in 20 μL of potassium phosphate buffer (KPB), pH 7.4, 20 nM. SERS spectra were subsequently measured for six distinct HSA:AgNS bioconjugates.

For SERS measurements (Figure 28), a 3 μL drop of each bioconjugate was placed on aluminium foil, and spectral acquisition was made almost immediately. Aluminium foil was chosen as the substrate to optimize the signal-to-noise ratio and ensure a consistent surface for high-quality observations. Additionally, aluminium foil provides a smooth, uniform, and non-reactive surface, minimizing interference from background signals. The measurement parameters included a 20x objective, a laser power of 10 mW, and 3 scans with an exposure time of 5 seconds each. Five spectra were obtained for each sample.

Control experiments (see A.2 in appendix) were conducted to account for any variations in the SERS signal due to environmental factors (substrate employed for sample placement) or sample preparation conditions (buffer, AgNS-only, HSA-only, and citrate, AgNS capping agent). However, no narrow bands or measurable peak areas were observed in these controls.

In Figure 28, the strongest signals, characterized by narrow bands and measurable peak areas, are observed at the lowest ratio (130:1 HSA:AgNS, dark blue spectrum), with notable peaks at 730 cm^{-1}, 925 cm^{-1}, 1015 cm^{-1}, 1075 cm^{-1}, 1180 cm^{-1}, and 1580 cm^{-1}, which may correspond to HSA vibrational modes. [119] This higher intensity at this ratio indicates stronger interactions between HSA and AgNS, which enhances SERS signal. As the HSA:AgNS ratio increases, the peak intensity decreases mainly due to the excess protein on the surface obstructing the emission of the SERS signal. When too much HSA is present, it absorbs light from the laser instead of allowing it to interact with the AgNS, which results in weaker SERS signals reaching the detector. Conversely, at lower concentrations (130:1 and 1300:1 HSA:AgNS, dark and light blue spectrum), there is less competition for binding sites, which facilitates more effective HSA-AgNS interactions. This leads to a more stable protein corona and improves SERS intensity.

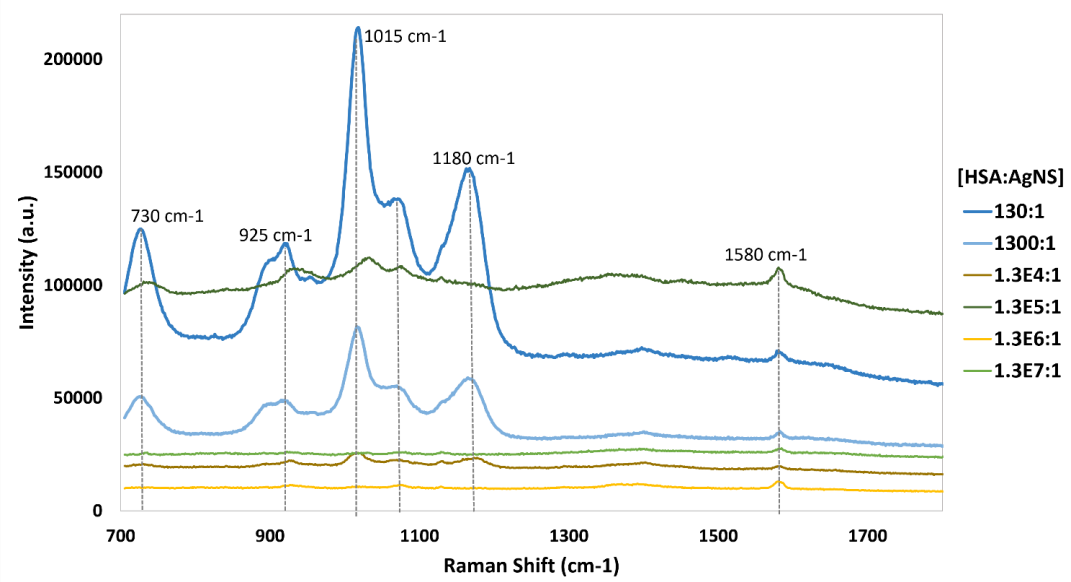

Figure 28. SERS spectra of varying HSA:AgNS ratios. The ratios vary by orders of magnitude, ranging from 130:1 to 1.3E7:1.

The results underscore the need to optimize HSA concentration for maximizing the SERS signal. The highest intensities were observed at HSA:AgNS ratios of 130:1 and 1300:1, suggesting these ratios are the most effective for enhancing the SERS signal and producing a clearer spectral profile. However, it is crucial to further evaluate the stability and functionality of the bioconjugates at these ratios. In section 3.4, we will investigate the optical and electrophoretic characteristics across ten different HSA ratios within this concentration range (130:1 – 1300:1 HSA:AgNS).

3.2.2 DLS analysis

The Z-average was used to analyze the hydrodynamic size of the samples and controls. The Polydispersity Index (PDI) will indicate the degree of dispersion in the solution, with values above 0.4 suggesting polydispersity, suggesting a wide size distribution among the particles. Colloidal stability is evaluated by a zeta potential greater than +30 mV or less than -30 mV. Each sample was measured 5 times, with duplicates prepared independently to ensure consistency and accuracy of the results. Zeta potential measurements were performed in triplicate for each duplicate.

Figure 29A illustrates the potential conjugation of HSA with AgNSs, possibly due to the formation of a protein corona.

The control sample of HSA, typically ranging from 5.9 to 6.2 nm in size, is provided in appendix A3. Figure 29B shows the hydrodynamic sizes (nm) of AgNS only and HSA:AgNS bioconjugates. The Z-average size of the AgNS-only control sample is approximately 90 nm, serving as a reference for bioconjugates formed at different HSA:AgNS ratios. AgNSs exhibited a PDI below 0.3 (Table 2), indicating a monodisperse system.

As HSA:AgNS ratio increased, the hydrodynamic size also increased, reaching 92 nm at a 1300:1 HSA:AgNS ratio, and continued to grow at higher ratios, measuring 105 nm (1.3E4:1), 117 nm (1.3E5:1), 121 nm (1.3E6:1), and 150 nm (1.3E7:1). This pattern suggests that higher HSA concentrations lead to more extensive protein binding, resulting in larger bioconjugates. The significant size increase at higher ratios likely reflects more extensive protein corona formation and potential aggregation, as indicated by the substantial size increase observed at the 1.3E7:1 ratio, where aggregation seems to intensify. These changes might be attributed to the irregular shape of AgNSs, which can facilitate uneven protein binding and increase aggregation tendencies at higher protein concentrations.

The error bars represent the standard deviation, with smaller bars indicating consistent measurements across experiments, except at the highest HSA:AgNS ratio (1.3E7:1), where increased variability is likely due to aggregation. The larger standard deviation at the lowest ratio (130:1) may be attributed to incomplete corona formation or experimental error, leading to less uniform particle sizes and less stable measurements.

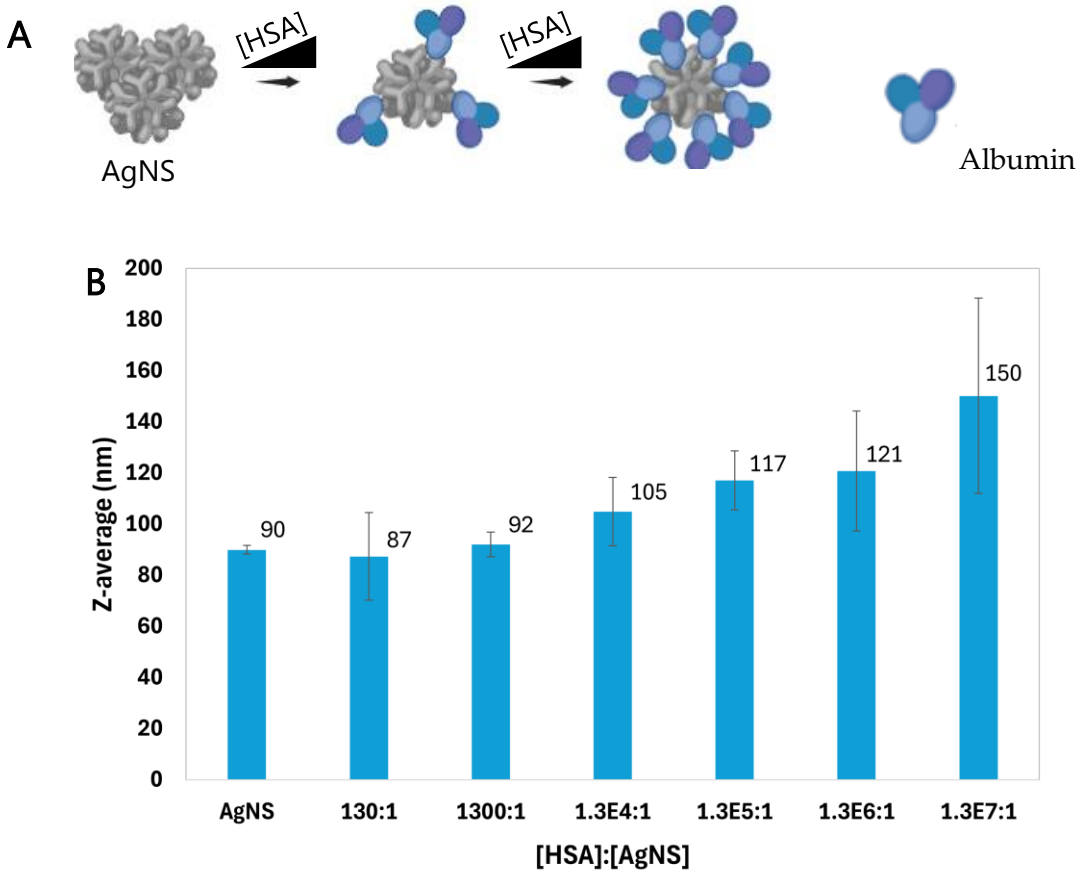

Figure 29. A. Illustration of protein corona formation on AgNS with increasing HSA concentration. **B.** Z-average (in nm) of AgNS alone and in various ratios of HSA:AgNS bioconjugates.

Table 2. Polydispersity index (PDI) values for HSA:AgNS bioconjugates across different ratios.

[HSA]:[AgNS]	Polydispersity index (PDI)					Average	SD
0 (AgNS)	0.108	0.257	0.372	0.294	0.053	0.217	0.12
130:1	0.099	0.251	0.026	0.044	0.241	0.132	0.10
1300:1	0.116	0.129	0.071	0.289	0.019	0.125	0.09
1.3E4:1	0.109	0.305	0.162	0.095	0.114	0.157	0.08
1.3E5:1	0.185	0.16	0.05	0.635	0.242	0.254	0.20
1.3E6:1	0.128	0.251	0.108	0.286	0.103	0.175	0.08
1.3E7:1	0.272	0.34	0.21	0.113	0.105	0.208	0.09

The PDI values for bioconjugates with varying ratios of HSA:AgNS, as well as for AgNS alone, are summarized in Table 2. Each entry corresponds to an individual measurement of the same sample. If the standard deviation (SD) is significant, it indicates that aggregation occurred during the measurements. For AgNS alone, the PDI ranges from 0.053 to 0.372, indicating a reasonably uniform size distribution, which serves as a baseline for comparison. At most HSA:AgNS ratio, PDI values show moderate consistency, indicating a minimal impact on size homogeneity. However, at a 1.3E5:1 ratio, one measurement yielded a PDI of 0.635, indicating that aggregation occurred during that measurement.

Figure 30 presents the zeta potential measurements of bioconjugates formed at different ratios of HSA:AgNS, alongside the values for AgNS alone. The AgNS control exhibits a highly negative zeta potential of -78 mV, indicating strong stability. However, as the HSA:AgNS ratio increases, the zeta potential becomes progressively less negative, suggesting a gradual reduction in stability. At the highest ratios, the zeta potential is still much lower than the AgNS control, indicating further destabilization.

The reason for this trend when increasing the HSA:AgNS ratios, is due to the interaction between AgNS and HSA that leads to a decrease in the negative zeta potential. At physiological pH (7.4), HSA carries a net negative charge due to its isoelectric point of 4.7. When HSA adsorbs onto the AgNS surface, its negatively charged groups partially neutralize the AgNS charge, reducing the overall negative zeta potential. [120] As the concentration of HSA rises, it forms a protein corona around the AgNS, which shields the surface charge and creates a more neutral surface environment. This protein layer alters the electrostatic environment, potentially exposing positive regions of HSA, contributing to a further reduction in zeta potential and affecting colloidal stability by promoting particle aggregation. [93]

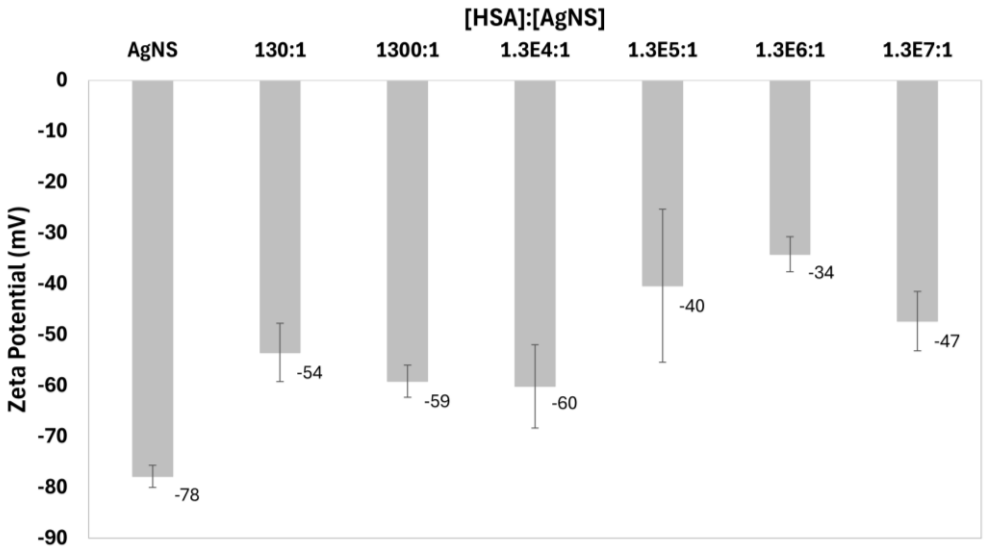

Figure 30. Zeta potential (mV) of AgNS and HSA:AgNS bioconjugates at various ratios.

In this section, we identified the lowest HSA:AgNS ratios (130:1 to 13000:1) as optimal due to their superior stability (indicated by higher zeta potential), reduced aggregation (lower PDI), increased hydrodynamic size, and enhanced SERS characteristics, including narrow bands, low background noise, measurable peak areas, and a distinct spectral profile. These findings suggest that these ratios offer the best balance of stability and SERS performance, making them suitable for further applications.

3.2.3 AGE analysis

Agarose is a linear polymer that forms a three-dimensional network when cooled, with channel sizes ranging from 50 to over 200 nm. This structural property makes agarose ideal for Gel Electrophoresis (AGE), which we used to analyze the size, aggregation behavior, and protein corona formation in bioconjugates of AgNS with HSA. By analyzing variations in electrophoretic mobility (Δμ), AGE helps characterize the bioconjugates based on their charge and mass.

The electrophoretic mobility (Δμ) of the HSA bioconjugates was measured and analyzed using Hill's model, which describes how a ligand binds to a macromolecule in relation to the concentration of the ligand. [121] This approach provides insights into the binding dynamics at different HSA:AgNS ratios. The electrophoretic mobility (Δμ) is calculated using the following equation:

$$\Delta\mu = \frac{\Delta\mu_{max} \cdot x^n}{K_D^n + x^n}$$

Equation 3

where $\Delta\mu_{max}$ represents the maximum electrophoretic mobility, x denotes the concentration of the binding ligand (such as HSA), K_D is the dissociation constant of the binding interaction, and n is the Hill coefficient, which indicates the degree of cooperativity in the binding process.

In the gel (Figure 31A), pure AgNS, corresponding to the first well, exhibited the lowest mobility. This reduced mobility can be attributed to the presence of citrate, the capping agent used during synthesis. Citrate imparts a higher negative charge to the AgNS, enhancing electrostatic repulsion between particles. Additionally, the observed low mobility could also be due to aggregation that may have occurred after centrifugation. Table 3 lists the HSA:AgNS ratios along with the corresponding HSA amounts (nM), representing the bioconjugates in order of increasing ratios. Although the AgNS were negatively charged due to their citrate stabilization layer, the addition of HSA altered both the charge and mass of the bioconjugates. This change was evident in the electrophoretic mobility, where migration distance correlated with the net surface charge and mass of the bioconjugates. The bioconjugates with the highest mobility were those with HSA ratios of 1E4:1, followed by 2E4:1, 1E5:1, and 2E5:1, showing a trend of decreasing mobility as the HSA concentration increases. This suggests that higher HSA content reduces electrophoretic mobility, as HSA carries a lower negative charge compared to the citrate in AgNS alone.

The AgNS control and the bioconjugates displayed noticeable migratory lag, likely due to its star-shaped structure, which can cause tip loss and affect movement. At the lowest HSA:AgNS ratios (62:1 and 620:1), some aggregation is observed at the wells, as indicated by the more intense color at the beginning of the band. The larger size of these aggregates can hinder their ability to migrate through the gel matrix, resulting in the observed lag and increased band intensity at the origin.

Hill's model (Figure 31B), fitted the electrophoretic mobility data with a binding constant (K_D) of 8994 nM, Hill coefficient (n) of 1.1, and r^2 value of 96%. The K_D value indicates a relatively high affinity between HSA and AgNS, suggesting that the binding interactions are strong. The Hill coefficient greater than 1 suggests positive cooperativity, meaning the binding of one HSA molecule to AgNS facilitates the binding of additional molecules, which could have implications for the stability and size of the bioconjugates. This cooperativity may significantly influence the stability and size of the bioconjugates, as increased binding could lead to more extensive protein coronas and potentially affect their overall behavior in biological applications. The $\Delta\mu_{max}$ value was 1.5E-07 $m^2 V^{-1} s^{-1}$. When compared to the gel from this reference [122], where this values was 3.1E-08 $m^2 V^{-1} s^{-1}$, it is evident that the binding of HSA to AgNS significantly enhances the electrophoretic mobility. This higher Δμmax indicates a stronger interaction between HSA and AgNS. However, these values cannot be directly compared, as they correspond to the binding of AuNS to MBA, which involves different surface chemistry and binding dynamics. Despite the differences, the comparison serves to highlight the relative strength of interactions

within similar bioconjugate systems, providing insights into the behavior of HSA-AgNS complexes.

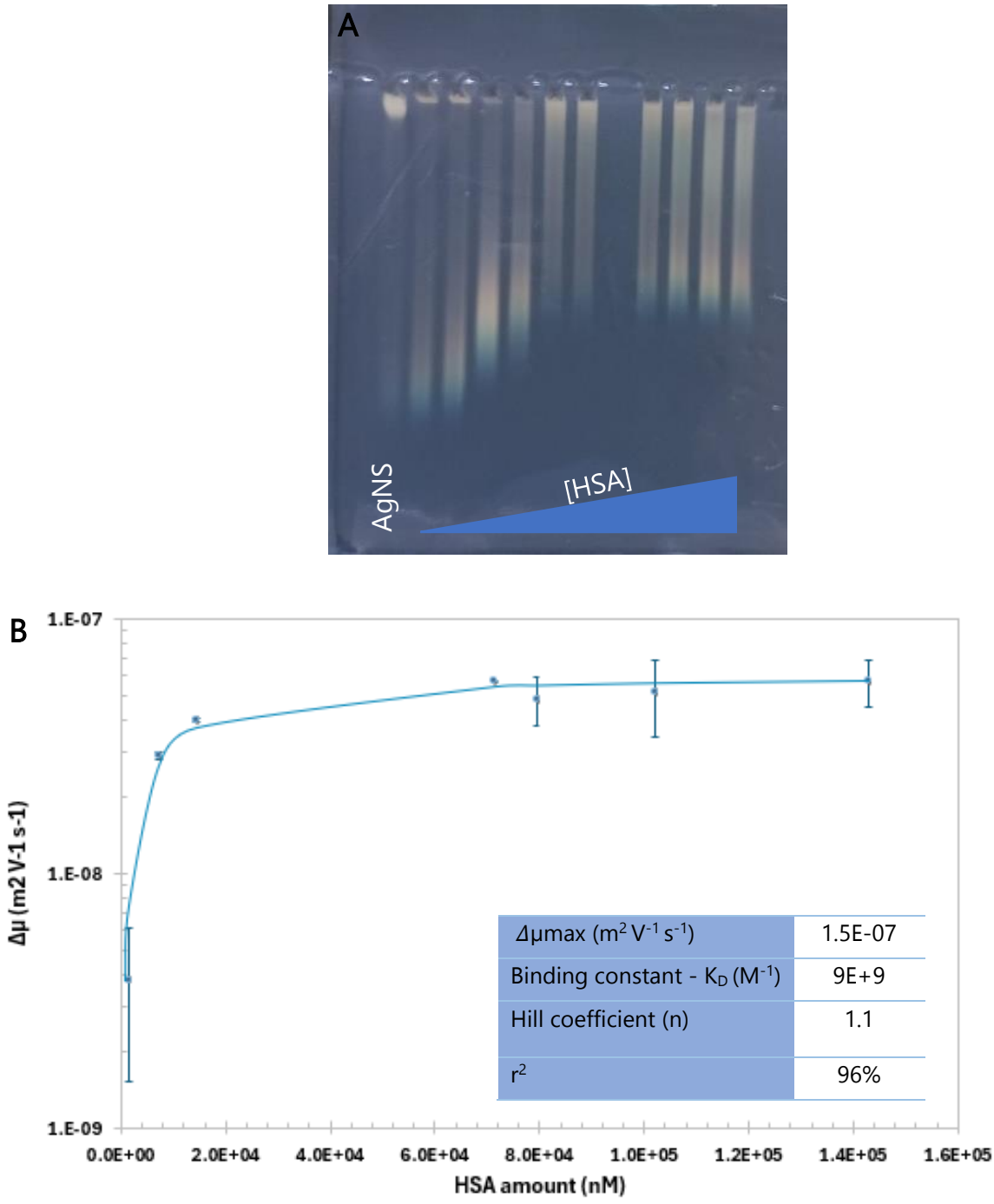

Figure 31. A. Agarose gel electrophoresis (AGE) of HSA bioconjugates at different molar ratios. The gel image displays the migration pattern of the HSA complexes, where each lane corresponds to a different molar ratio of HSA to AgNS. **B**. Hill's model fitting curve for the electrophoretic mobility of HSA bioconjugates. The graph shows the variation in electrophoretic mobility (Δμ) as a function of the molar ratio of HSA to AgNS. Data obtained from this fitting is presented in the table.

Table 3. HSA amounts (nM) at different HSA:AgNS ratios.

[HSA]:[AgNS]	HSA amount (nM)
1.0E+4:1	7.14E+02
2.0E+4:1	1.43E+03
1.0E+5:1	7.14E+03
2.0E+5:1	1.43E+04
1.0E+6:1	7.14E+04
1.1E+6:1	7.94E+04
1.5E+6:1	1.02E+05
2.0E+6:1	1.43E+05
5.1E+6:1	3.57E+05
1.0E+7:1	7.14E+05

The results of this section, including the Hill coefficient of 1.1 and the migration patterns observed in the AGE gel, indicate that conjugation between HSA and AgNS is taking place, as evidenced by modifications in charge and size compared to AgNS alone. This is further supported by the observed increase in hydrodynamic size and distinct changes in the SERS spectra. Together, these findings confirm successful bioconjugate formation and underscore the impact of HSA binding on the physical and chemical properties of AgNS.

3.3 Optimization of Plasma concentration for SERS

The aim of this section is to optimize the concentration of human plasma for effective SERS analysis, following the same analysis as in the previous section for HSA. Plasma samples are commonly used in the diagnosis of various conditions, such as stroke. [29], [123], [124] The initial characterization of human plasma proteins will aid in identifying the optimal plasma:AgNS ratios for developing effective point-of-care (PoC) testing applications. The use of commercially available "generic" human plasma allows for a controlled and reproducible simulation of SERS detection, allowing optimization of PoC diagnostic procedures without spending patient samples.

In this section, we developed a method for the preliminary characterization of plasma bioconjugates, employing a range of spectroscopic techniques, including SERS, DLS, UV-Vis spectroscopy, AGE, and SDS-PAGE.

3.3.1 SERS analysis

SERS spectra of human plasma are inherently complex due to the diverse array of proteins present, each contributing to overlapping vibrational bands. This complexity makes it challenging to assign specific vibrational bands to individual proteins. Therefore, statistical methods such as Principal Component Analysis (PCA) are essential for analyzing SERS spectra of plasma bioconjugates. Through this statistical analysis (section 3.6), it is possible to compare the spectral profiles of plasma bioconjugates with those of HSA bioconjugates, enabling us to identify statistically significant differences in their spectral features.

Plasma:AgNS were incubated overnight at 4°C. Following incubation, the bioconjugates were centrifuged for 10 minutes at 2500 g and 4°C to remove any unbound plasma and isolate the plasma:AgNS bioconjugates. The pellets were then resuspended in 20 μL of ultra-pure water. SERS spectra were subsequently measured for six distinct bioconjugates.

For SERS measurements (Figure 31), a 3 μL drop of each bioconjugate at different ratios, ranging from 97:1 to 9.7E4:1, was placed on aluminum foil, and spectral acquisition was performed almost immediately. Aluminum foil was chosen for the same reason as mentioned in the previous section. The measurement parameters included a 20x objective, a laser power of 50 mW, and 3 scans with an exposure time of 5 seconds each. Five spectra were obtained for each sample.

In Figure 31 two ratios are missing, namely, 9.7E5:1 and 9.7E6:1 (see appendix A4), as the SERS intensity was higher, but there were no narrow bands or measurable peak areas in the SERS spectra. In appendix A3, a SERS spectrum of plasma on aluminium foil and on a glass slide, both showing a flat spectrum. The obtained spectra exhibit distinct SERS lines with key peaks labeled at 928 cm^{-1}, which seem to correspond to HSA and transferrin; 1129 cm^{-1}, attributed to hemoglobin; and 1180 cm^{-1}, which may correspond to either hemoglobin or HSA (Figure 31). These peaks are associated with the vibrational modes of the proteins present in plasma. [119] The other vibrational lines (1033 cm^{-1}, 1306 cm^{-1} and 1398 cm^{-1}) observed in the spectra may correspond to additional plasma proteins, the signals of which have not been found in the literature, or they may arise from the superposition of vibrational lines from different proteins due to their presence during the incubation period.

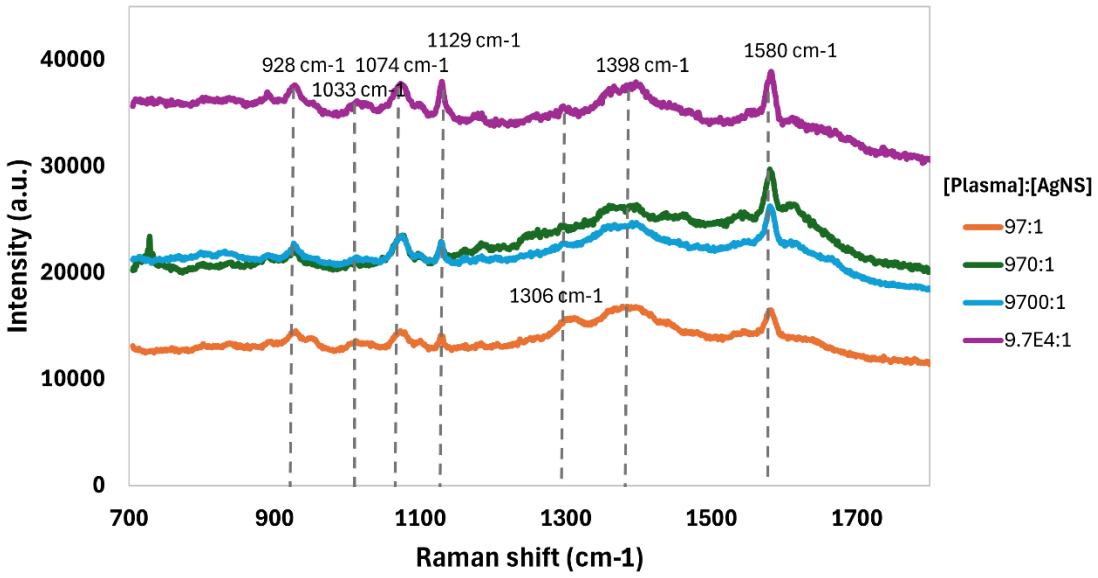

Figure 31. SERS spectra of plasma (human plasma) and AgNS bioconjugates at varying ratios on an aluminium foil substrate. The ratios vary by orders of magnitude, ranging from 9.7E7:1 to 9.7E4:1.

The SERS signal intensity varies across the different ratios, with the maximum intensity observed at the 9.7E4:1 ratio.

As plasma concentration increases, there is noticeable broadening of some peaks, particularly at 1074 cm^{-1} and 1580 cm^{-1}, that may correspond to the AgNS. The peak at 1033 cm^{-1}, which is more prominent in the spectra of higher plasma concentrations, diminishes with decreasing plasma concentration, potentially due to competitive binding or saturation effects on the AgNS surface. This peak could also be related to fibrinogen. [119]

In conclusion, evaluating the stability of the bioconjugates at this ratio is necessary. However, it is essential to thoroughly assess the stability and functionality of the bioconjugates at this ratio. Further investigation is needed, specifically regarding the optical and electrophoretic characteristics, as the SERS spectra of the different ratios appear very similar. We will continue to explore these aspects for ten plasma ratios within this concentration range (section 3.5).

3.3.2 DLS Analysis

Figure 32A, is a schematic representation of protein corona formation around AgNS as plasma protein concentration increases. DLS data in Figure 32B show the Z-average hydrodynamic size of AgNS and their bioconjugates with plasma at ratios ranging from 97:1 to 9.7E6:1. Each sample was measured 5 times, with duplicates prepared independently to ensure consistency and accuracy of the results. Zeta potential measurements were performed in triplicate for each duplicate.

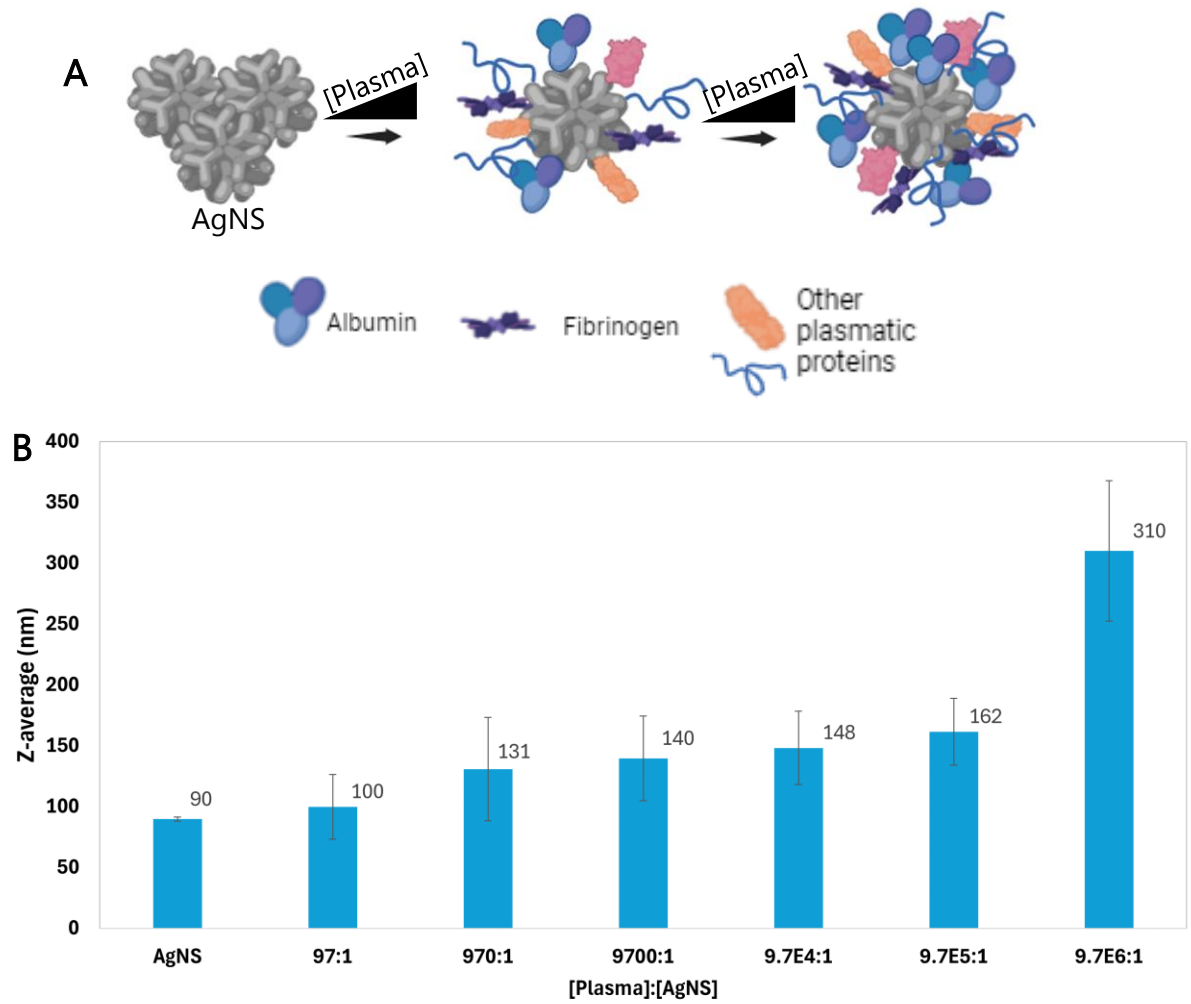

Figure 32. A. Illustration of protein corona formation on AgNS with increasing plasma concentration **B.** Z-average (in nm) of AgNS and increasing plasma:AgNS ratios in the 97:1 to 9.7E6:1 range.

Silver nanostars alone, present a Z-average size of approximately 90 nm, serving as a reference for comparison with plasma:AgNS bioconjugates. At the lowest plasma:AgNS ratio of 97:1, the hydrodynamic size increases slightly to 100 nm, but remaining constant within experimental error, hinting at initial binding of plasma proteins to the AgNS surface and the formation of a thin protein corona with a minor impact on overall particle size. As plasma concentration increases, the hydrodynamic size grows progressively: reaching 131 nm at 970:1, 140 nm at 9700:1, and 148 nm at 9.7E4:1, reflecting the formation of an increasingly thicker protein corona. At the higher ratio, the size increases more markedly, reaching 310 nm. Supporting this observation, the distribution graph of the sizes for the two highest plasma:AgNS ratios (9.7E5:1 and 9.7E6:1) is presented in Figure 33, illustrating a notable increase in size at the highest ratio (9.7E6:1). This dramatic increase is likely due to extensive aggregation or the formation of large protein complexes on the AgNS surface.

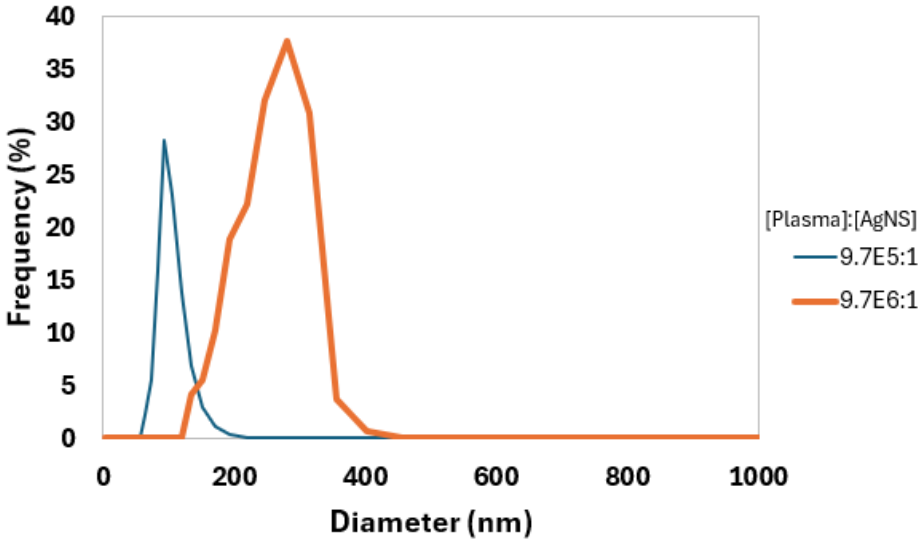

Figure 33. Distribution graph of the hydrodynamic sizes (nm) for the two highest plasma:AgNS ratios (9.7E5:1 and 9.7E6:1).

Error bars in Figure 32B indicate the standard deviation, highlighting variability in the measurements. Notably, larger error bars at higher plasma concentrations, especially at the 9.7E6:1 ratio, suggest significant variability in hydrodynamic size, likely due to heterogeneous aggregation or uneven protein corona formation, as previously observed in Figures 32 and 33. PDI data (Table 4) revealed variations in size distribution across different plasma:AgNS ratios during the measures, but none was greater than 0.4, so monodispersity is mantained across the measurments. AgNS alone exhibits moderate dispersity with PDI values ranging from 0.093 to 0.231. As plasma concentration increases, PDI values fluctuate, indicating a mix of uniform and heterogeneous bioconjugates.

Table 4. Polydispersity index (PDI) of AgNS and Plasma bioconjugates.

[Plasma]:[AgNS]	Polydispersity index (PDI)						Average	SD
0 (AgNS alone)	0.231	0.112	0.093	0.093	0.154	0.137	0.144	0.05
97:1	0.047	0.048	0.197	0.045	0.317	0.131	0.145	0.10
970:1	0.295	0.293	0.022	0.101	0.023	0.147	0.148	0.11
9700:1	0.022	0.325	0.02	0.293	0.102	0.152	0.149	0.12
9.7E4:1	0.276	0.021	0.02	0.208	0.269	0.159	0.148	0.11
9.7E5:1	0.351	0.017	0.325	0.019	0.113	0.165	0.142	0.13
9.7E6:1	0.213	0.017	0.129	0.127	0.109	0.119	0.119	0.06

Figure 34 shows the zeta potential measurements for AgNS and various bio-conjugate samples at different plasma:AgNS ratios (97:1 to 9.7E6:1). AgNS-only have a significantly negative zeta potential of -72 mV, indicating a highly stable colloidal

suspension due to strong electrostatic repulsion between the nanoparticles. As plasma is progressively added to AgNS, forming bioconjugates, the zeta potential becomes less negative, suggesting a gradual masking of the nanoparticles' surface charge by plasma proteins. This protein adsorption reduces electrostatic repulsion between nanoparticles, which may increase the likelihood of aggregation at higher plasma concentrations, as evidenced by the less negative zeta potentials.

The stable zeta potential values observed from the 9700:1 ratio onwards might suggest a saturation point where additional plasma does not significantly alter the surface charge, indicating a limit to protein binding on the nanoparticle surface.

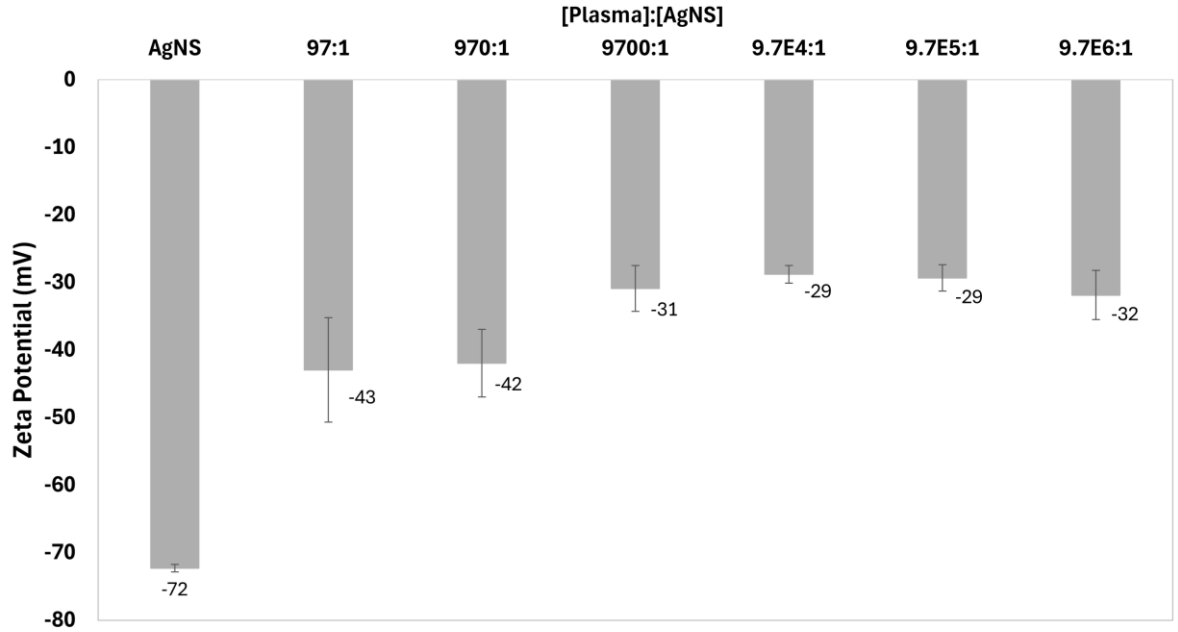

Figure 34. Zeta potential (mV) of AgNS and plasma:AgNS bioconjugates at various ratios. The zeta potential is plotted on the y-axis, while the x-axis represents the different HSA:AgNS ratios.

In summary, the results indicate that the 970:1 and 9700:1 plasma:AgNS ratios exhibit an increase in size, accompanied by low standard deviation (SD) in the PDI values, which are approximately 0.11 (with PDI values below 0.3). This suggests monodispersity and a higher negative zeta potential, reflecting enhanced stability.

3.3.3 AGE Analysis

Figure 35A presents plasma:AgNS bioconjugates in the gel, with each gel lane representing increasing plasma concentrations in the range from 1.0E4:1 to 5.1E6:1. Table 5 shows the corresponding amount of protein for each lane. Plasma concentrations in each case were estimated according to the method presented in section 2.2.8.1. Figure 35B shows AGE data fitted to Hill's model, illustrating variations in electrophoretic mobility ($\Delta\mu$) in relation to the molar ratios of plasma:AgNS bioconjugates. The migration patterns vary across the lanes, reflecting differences in size and charge of

the bioconjugates. Reduced migration indicates larger or aggregated bioconjugates with lower net charge, while extensive movement suggests smaller bioconjugates with a stronger negative charge.

Figure 35B shows that $\Delta\mu$ increases with lower plasma concentrations, which can be attributed to the strong interactions between AgNS and plasma proteins, leading to the formation of a protein corona. The initial lag in the bands suggests that the AgNS have variable shapes and bind to different plasma proteins, resulting in heterogeneous attachment. As the plasma concentration continues to rise, the curve plateaus, indicating saturation of the available binding sites on AgNS, consistent with Hill's model of binding affinity and cooperative interactions. This suggests the formation of a stable, dense protein layer around the AgNS, where further increases in plasma concentration do not significantly impact mobility.

At lower plasma:AgNS ratios, aggregation seems evident, as seen by the accumulation of bioconjugates in the wells, implying that larger aggregates have limited mobility. The first well, containing citrate-capped AgNS, exhibits no migration; however, this electromobility seems to correspond primarily to the citrate, as some of the AgNS may have remained adhered to the well.

Key parameters from the Hill fitting curve, shown in Figure 35B, describe the binding between AgNS and plasma proteins observed in the AGE experiment. The maximum value of $\Delta\mu$, determined to be 1.24×10^{-7} $m^2/V{\cdot}s$, reflects the extent of protein binding to the AgNS surface. A higher $\Delta\mu$ indicates a greater interaction between the plasma proteins and the AgNS, suggesting a more substantial protein layer on the nanoparticle surface.

The binding constant (K_D), calculated at 30150 nM, indicates a moderate affinity between plasma proteins and AgNS; lower K_D values would suggest stronger binding interactions. This moderate affinity suggests that while the plasma proteins are able to bind to the AgNS surface, they are not as strongly attached as would be indicated by a lower K_D.

The Hill coefficient (n) of 0.7 implies negative cooperative binding, meaning that the binding of one protein molecule to the AgNS surface decreases the likelihood of additional protein binding. This phenomenon may be attributed to steric hindrance, where the physical presence of one bound protein restricts access for others.

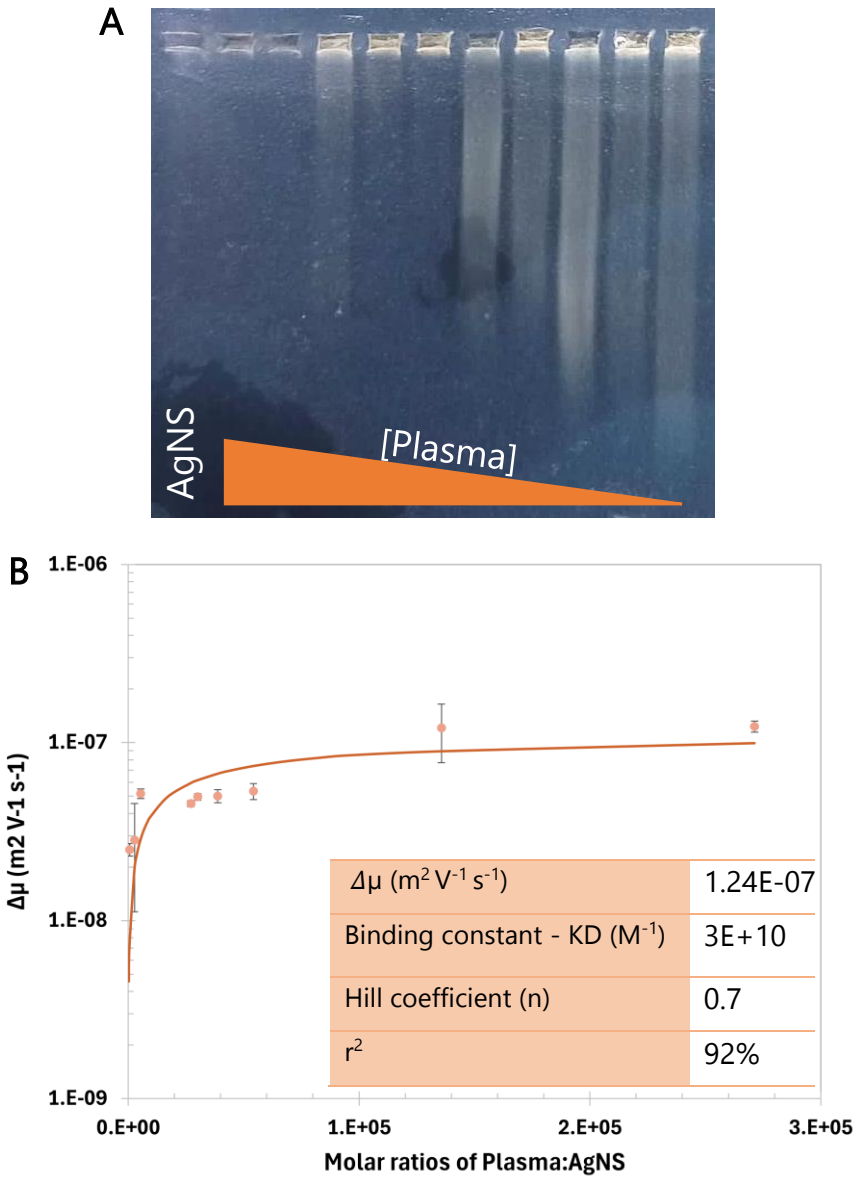

Figure 35. A. AGE image of plasma conjugated with AgNS at varying ratios. **B.** AGE data fitting to Hill's model, and table with the obtained data from the model.

Table 5. Plasma amounts at different Plasma:AgNS ratios.

[Plasma]:[AgNS]	Plasma protein amount (nM)
1.0E+4:1	2.71E+02
2.0E+4:1	5.43E+02
1.0E+5:1	2.71E+03
2.0E+5:1	5.43E+03
1.0E+6:1	2.71E+04

1.1E+6:1	3.01E+04
1.5E+6:1	3.88E+04
2.0E+6:1	5.43E+04
5.1E+6:1	1.36E+05

Overall, the findings from electrophoretic light scattering and AGE highlight the complexity and variability of bioconjugate formation across different plasma concentrations, complementing the SERS data. We identified the lowest plasma:AgNS ratios (97:1 to 9700:1) as optimal due to their superior stability, indicated by higher zeta potential, reduced aggregation (lower PDI), and increased hydrodynamic size. Additionally, these ratios exhibited enhanced SERS characteristics, including distinct narrow bands, low background noise, measurable peak areas, and a unique spectral profile. Collectively, these results suggest that these ratios offer an ideal balance of stability and SERS performance for further applications.

3.4 Characterization of 10 Selected HSA:AgNS Ratios from Initial Screening

Since the optimal ratios of HSA:AgNS bioconjugate found in 3.2 were ranging from 130:1 to 1300:1, this section explores the characterization of ten distinct HSA:AgNS bioconjugate ratios (from 130:1 to 1300:1) using a combination of electrophoretic light scattering and spectroscopic methods, including UV-Vis spectroscopy and SERS. Moreover, testing different substrates for sample placement in SERS was also performed.

3.4.1 SERS analysis

SERS spectra were obtained on aluminium foil and various paper substrates with printed wells to identify the substrate that provides the highest SERS intensity, measurable peak areas, and a well-defined SERS profile. Spectra obtained on paper substrates were obtained through five separate applications, each with a 3 μL sample volume. Spectral measurements were taken immediately after the fifth application to capture the “wet” sample state, and again after drying to record the "dry" state spectra. This approach aimed to enhance bioconjugate concentration on the substrate, improving signal detection and replicating real-world sample conditions. The ten HSA:AgNS ratios allowed for a thorough assessment of SERS signal intensity and spectral characteristics across a broad range of these ratios. The measurement parameters included a 20x objective, a laser power of 50 mW, and 3 scans with an exposure time of 5 seconds each. Five spectra were obtained for each sample.

3.4.1.1 Aluminium substrate

Across all investigated ratios, SERS spectra of the wet samples of the ten HSA:AgNS bioconjugate ratios on an aluminium substrate (Figure 36) exhibited similar spectral characteristics, including good signal-to-noise ratios and spectral profiles comparable to those obtained for the SERS spectra on aluminium foil in section 3.2 (Figure 28). The consistent spectral quality across these ratios indicates that the chosen range is suitable for SERS detection of bioconjugates. Intense vibrational bands are observed at 730 cm^{-1}, 925 cm^{-1}, 1015 cm^{-1}, and 1180 cm^{-1}, which correspond to vibrational modes of HSA and AgNS seen in section 3.2. Among all the spectra, the prominent peak at 1015 cm^{-1} has the highest intensity, suggesting significant SERS at this vibrational mode, characteristic of HSA. Additionally, the peak at 1075 cm^{-1} and 1580 cm^{-1} is noteworthy for its distinct and well-defined profile, as these peaks could be from AgNS.

The overall consistency and repeatability of the spectral profiles in the figure confirm that the aluminium substrate is a suitable choice for SERS analysis of these bioconjugates, enabling clear and reproducible spectra necessary for further qualitative evaluations.

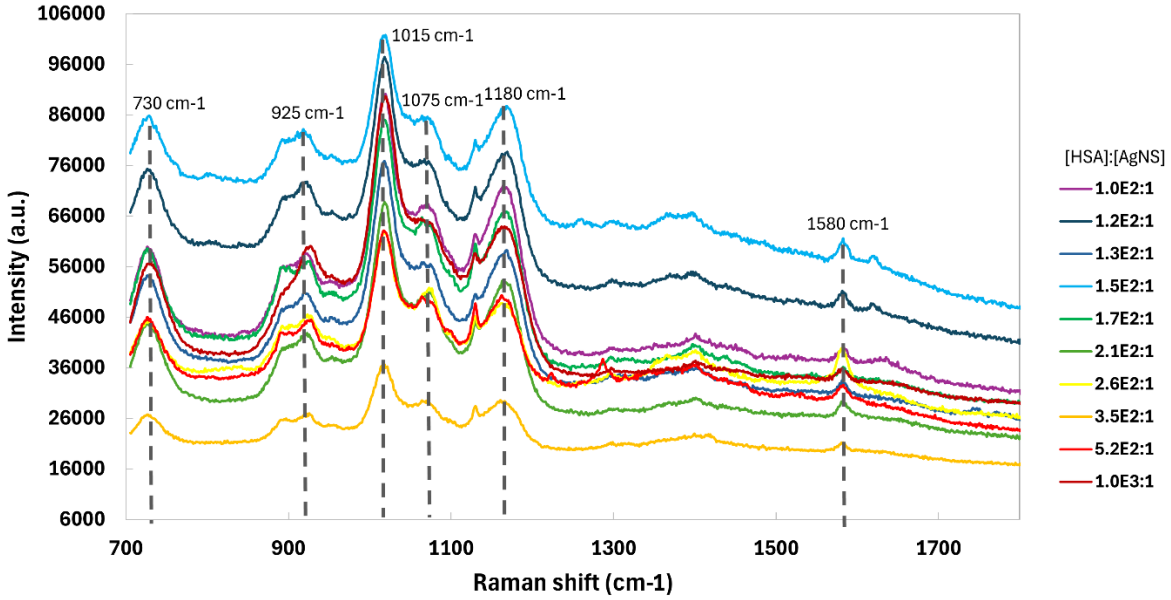

Figure 36. SERS spectra of the 10 different ratios HSA:AgNS on aluminium foil. The HSA:AgNS ratios range from 62:1 to 620:1.

3.4.1.2 Photocopy paper substrate

The SERS spectra of the ten HSA:AgNS bioconjugate ratios in their wet state are shown in Figure 37A, while the SERS spectra of the same ratios after drying on the photocopy paper substrate are presented in Figure 37B. A control Raman spectra of photocopy paper is presented in Figure A10 in appendix A5, with no narrow bands or measurable peak areas observed.

In the wet state (Figure 37A), the drop the drop retains its curvature, the SERS spectra exhibit strong, distinct peaks with high signal intensity and area; the most prominent peak across all ratios is observed at 1015 cm^{-1}. Additional significant peaks are seen at 730 cm^{-1}, 925 cm^{-1}, and 1180 cm^{-1}, which correspond to known vibrational modes of HSA, as detailed in section 3.2. The peaks at 1075 cm^{-1} and 1580 cm^{-1} may originate from the AgNS.

The SERS vibrational lines observed on this paper substrate are similar to those detected on the aluminum substrate (compare spectra in Figures 37 and 36, respectively); however, the overall intensity, is significantly higher, ranging from 400,000 a.u. on the paper substrate to 90,000 a.u. on the aluminum substrate (1000:1 HSA:AgNS). This suggests that the photocopy paper substrate may enhance the SERS effect, possibly due to its absorbent nature and the presence of wells in the paper that concentrate the sample. This approach could work even better in a PoC test, where a simple, low-cost, and efficient substrate that produces higher SERS signal is necessary for rapid diagnostics.

When comparing the SERS spectra of the HSA:AgNS bioconjugates obtained on the photocopy paper substrate in its wet state to those in its dried state, several key differences emerge. In the dried state (Figure 37B), the spectra generally exhibit a decrease in intensity across all the HSA:AgNS ratios, particularly noticeable in the higher intensity peaks around 1015 cm^{-1} and 1580 cm^{-1}. This reduction in intensity suggests that the drying process may lead to a redistribution or aggregation of the bioconjugates on the photocopy paper substrate, potentially reducing the uniformity of the SERS signal.

In addition, the dried samples exhibit broader peaks in certain regions, a feature that is less prominent in the wet samples. This broadening may result from changes in the local environment of the bioconjugates as they dry, including potential alterations in protein structure or the formation of a more heterogeneous and uneven layer on the substrate. These modifications can lead to less defined and more diffuse SERS lines, complicating the spectral interpretation and potentially reducing the precision of SERS-based analyzes.

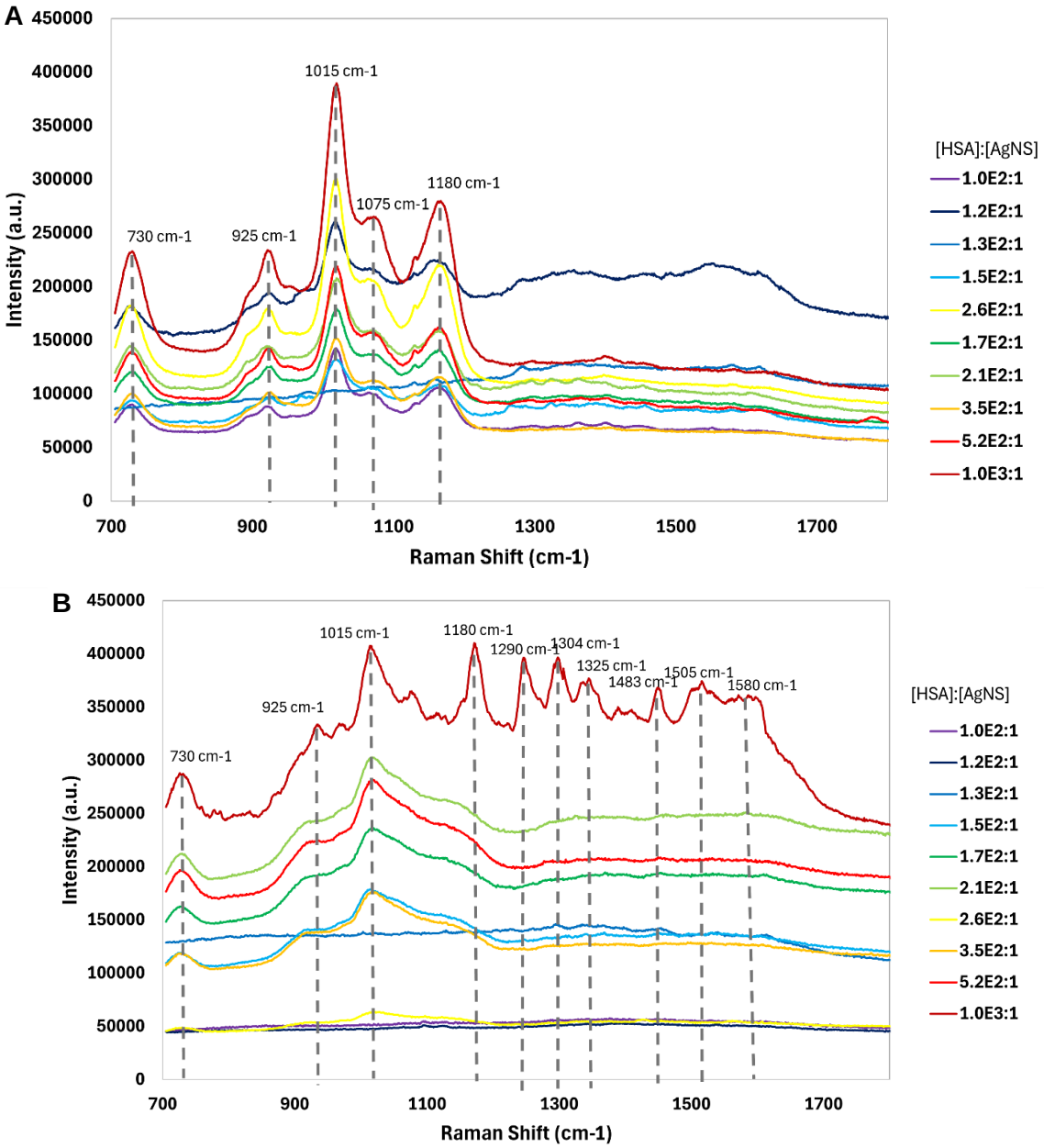

Figure 37. A. SERS spectra of HSA:AgNS conjugates on photocopy paper after adding the last drop. **B**. SERS spectra of HSA:AgNS conjugates on photocopy paper after the last drop was added and dried.

In summary, the wet samples generally yield higher signal intensities and more defined spectral features compared to the dried samples. Although the dried samples exhibit reduced intensity and slight peak broadening, they still maintain some of the SERS profile of the HSA:AgNS bioconjugates. This comparison underscores the critical importance of considering the sample state (wet or dry) in SERS measurements, as it significantly impacts the quality, consistency, and interpretability of the spectra. Additionally, this finding suggests that for a PoCT application, the sample does not need to dry, as a wet sample is sufficient to produce a good SERS spectrum, saving time for the fast diagnostic.

3.4.1.3 Whatman No.1 paper substrate

Figure 38A, presents wet sample spectra of samples deposited on Whatman No. 1 paper substrate with printed wells, and significant variation in intensity is observed across different HSA:AgNS ratios. In Figure A11 at appendix A5, Raman spectra of just Whatman No.1 paper is presented. Among the tested ratios, the 100:1 ratio HSA:AgNS (dark red spectrum) shows the highest area peak, which suggests that the interaction between HSA and AgNS is stronger when the sample is wet. This leads to a more effective SERS effect. There are distinct peaks around 1100 cm^{-1}, 1300 cm^{-1}, and 1600 cm^{-1}, likely corresponding to the vibrational modes of the HSA protein as seen in section 3.2. Ratios like 1.0E3:1 and 2.6E2:1 HSA:AgNS (dark red and yellow spectrum) show more pronounced spectral features in the wet state, potentially due to better dispersion of HSA with the AgNSs in this condition. However, there is some background noise, especially above 1500 cm^{-1}, possibly due to the solvent or other aspects of the wet environment. Additionally, the observed shifts in the vibrational lines, such as at 925 cm^{-1} and 1015 cm^{-1}, may be attributed to potential thermal effects caused by laser burning into the sample. This heating can alter the molecular structure and interactions within the sample, leading to changes in vibrational frequencies.

In Figure 38B, which displays the dry sample spectra on Whatman No. 1 paper, the intensity becomes more consistent across different ratios, although the 1000:1 ratio (dark red spectrum) still exhibits the highest signal. However, no SERS lines are observed, likely due to the drying of the sample, which affects the scattering signal. These changes may impact the uniformity of the bioconjugate distribution on the substrate, consequently reducing the effectiveness of the SERS signal.

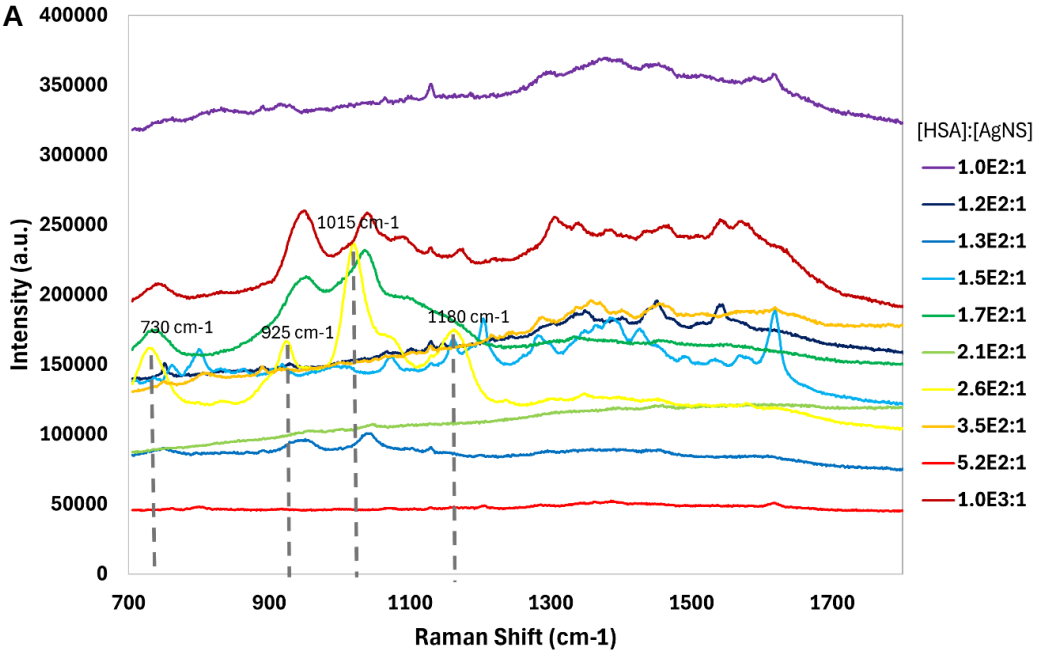

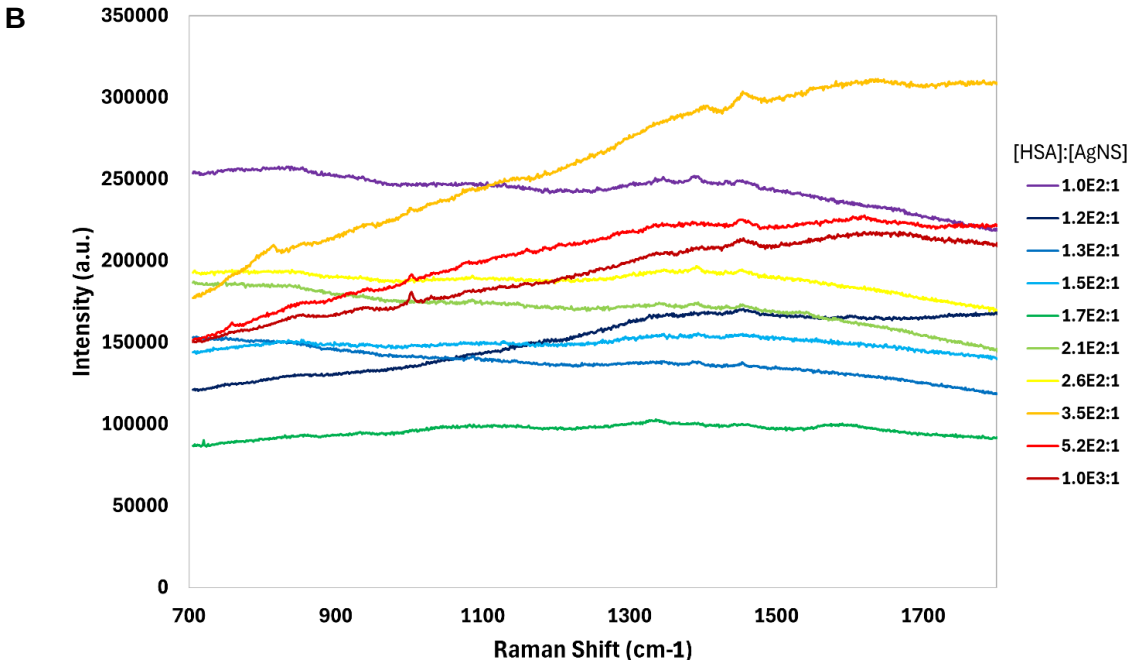

Figure 38. A. SERS spectra of HSA:AgNS conjugates (wet state) on Whatman No. 1 paper substrate read after adding the last drop. **B**. SERS Spectra of HSA:AgNS conjugates on Whatman No.1 paper substrate(dry state).

In general, for samples deposited on Whatman No.1 filter paper, the wet samples show higher intensity and narrow bands and measurable peaks areas, indicating stronger SERS signals. Conversely, drying appears to negatively impact the signal, as no SERS lines are observed. As a result, the wet state may be more favorable for achieving higher signal intensities, like what is observed with the photocopy paper substrate. Both substrates show comparable intensities, with photocopy paper at 400,000 a.u. and Whatman No. 1 paper at 250,000 a.u. However, photocopy paper consistently produces a uniform SERS spectral profile across most of the ten ratios, unlike Whatman No. 1 paper. Therefore, between these paper substrates, photocopy paper is likely to yield better results in future PoC tests.

3.4.1.4 Paper substrate with wells containing AgNP

In alignment with ongoing research at CENIMAT, we also explored the use of paper substrates with wells containing AgNP for SERS analysis. In this study, photocopy paper substrates were engineered with wells impregnated with AgNPs to enhance the sensitivity of biomolecule detection, specifically for HSA. In appendix A5, a SERS spectrum of these substrates can be observed, with no Raman lines being observed.

For this section five HSA:AgNS ratios that showed the best SERS signals in the previous section (3.4.1) were employed. This section evaluates the SERS spectral properties of HSA:AgNS deposited on these well-structured paper substrates in both wet

and dried states, assessing the effectiveness and suitability of the substrate for SERS-based analytical applications.

3.4.1.4.1 Deposition of HSA:AgNS bioconjugates

Figure 39A illustrates the SERS signal intensities for various HSA:AgNS ratios. Notably, significant vibrational modes of HSA are observed in this spectrum, particularly around 730 cm^{-1}, 925 cm^{-1}, 1015 cm^{-1}, and 1180 cm^{-1}, as seen in section 4.2. Additionally, vibrational lines at 1075 cm^{-1} and 1580 cm^{-1} may indicate possible signal overlap between AgNP from the wells and AgNS from the bioconjugates. This signal redistribution could modify the interaction dynamics between the AgNS and HSA, potentially leading to alterations in the SERS signal profile.

Figure 39B shows SERS spectra of HSA:AgNS conjugates in the dried state. Several distinct peaks are labeled at specific wavenumbers: 730 cm^{-1}, 925 cm^{-1}, 1015 cm^{-1}, and 1180 cm^{-1}, likely corresponding to characteristic vibrations of specific molecular bonds in HSA. However, these peaks exhibit a broader profile compared to those observed in the 'wet' state. Additionally, both the SERS intensity and peak area are lower than those recorded on the photocopy paper with printed wells (section 3.4.1.2), confirming that the latter remains the superior option.

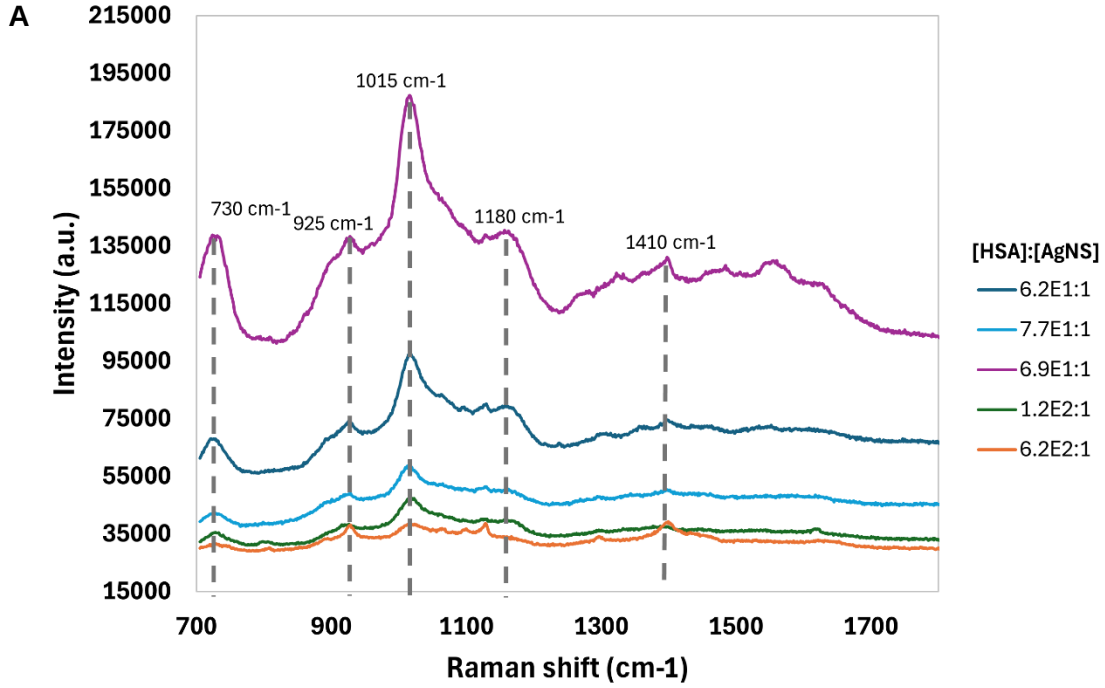

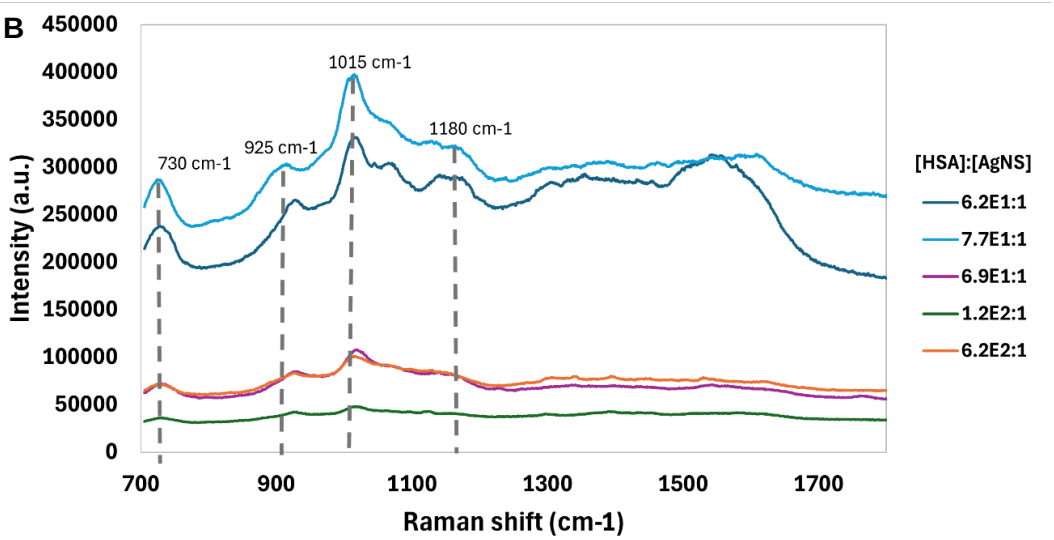

Figure 39. A. SERS spectra of HSA:AgNS conjugates in photocopy paper substrate containing AgNP on the wells read after adding the last drop. **B**. SERS Spectra of HSA:AgNS conjugates in photocopy paper substrate containing AgNP on the wells after the last drop added dried.

Here, is also possible to calculate the EF, by calculating the areas of the 1015 cm^{-1} when we deposit the HSA:AgNS conjugates on photocopy paper and photocopy paper with AgNP wells, in the wet state.

3.4.1.4.2 Deposition of protein HSA

This section focuses on evaluating the SERS spectra of just HSA when deposited on paper substrates impregnated with AgNPs, avoiding the step of conjugation with AgNS. The aim is to understand if there is a difference in Raman signals for a deposition of HSA or the deposition of the bioconjugates. By examining the SERS response at various HSA concentrations, both in wet and dry conditions, the study provides insights into the efficiency and practicality of AgNP-based substrates for potential biosensing applications. The two figures (Figure 40A-B) presented illustrate the SERS spectra for different concentrations of HSA deposited on paper substrates with AgNP wells.

In the first figure (Figure 40A), which depicts wet samples, the spectra show varying intensities across different concentrations of HSA. The spectra reveal clear vibrational bands characteristic of HSA, with prominent peaks around 1015 cm^{-1} and 1580 cm^{-1}, corresponding to specific molecular vibrations of this protein.

In contrast, the second figure (Figure 40B) represents the SERS spectra after drying the samples on the photocopy paper substrate with AgNP wells. Here, the intensity of the peaks is generally lower compared to the wet state. This reduction suggests that drying affects the SERS profile, likely due to changes in the distribution and interaction of HSA molecules with the AgNP substrate. Although the spectra retain the characteristic HSA vibrational bands (730 cm^{-1}, 927 cm^{-1}, and 1022 cm^{-1}), the SERS

profile appears altered, exhibiting higher background noise than those observed in section 3.2.

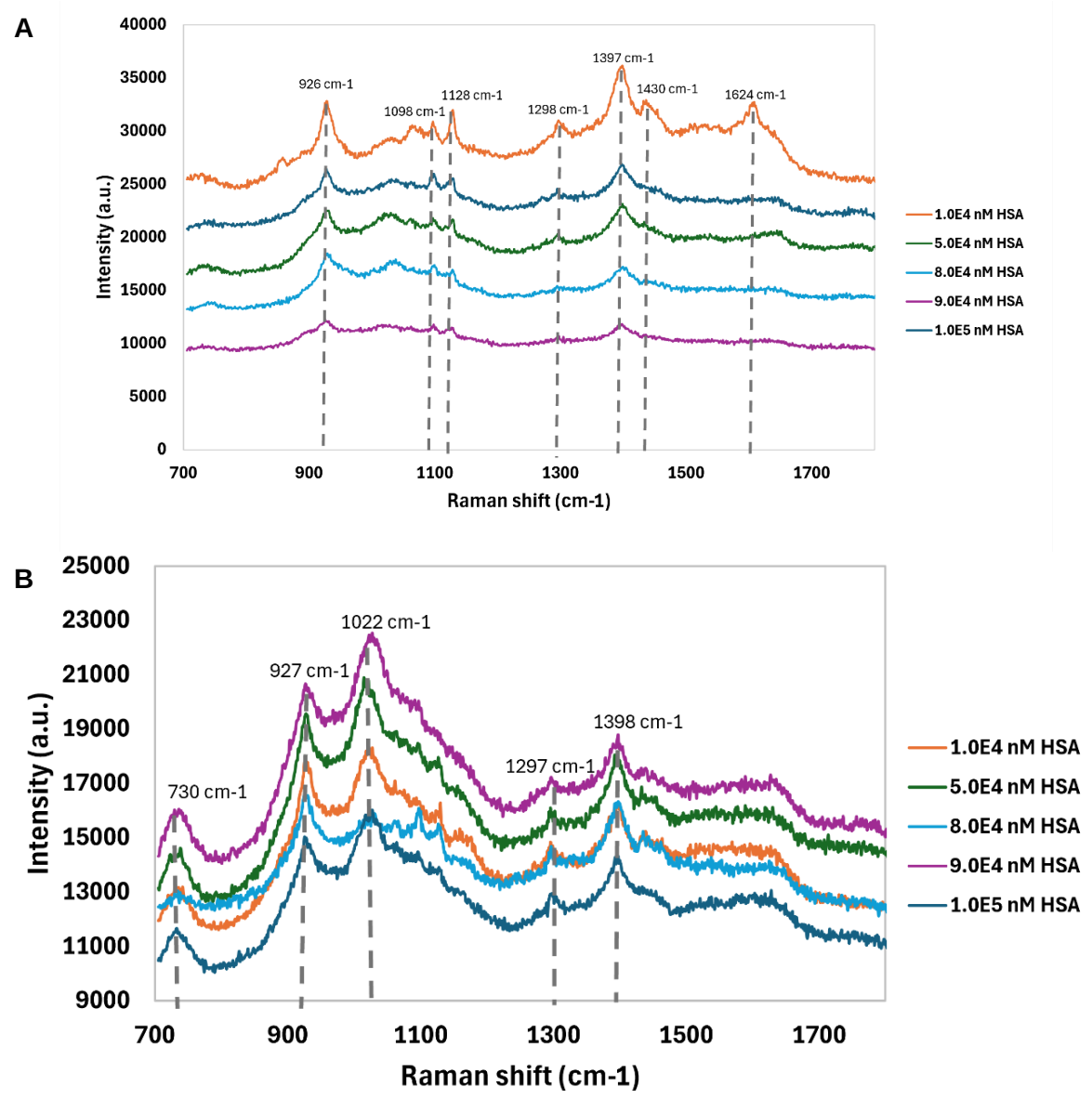

Figure 40. **A.** SERS spectra of HSA deposition in photocopy paper substrate containing AgNP on the wells read right after adding the last drop. **B**. SERS Spectra of HSA in photocopy paper substrate containing AgNP on the wells after the last drop added dried.

Overall, these figures demonstrate how the state of the sample (wet and dry) significantly influence the SERS signal. Notably, when only HSA is deposited, the Raman shift at 1180 cm^{-1} is absent in both states, which corresponds to a vibrational line previously associated with HSA. This experiment showed that the dried spectra provide a profile similar to the one obtained in the aluminium foil substrate, but not as well-defined as in the aluminium substrate.

3.4.1.5 Whatman No. 1 paper with wells with AgNS

In this section, inspired by the observations from previous sections, we aimed to determine whether pre-conjugation of HSA with AgNS was necessary before deposition on the substrate, or if the AgNS could be directly deposited on the paper substrate, allowing the sample to simply be added over the wells. The first figure (Figure 41A) depicts the SERS spectra obtained from a wet drop on Whatman No. 1 paper with AgNS already deposited (5 drops of 2 μL each, with drying intervals between applications). The spectra show a prominent signal with significant intensity, especially at higher concentrations of HSA. As the concentration of HSA increases, the intensity of the SERS signal also increases, particularly between 1200 cm^{-1} and 1500 cm^{-1}, that may indicate characteristic vibrational modes associated the paper substrate. In the wet condition (Figure 41A), the interaction between HSA molecules and AgNS appears to be more effective, resulting in a stronger SERS signal. However, the SERS spectra profile observed seems to be of the wax used to form the wells on the substrate.

In contrast, Figure 41B presents the SERS spectra after the drop has dried. The SERS signals here are notably weaker compared to the wet condition, with a lower signal-to-noise ratio. In both situations (wet and dry state), the SERS spectra resemble the one of the wax used for the wells, as it can be compared to the Raman spectra of wax in Figure 41C.

The third figure (Figure 41C) presents the Raman spectrum of the wax profile. Characteristic peaks between 1200 cm^{-1} and 1400 cm^{-1} are evident, and these peaks also appear in the earlier figures (Figure 41A-B), particularly under wet and dry conditions. This indicates that the wax from the wells of the paper substrate contributes to the overall SERS signal. Consequently, it suggests that refining the protocols for fabricating these substrates with wells is necessary to optimize signal clarity and reduce interference from the substrate material.

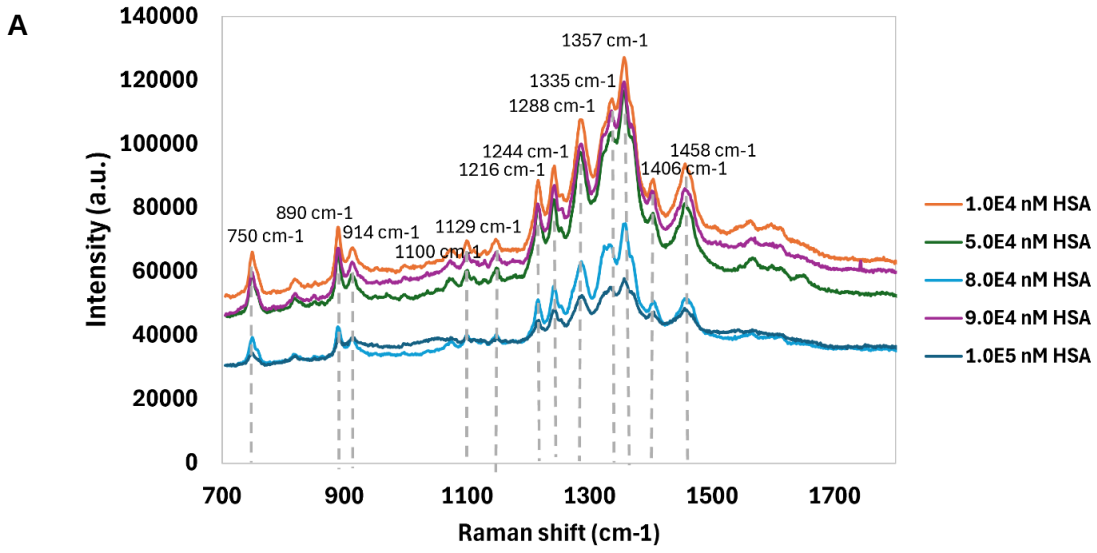

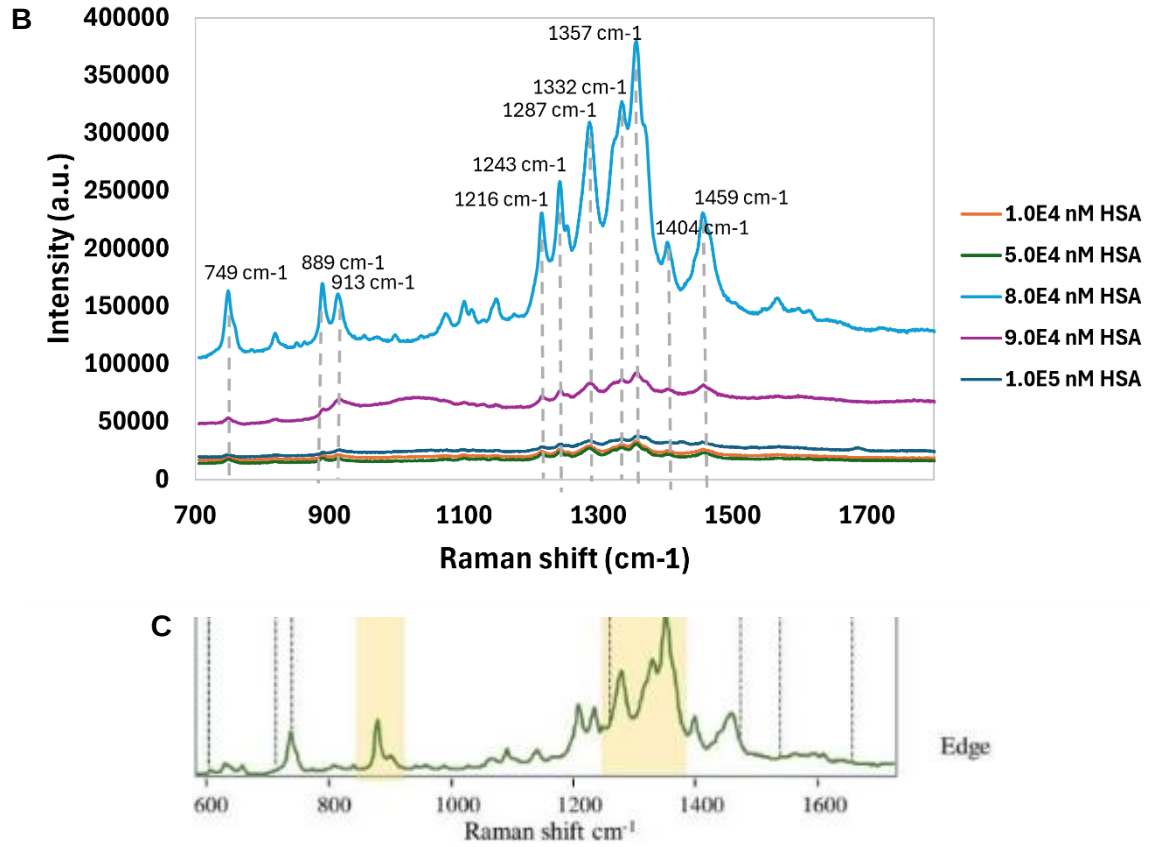

Figure 41. **A**. SERS spectra of HSA deposition on Whatman paper substrate containing AgNS on the wells read after adding the last drop. **B**. SERS Spectra of HSA on Whatman paper substrate containing AgNS on the wells after the last drop added dried. **C**. Raman spectra of wax used to limit the wells in Whatman paper substrate. Adapted from [125].

In conclusion, while the comparison between the wet and dry conditions revealed similar SERS spectra profile, the wet state consistently showed more reliable profiles, following a uniform pattern across different concentrations. To improve the consistency of the results, it is essential to repeat the experiment with careful control over the preparation process of this substrates, particularly to prevent wax diffusion into the paper substrate during the formation of the wells. This will help ensure that the substrate does not interfere with the SERS measurements.

3.4.1.6 Photocopy paper with wells with AgNS

This section focuses on the SERS analysis performed using photocopy paper substrates with wells containing AgNS, as this paper substrate was the one showing the SERS profile more similar to the ones obtained on the aluminium foil substrate (section 3.2). Figure 42A-B presented illustrates the SERS spectra of HSA at different concentrations, particularly after the last drop application and after the samples have dried on the paper substrate, respectively. The SERS spectra correspond to a range of HSA concentrations from 10000 nM to 100000 nM.

Figure 42A reveals a variation in SERS signal intensity as HSA concentration increases. Distinct peaks, particularly around 1100 cm^{-1} and 1500 cm^{-1}, suggest that this concentration facilitates optimal adsorption and interaction of HSA molecules with the AgNS on the paper substrate, resulting in strong signal intensities.

As observed in previous experiments, the photocopy paper substrate yielded better results: higher intensities, larger Raman shift areas, and a narrow bands. However, in this case, when AgNS were pre-deposited in the wells, dried, and then HSA was added, no distinct SERS spectra or peaks were observed, and the SERS intensities were significantly reduced. This may indicate that the drying process interferes with effective bioconjugate formation, diminishing the SERS effect.

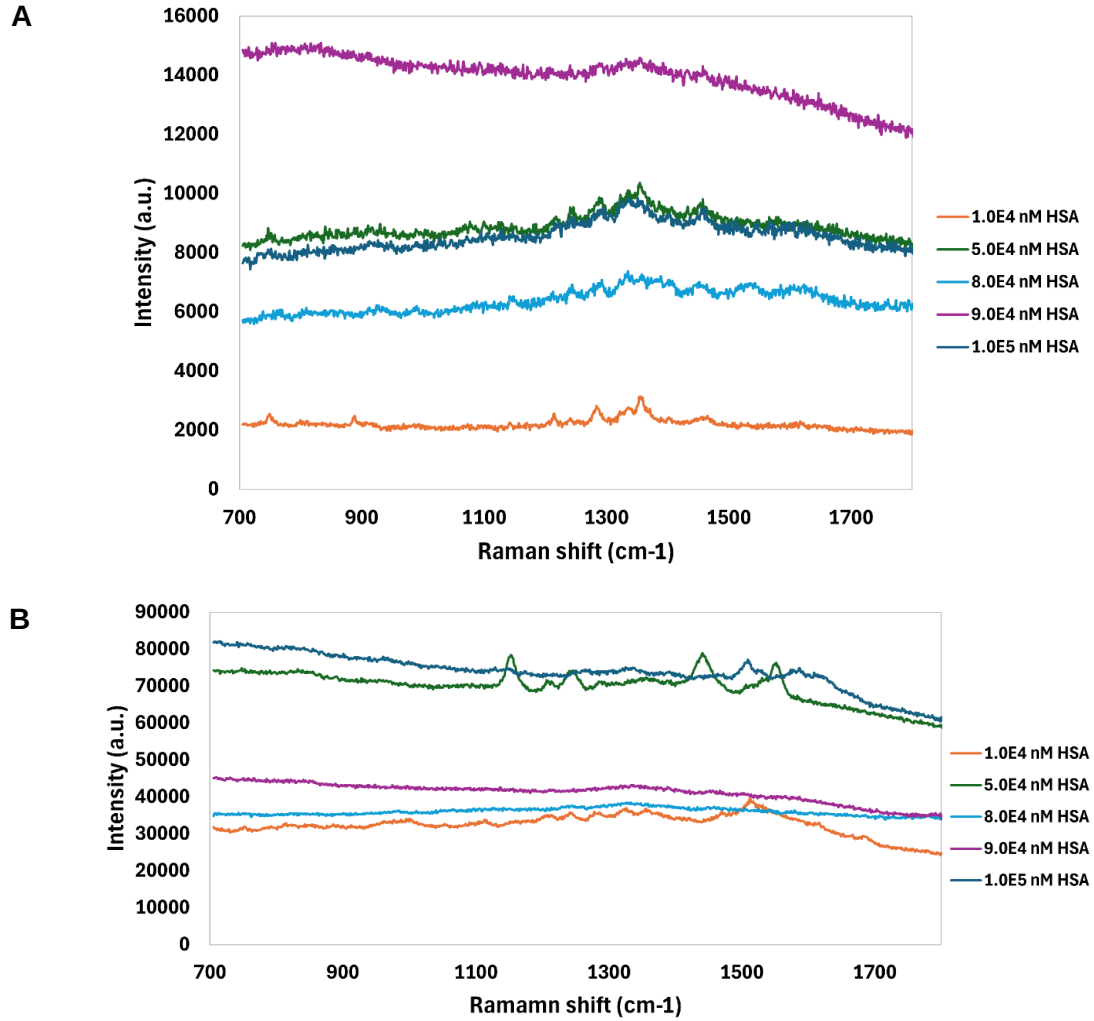

Figure 42. **A**. SERS spectra of HSA deposition on photocopy paper substrate containing AgNS on the wells read after adding the last drop. **B**. SERS spectra of HSA on photocopy paper substrate containing AgNS on the wells after the last drop added dried.

3.4.1.7 Photocopy paper with 100 nm of Molybdenum

In this section, we explored alternatives to the aluminium foil substrate, leading us to the idea of using a paper substrate coated with a layer of molybdenum (Mo). The

choice of molybdenum (Mo) was based on its similar refractive index to aluminium, making it a suitable substitute. Figure 43 shows SERS spectra for different series using a photocopy paper substrate coated with 100 nm of molybdenum (Mo) (Figure A13 in appendix A5). The three series likely represent varying conditions, such as different HSA concentrations or other experimental variables. Not all concentration were tested as the other wells of the photocopy paper presented the presence of the wax in their SERS spectra. The most prominent peaks are observed in green (1.5E2:1 HSA:AgNS) and blue (3.5E2:1 HSA:AgNS) spectrum, indicating stronger SERS signals under these conditions. Significant peaks around 800 cm^{-1} and 1600 cm^{-1} suggest the presence of specific molecular vibrations that are strongly enhanced by the Mo-coated surface.

The orange spectrum (5.2E2:1 HSA:AgNS) shows much lower intensity across the board, which could imply that this particular condition, potentially a lower concentration of HSA or a less effective interaction with the Mo surface, results in weaker SERS enhancement. This disparity in intensity between the series underscores the importance of the experimental setup, particularly the surface placement and the interaction between the sample and the substrate.

The use of 100 nm Mo on photocopy paper as a SERS substrate produces low background noise and narrow bands, indicating that this surface modification is effective in enhancing SERS signals. However, the varying intensities across the different series suggest that optimizing experimental parameters is crucial to achieve consistent and strong SERS signals. Additionally, compared to the other substrates studied, this one provides lower SERS intensity, with photocopy paper and aluminium foil substrates still being the best options.

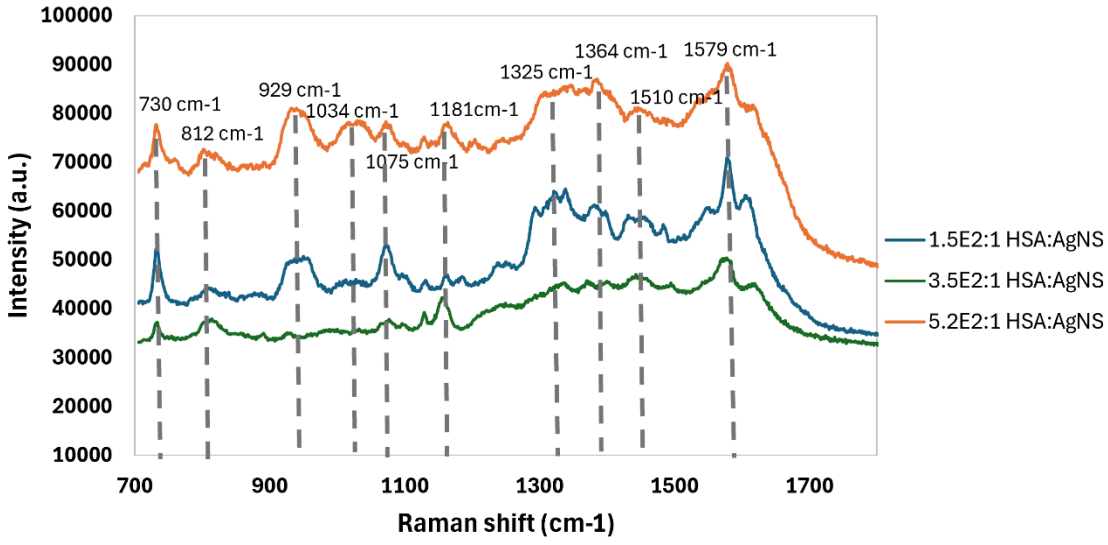

Figure 43. SERS spectra of HSA:AgNS deposition on photocopy paper substrate with 100nm Mo deposited on the substrate.

Based on these results, the most suitable substrates for PoCT and SERS analysis are aluminum and photocopy paper with printed wells. The latter showed increased

intensity, likely due to the concentration effect of the printed wells. Other experiments, involving the deposition of just the protein (HSA) or wells with AgNP and Mo, did not produce sufficient intensity or the spectral profile observed in section 3.2. Additionally, keeping the sample wet enhances Raman intensity, which can save time in PoCT applications by eliminating the need to wait for the drop to dry. Moreover, the bioconjugation process is confirmed by DLS analysis (see Appendix A6), further validating the interaction between HSA and AgNS in these conditions.

3.5 Characterization of 10 Selected Plasma:AgNS Ratios from Initial Screening

This section describes plasma protein bioconjugates with ten different ratios plasma:AgNS (from 97:1 to 9700:1). The interaction between AgNS and plasma proteins holds great potential for applications in biomedical sensing, diagnostics, and therapeutic delivery. The aim of this study is to identify the optimal conditions that produce the most stable and effective bioconjugates for these various applications by generating bioconjugates with different ratios of AgNS to plasma proteins. This approach allows us to explore how these variations affect key physical characteristics of the bioconjugates, such as hydrodynamic size, stability, and aggregation behavior (see appendix A7 for DLS characterization). Each ratio represents a specific concentration of plasma proteins relative to the silver nanostructures.

The findings presented here are part of a broader effort to understand the behavior of these bioconjugates, with potential implications for their use in analytical techniques such as SERS. This analyzis underscores the importance of optimizing the plasma:AgNS ratios to maximize the SERS signal and improve the sensitivity and specificity of PoC diagnostic applications.

The complexity of the protein mixture in plasma necessitates further statistical analyzis for accurate spectral interpretation. These features are critical in defining the performance of the bioconjugates in applications like SERS, where the interaction between the protein and the nanostructure directly impacts signal intensity, reproducibility, and overall sensitivity. The objective of the subsequent analysis is to determine the optimal plasma:AgNS ratio for producing stable and efficient bioconjugates, with a particular emphasis on their potential use in SERS-based sensing technologies.

3.5.1 SERS Analysis

3.5.1.1 Aluminium foil

This section focuses on the SERS analysis of plasma using aluminium foil as a substrate. Figure 44 displays the SERS spectra obtained at various plasma:AgNS ratios, providing important insights into how these ratios affect the intensity of the SERS

signals. The measurement parameters included a 20x objective, a laser power of 50 mW, and 3 scans with an exposure time of 5 seconds each. Five spectra were obtained for each sample.

The most notable finding from the figure is that the highest SERS intensity is achieved at a plasma:AgNS ratio of 75:1, represented by the blue spectrum. This spectrum shows significant high-intensity peaks, particularly in the plasma-specific regions around 800 cm^{-1}, 1100 cm^{-1} and 1600 cm^{-1}. These sharply defined peaks indicate a strong interaction between the AgNSs and plasma molecules, resulting in a substantial enhancement of the Raman signal.

Figure 44 also reveals that the SERS signals remain relatively strong at certain intermediate ratios, such as 1800:1 and 1200:1 plasma:AgNS. This suggests that there is a threshold concentration of plasma required for effective SERS enhancement. However, as the concentration decreases further, the SERS effect significantly diminishes, as observed in the spectra with the lowest ratios.

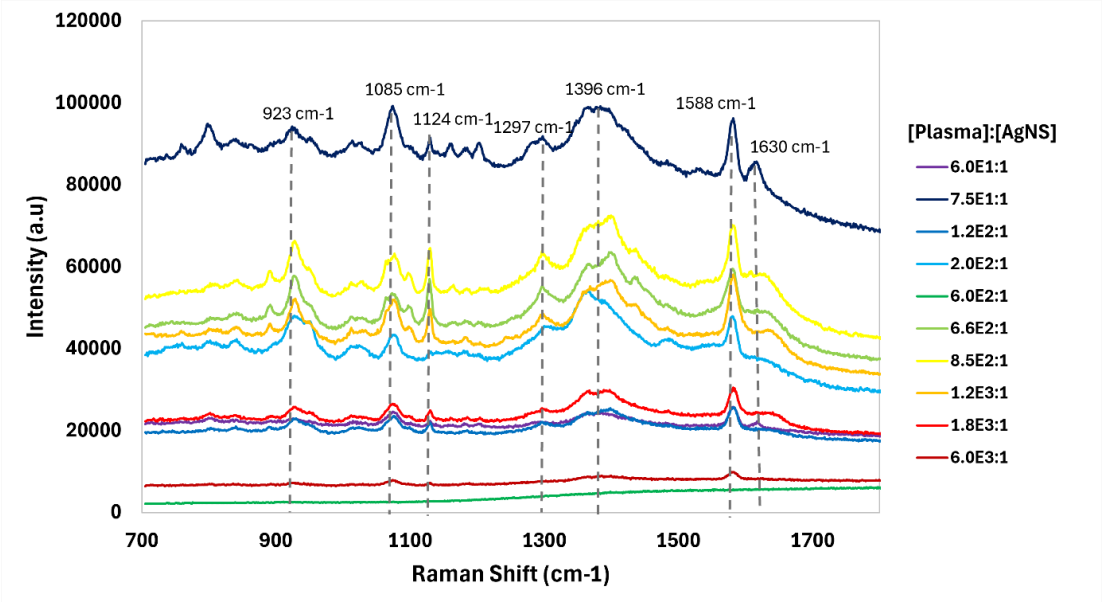

Figure 44. SERS Spectra of the 10 different ratios Plasma:AgNS on aluminium foil.

The data suggest that a higher concentration of plasma relative to AgNSs is necessary to obtain robust and reproducible SERS signals. This finding is critical for applications that rely on SERS for the detection of plasma or other biomolecules, as it underscores the need for meticulous optimization of sample preparation parameters to ensure accurate and sensitive detection.

3.5.1.2 Photocopy paper substrate

Figure 45 presents the SERS spectra for plasma samples evaluated across ten different plasma:AgNS ratios on a photocopy paper substrate with wells. The first image shows the spectra while the drop is still wet (Figure 45A), and the second image displays the spectra after the drop has dried (Figure 45B).

In the wet condition (Figure 45A), the SERS signals are generally weaker, with the strongest spectrum reaching an intensity of about 200000 a.u. This lower signal strength may be due to the uneven distribution of analytes on the wet surface or the scattering effects of water molecules, which could hinder effective interaction with the SERS-active sites of the substrate. The spectral features in this state are broader, and the peaks, particularly those between 1300 cm^{-1} and 1500 cm^{-1}, appear less defined, suggesting a less stable environment for the analyte molecules.

Once the drop dries (Figure 45B), the SERS signals intensify significantly, with the highest intensity spectrum reaching up to 350000 a.u. During the drying process, analytes are likely concentrated on the substrate, enhancing their interactions with the silver nanoparticles. This results in sharper peaks, especially in the 1300–1600 cm^{-1} range, indicating that the drying procedure improves the sensitivity and stability of the SERS measurement. The increased sharpness and intensity of the peaks reflect stronger interactions between the analyte molecules and the SERS-active sites on the substrate.

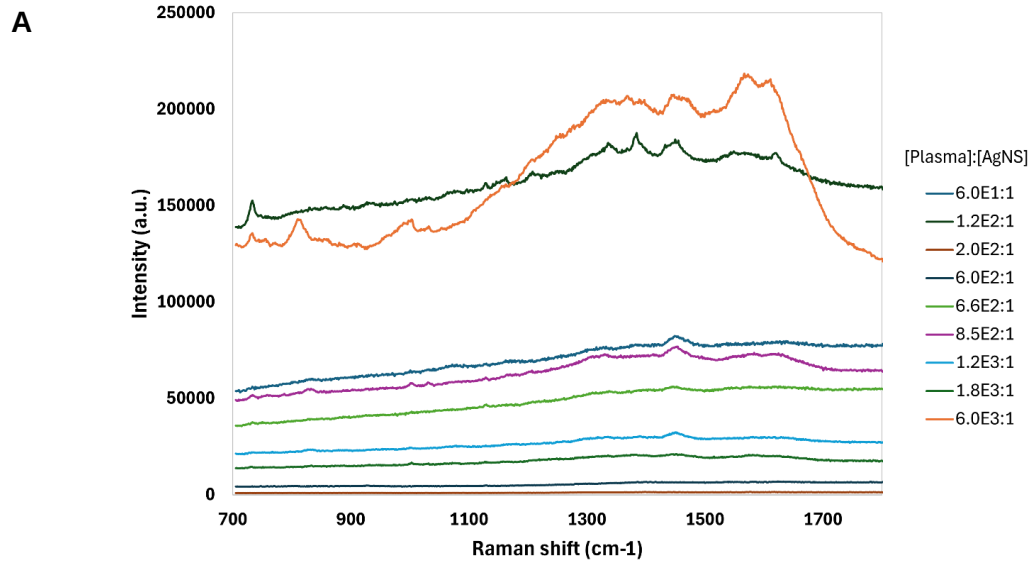

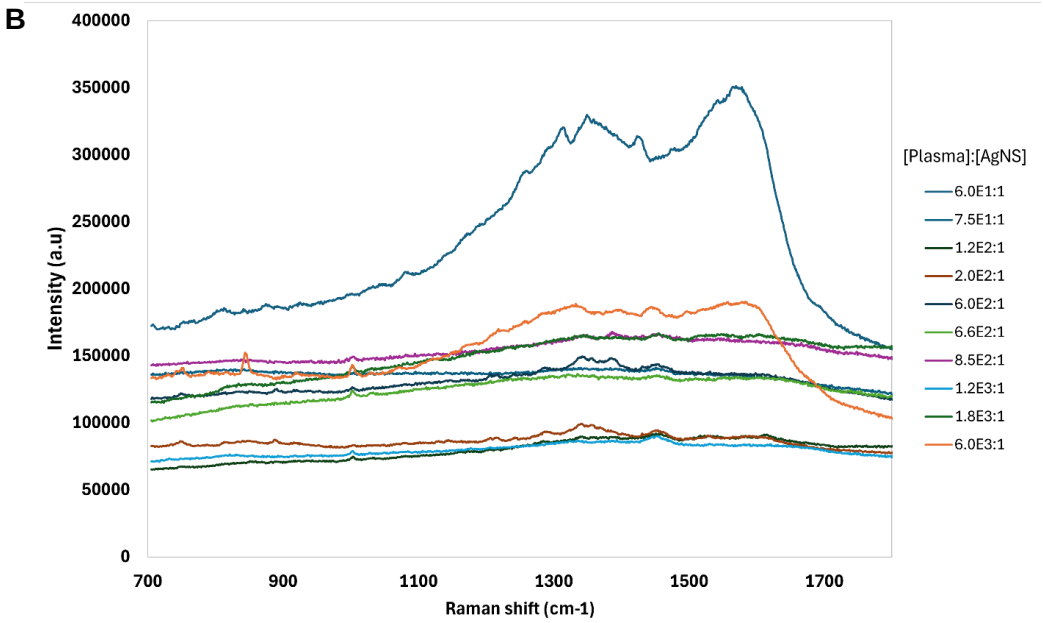

Figure 45. **A**. SERS spectra of plasma:AgNS conjugates on photocopy paper in the wet sate. **B**. SERS spectra of plasma:AgNS conjugates on photocopy paper in the dry state.

Overall, the SERS spectra obtained in the dry condition show significantly higher intensities compared to those in the wet condition, indicating that the drying process enhances signal sensitivity. However, the SERS spectral profiles between the two states remain largely similar, with key peaks appearing at comparable positions and relative intensities. This suggests that while drying boosts the overall signal strength, it does not significantly alter the fundamental spectral features of the analytes. Additionally, when comparing these results to those in section 3.3 using the aluminum substrate, the SERS spectra exhibit broader peaks and less measurable peak areas, indicating reduced resolution and signal clarity on the photocopy paper with printed wells substrate.

3.5.1.3 Whatman No. 1 Paper substrate

The first figure (Figure 46A) presents the SERS spectra obtained from a wet sample drop applied to the Whatman No. 1 paper substrate with wells. The spectra exhibit multiple peaks with noticeable intensity variations across different SERS lines. A characteristic wax signal from the Whatman No. 1 paper is evident between 1100 and 1500 cm^{-1}, contributing to a complex background. Different analyte concentrations are represented by various colors in the spectra; for instance, higher concentrations (shown in blue and green) display more intense and narrower peaks compared to lower concentrations.

In contrast, Figure 46B shows the SERS spectra recorded after the sample had dried on the same substrate. The dried sample spectra demonstrate significantly higher intensities, indicating more effective SERS enhancement compared to the wet condition. The peaks are more pronounced, particularly in regions corresponding to

key molecular vibrations of the analytes. Despite the drying process, the wax signal between 1100 and 1500 cm^{-1} remains present (as shown in Figure 46C).

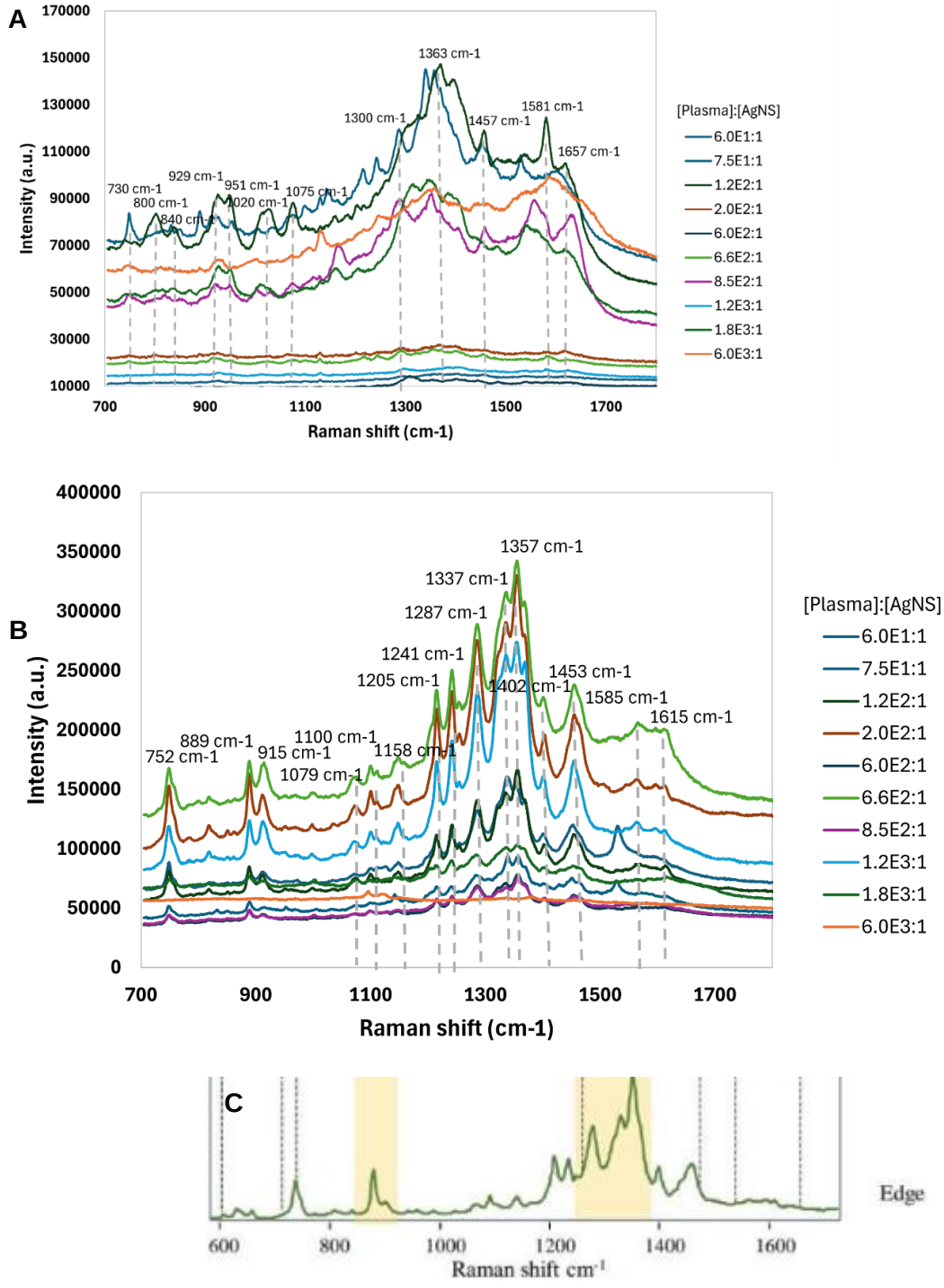

Figure 46. **A**. SERS spectra of plasma:AgNS conjugates in Whatman paper after adding the last drop. **B**. SERS spectra of plasma:AgNS conjugates in Whatman paper after the last drop was added and

dried. **C**. Raman spectra of wax used to limit the wells in Whatman paper substrate. Adapted from [125].

3.5.2 Plasma without albumin

After the optimizations discussed in previous sections, this section focuses on the SERS and DLS analysis of AgNS bioconjugates with plasma samples from which albumin has been removed (Psem). The goal is to investigate whether albumin, the most abundant plasma protein, might be masking the detection of other plasma proteins. Albumin's high concentration can dominate the analysis, potentially leading to an underestimation of the size distribution and polydispersity of the remaining proteins. By removing albumin, we aim to gain a clearer understanding of the behavior and characteristics of the other plasma proteins, ensuring more accurate detection and analysis of their interactions with AgNS bioconjugates.

3.5.2.1 SERS Analysis

The Raman shift profiles for various samples from the plasma without albumin on aluminium foil experiment are illustrated by the SERS analysis shown in Figure 47A. The measurement parameters included a 20x objective, a laser power of 50 mW, and 3 scans with an exposure time of 5 seconds each. Five spectra were obtained for each sample. Raman spectrum of plasma without albumin is in appendix A7, and no Raman vibrations can be observed. In appendix A9, a control of SERS spectra of plasma without albumin with no vibrational lines can be observed.

The blue spectrum (3300:1 Psem:AgNS), presents sharp and intense bands, namely in the 1200 cm^{-1} to 1600 cm^{-1} range. This suggests that specific proteins or aggregates become more pronounced and contribute to stronger Raman signals when albumin is absent. This is possible to observe in Figure 47B, were SERS spectra of Psem:AgNS and plasma:AgNS are being compared. Conversely, samples with higher albumin concentrations or lower concentrations of other proteins, such as 2000:1 and 100:1 Psem:AgNS, display lower intensity SERS spectra, reflecting less aggregation or fewer scattering centers. As observed in section 3.2 when working with HSA, the characteristic SERS profile is no longer present, as the vibrational lines that correspond to 928 cm^{-1}, 1015 cm^{-1} and 1180 cm^{-1}.

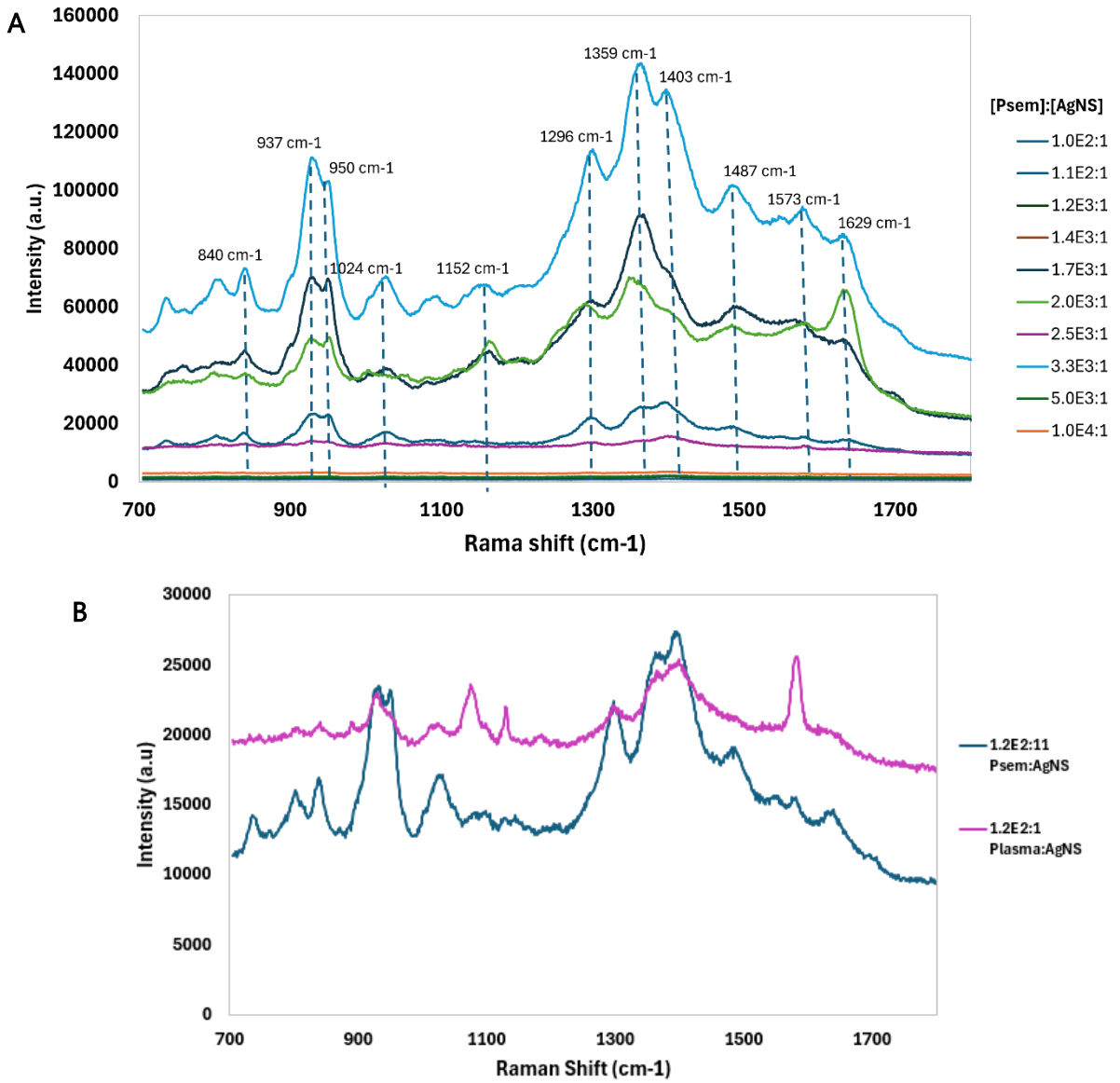

Figure 47. **A.** SERS spectra of plasma without albumin (Psem) conjugated with AgNS in ten different ratios on aluminium foil. **B.** SERS Spectra comparing SERS spectra of Psem:AgNS and plasma:AgNS bioconjugates on aluminium foil.

Furthermore, the SERS spectra reveal a distinct profile compared to previous sections, with the appearance of new vibrational lines at 950 cm^{-1}, 1296 cm^{-1}, 1359 cm^{-1}, 1433 cm^{-1}, and 1487 cm^{-1}. Additionally, some vibrational lines that had already appeared in section 4.3, such as 937 cm^{-1} and 1024 cm^{-1}, were also detected, indicating that certain protein interactions are consistent across different plasma conditions.

3.5.2.2 DLS Analysis

The Z-average values (Figure 48), representing the intensity-weighted mean hydrodynamic diameter, show a clear trend of increasing particle size as the concentration of albumin decreases across the samples. In the sample with the highest albumin concentration (1000:1 Psem:AgNS), the Z-average is the smallest at 108 nm, suggesting

that albumin helps maintain smaller and more uniform particles. As the albumin concentration decreases, the Z-average gradually increases, with 1.0E4:1 Psem:AgNS and 1.0E5:1 Psem:AgNS showing average sizes of 140 nm and 131 nm, respectively. This upward trend continues, reaching 156 nm in 1.0E6:1 Psem:AgNS, and culminates in a significant spike to 314 nm in 1.0E7:1 Psem:AgNS, where albumin is completely absent. This pattern suggests that albumin plays a critical role in preventing the aggregation of plasma proteins, thereby maintaining a more stable and smaller particle size distribution.

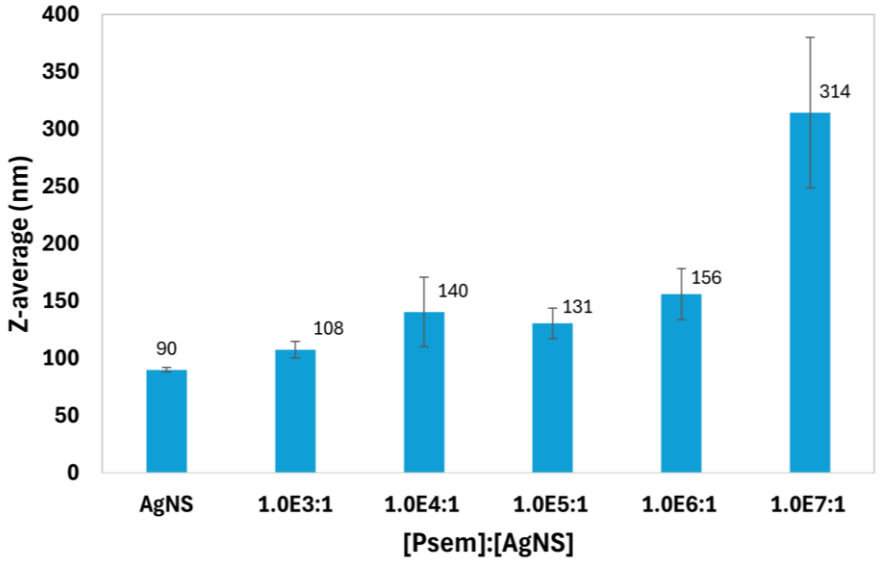

Figure 48. Z-average (in nm) of plasma without albumin bioconjugates with AgNS at different ratios ranging from 1000:1 to 1.0E7:1.

Table 6. Polydispersity index of plasma without albumin conjugated with AgNS ratios.

[Psem]:[AgNS]	Polydispersity index (PDI)					Average	SD
0 (AgNS alone)	0.108	0.257	0.372	0.294	0.053	0.22	0.12
1000:1	0.095	0.12	0.208	0.103	0.114	0.13	0.04
1.0E4:1	0.019	0.275	0.234	0.174	0.02	0.14	0.11
1.0E5:1	0.168	0.122	0.272	0.266	0.1	0.19	0.07
1.0E6:1	0.281	0.117	0.124	0.269	0.257	0.21	0.07
1.0E7:1	0.056	0.142	0.305	0.129	0.269	0.18	0.09

The PDI values (Table 6) further supports these findings by highlighting the heterogeneity in particle size distribution across the samples. In the 1000:1 Psem:AgNS sample, the PDI values are relatively low, indicating a uniform particle size distribution consistent with the smaller Z-average. As the albumin concentration decreases, the PDI values increase, particularly in 1.0E5:1 Psem:AgNS and 1.0E6:1 Psem:AgNS,

where higher values suggest a broader range of particle sizes due to the onset of protein aggregation or protein corona formation. This trend becomes more pronounced in the 1.0E4:1 sample, where the PDI remains relatively high, reflecting ongoing aggregation. In the 1000:1 sample, the PDI shows even greater variability, which aligns with the significant increase in Z-average, indicating a much more heterogeneous particle size distribution in the absence of albumin. Additionally, when AgNS conjugated with plasma without albumin, a decrease in zeta potential is observed (Figure 49), indicating that the conjugation is happening.

The analysis reveals that albumin not only affects the detection of other proteins but also plays a crucial role in maintaining protein stability. The removal of albumin results in significant protein aggregation, as indicated by the increase in Z-average and greater variability in PDI. This highlights the critical role of albumin in preserving the structural integrity of plasma proteins and emphasizes the importance of accounting for its influence in plasma-based studies to ensure accurate data interpretation.

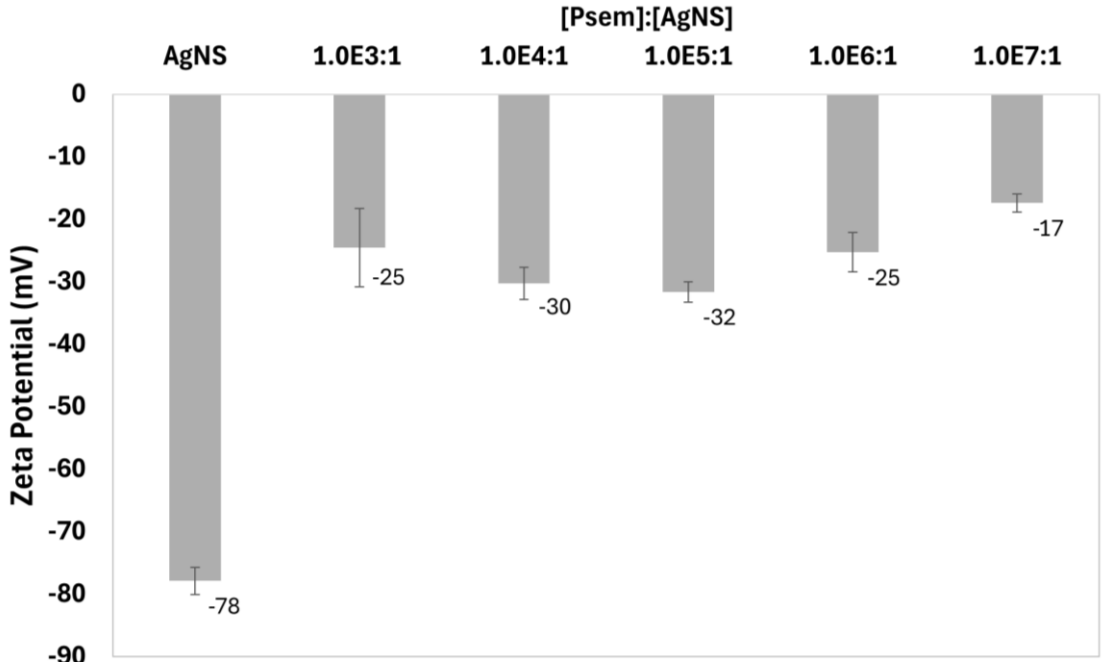

Figure 49. Zeta Potential (mV) of the ten Psem:AgNS ratios. In the y-axis is the zeta potential (mV) and in the x-axis is the different ratios of the bioconjugates of Psem:AgNS.

Moreover, the removal of albumin does not appear to impact the formation of the protein corona around the nanoparticles. In fact, the size of the particles increases when compared to the AgNS-only sample, suggesting that when albumin is removed, other proteins may be taking its place and forming a more extensive corona around the nanoparticles.

Additionally, the observed decrease in zeta potential further supports the notion that conjugation is occurring. A lower zeta potential typically indicates reduced surface charge repulsion, which is consistent with the formation of a protein corona that alters the surface characteristics of the nanoparticles.

The variation in peak intensities across the different SERS spectra likely reflects differences in protein interactions and aggregation behaviors in the absence of albumin. DLS analysis also showed larger hydrodynamic diameters, as measured by Z-average values in albumin-depleted samples, consistent with the higher peaks and greater intensities observed in some ratios indicating enhanced protein aggregation. These findings support the hypothesis that albumin stabilizes bioconjugates, preventing their aggregation. Combined with the DLS results, the data from this SERS analysis provide a comprehensive understanding of how albumin removal affects plasma protein behavior, underscoring the importance of considering these factors in analytical studies.

3.5.3 SDS-PAGE Analysis

To verify the removal of albumin from the plasma, an SDS-PAGE analysis was conducted. This experiment also provided a detailed observation of the overall plasma protein composition, allowing us to better understand the range of proteins present in the plasma after albumin extraction. Several conclusions can be drawn from the SDS-PAGE gel image (Figure 50) and the provided molecular weight data (Table 7). The standard low molecular weight markers correspond to this reference. [126] To determine the molecular weight of the various proteins, a calibration curve was generated using the low molecular weight markers (see Appendix A8, figure A19). The first lane, labeled "HSA," shows a distinct band around 65.7 kDa, aligning well with the expected molecular weight of human serum albumin. In the second lane, "HSA depleted from Plasma," a comparatively much less intense band at the same molecular weight suggests partial removal of albumin from the plasma, and additional bands around 56.2 kDa agree with the MW of fibrinogen beta.

The third lane, "Plasma without albumin," displays multiple bands corresponding to proteins such as transferrin at 93.9 kDa and haptoglobulin at approximately 73.4 kDa, as indicated by our data. The fourth lane, "Plasma without albumin 2," also shows bands for haptoglobulin and transferrin with slightly different molecular weights, indicating potential isoforms or variants of these proteins. The "Plasma" lane exhibits a complex profile with bands representing a mixture of proteins including immunoglobulins, transferrin, albumin, and fibrinogen, characteristic of normal plasma composition.

Overall, the gel and data indicate that albumin depletion from the plasma samples was generally successful, although some residual albumin remains in the depleted samples. The consistent presence of fibrinogen, haptoglobulin, and transferrin across several lanes highlights the complexity of the plasma protein mixture and demonstrates that the depletion process effectively reduces albumin levels while largely preserving other proteins. In appendix A6 it is possible to observe the calibration curve used for the determination of the MW in the bands present in the SDS-PAGE gel.

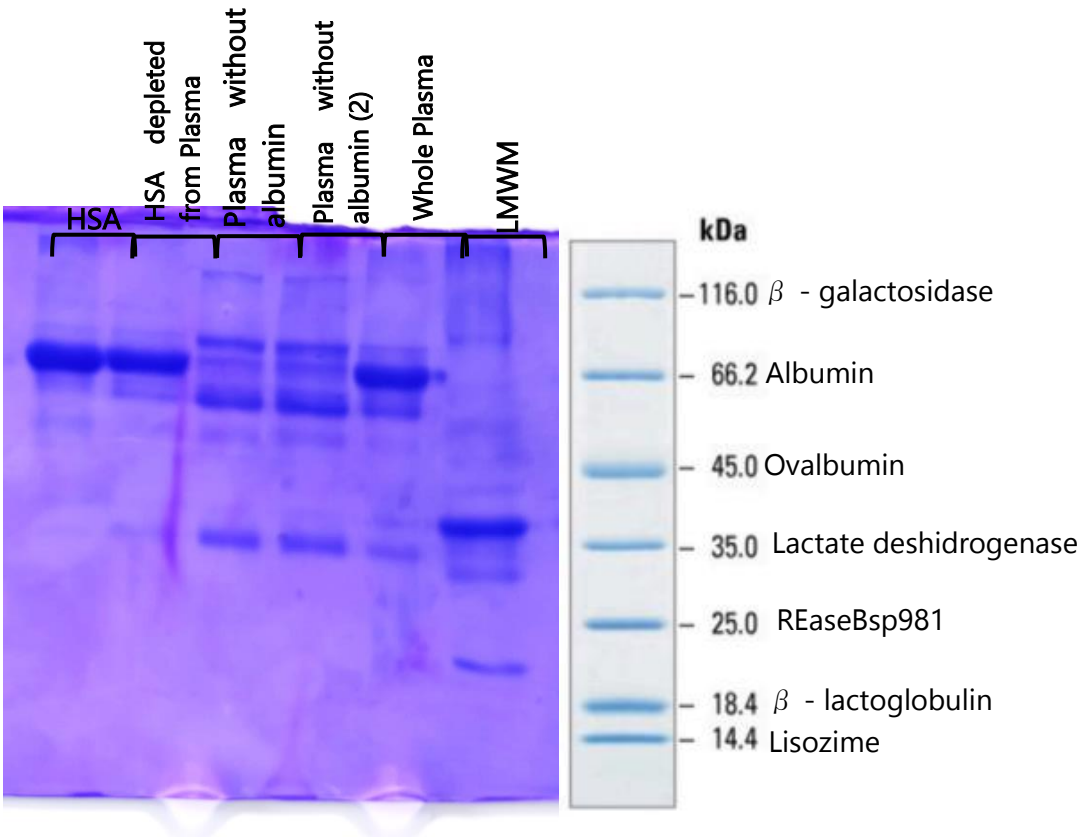

Figure 50. SDS-PAGE Analysis of Plasma Protein Profiles: Comparison of Albumin-Depleted Plasma and Whole Plasma Samples.

Table 7. Molecular Weights of the proteins that appeared in the SDS-PAGE.

Plasma	Molecular Weight (kDa)
Transferrin	73.4
Albumin	63.0
Fibrinogen	56.0
IgG,IgM	19.1

Plasma without albumin	Molecular Weight (kDa)
1- Transferrin	93.9
1- Haptoglobin	73.4
1- Fibrinogen gamma	55.5
2- Haptoglobin	96.2
2- Transferrin	71.0
2- Fibrinogen gamma	57.4

HSA	Molecular Weight (kDa)
Albumin depleted from Plasma	63.6
Albumin depleted from Plasma Fibrinogen beta	56.12
HSA	65.7
HSA- Fibrinogen beta	58.4

3.6 Statistical SERS analysis by PCA

Principal Component Analysis (PCA) is a statistical technique used to reduce the dimensionality of large datasets while preserving the most significant variance in the data. In this section, PCA was applied to analyze spectral data of bioconjugate samples containing HSA (A), plasma (P), and plasma without albumin (PS). The objective was to identify patterns, similarities, and differences between the samples based on their spectral profiles.

The PCA score plot is shown in Figure 51, with each point representing one of the 50 spectra for each sample type. The two principal components, PC-1 and PC-2, account for 71% of the total variance in the data, with PC-1 contributing 60% and PC-2 contributing 11%. The samples form three distinct clusters: plasma (P, red ellipses), HSA (A, blue ellipses), and plasma without albumin (PS, green ellipses).

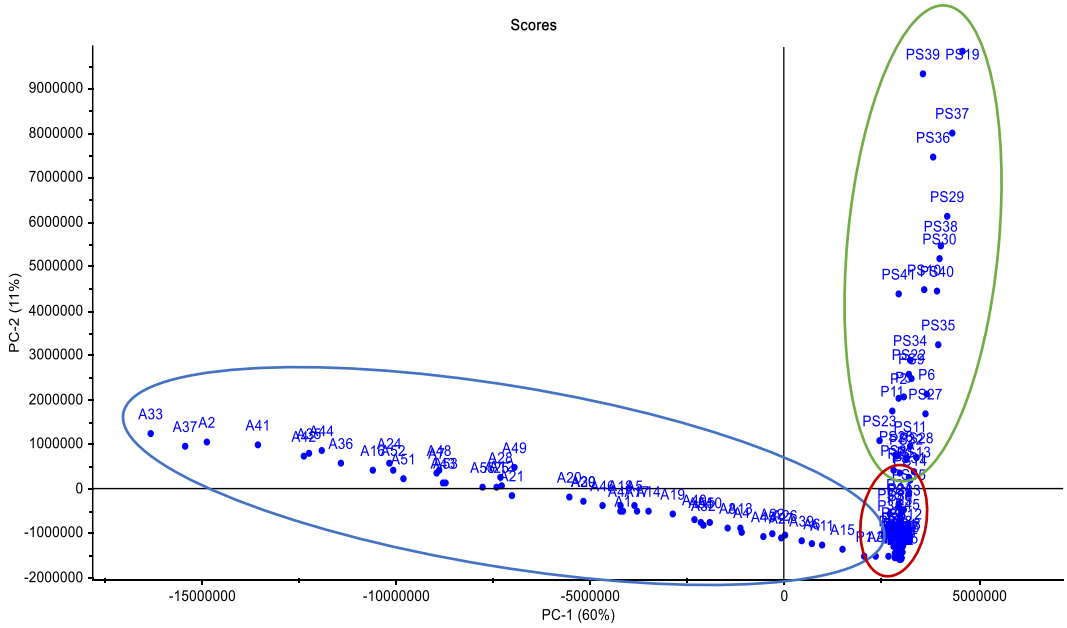

Figure 51. PCA of the different samples, albumin (A, blue ellipses), plasma (P, red ellipses) and plasma without albumin (PS, green ellipses).

The HSA (A) samples cluster on the left side of the PCA plot, showing a notable spread along the PC-1 axis, indicating variability likely due to concentration differences or minor impurities. This variability along the x-axis does not correlate with the different ratios used, as samples like A1, the least concentrated, and A33, a mid-range concentration, are both positioned further from the main cluster. This spread may be attributed to the varying intensities of spectra obtained from measuring different points within the samples. There is also moderate spread along the PC-2 axis, suggesting secondary variations that might be related to sample preparation or measurement conditions.

The plasma (P) samples are tightly clustered around the origin of the plot, showing minimal variation along both PC-1 and PC-2. This tight clustering suggests that the plasma samples have a uniform spectral profile, likely due to the consistent presence of various plasma proteins that produce a stable signal. The narrow spread indicates high reproducibility of the plasma samples under the given experimental conditions.

The plasma without albumin (PS) samples form a distinct cluster on the right side of the plot. These samples show significant separation from both the albumin and plasma samples, particularly along the PC-1 axis. This separation suggests that the removal of albumin substantially alters the plasma's spectral characteristics, likely due to the absence of the most abundant plasma protein. The variability within this group, indicated by the spread along the PC-2 axis, could be due to differences in the concentrations of remaining plasma proteins or interactions with other components after albumin removal.

Overall, the PCA analysis effectively differentiates between the three sample types based on their spectral profiles. The clear separation between clusters highlights the significant impact of albumin on the spectral properties of plasma. This analysis demonstrates that removing albumin from plasma significantly alters the sample's biochemical environment, as reflected in the SERS spectra, underscoring the importance of albumin in bioconjugate formation and its influence on spectral data interpretation.

Looking ahead, this approach establishes a foundation for future research involving stroke samples. By integrating PCA with machine learning techniques, we aim to enhance the ability to distinguish between various plasma bioconjugates, especially those associated with pathological conditions like stroke. Machine learning algorithms trained on large SERS datasets could identify subtle patterns and differences that may not be immediately apparent through conventional statistical methods. This advanced analysis will enable more precise identification of disease-specific biomarkers, aiding in the development of non-invasive diagnostic tools for stroke and potentially other conditions.

3.7 Testing incubation times in view of PoCT application

An important factor in the development of effective PoCT solutions is the optimization of incubation times of the sample conjugated with AgNS. PoCT devices are designed to provide rapid and accurate diagnostics at or near the patient care site, making the performance and reliability of these tests crucial. The incubation period, or the time the sample interacts with the AgNSs, can significantly impact the sensitivity and specificity of the diagnostic test. This section focuses on evaluating different incubation times to identify the optimal duration that balances rapid detection with accurate and reliable results. By experimenting with various incubation intervals, we aim to determine the ideal conditions for the bioconjugates, or other reagents used in

PoCT, in terms of signal strength, repeatability, impacting on the overall diagnostic accuracy.

3.7.1 SERS Analysis

Figure 52A displays SERS spectra of bioconjugates of AgNS with 990:1 HSA:AgNS HSA at different incubation durations (15 minutes, 3 hours, and overnight). This concentration is between the range that we determine in section 4.2.The measurement parameters included a 20x objective, a laser power of 50 mW, and 3 scans with an exposure time of 5 seconds each. Five spectra were obtained for each sample.

Significant variations in signal intensity are evident, with values ranging from 31000 a.u. at the 3-hour incubation to 12000 a.u. at the 15-minute mark. Notably, the overnight spectra demonstrate a substantial decrease in SERS intensity, dropping to just 4000 a.u.

Unlike other sections of the SERS analysis, in this experiment, the samples were not centrifuged after the incubation period, because of experimental constraints. This lack of centrifugation leads to more HSA remaining unbound and the presence of additional components in the solution beyond just the bioconjugates, which could contribute to the observed differences in signal intensity across the different incubation times. The increased presence of unbound HSA and other species in the solution may also result in noisier spectra and make it more challenging to focus the microscope on the bioconjugates, as there are more components present than just the target conjugates. The 3-hour incubation period exhibits the highest intensity peaks, particularly around the HSA-specific 1015 cm^{-1} region. Although the overnight incubation still shows distinct peaks, its intensity is slightly lower than that of the 3-hour incubation. This suggests that a 3-hour incubation period may be optimal for obtaining a strong SERS signal when 990:1 HSA:AgNS, as it allows sufficient time for the HSA molecules to interact effectively with the AgNS substrate without significant degradation or aggregation, which could occur over longer periods.

A different pattern is observed in Figure 52B, which shows the SERS spectra for 9.9E6:1 HSA:AgNS at the same incubation times (15 min, 3 h and overnight). his concentration corresponds to the amount of HSA found in plasma, as we aimed to determine whether, without centrifugation, the SERS profile similar to that observed in the previous figure, potentially corresponding to HSA, would change under these conditions. In this case, the baseline intensity varies across all incubation durations, and SERS signals are notably weaker than those of the diluted samples. The lack of distinct, sharp bands in this figure samples suggests that overcrowding or aggregation may be an issue, potentially leading to a less effective interaction with the AgNS substrate. This may be due to steric hindrance or saturation of the surface binding sites, which could inhibit efficient SERS enhancement.

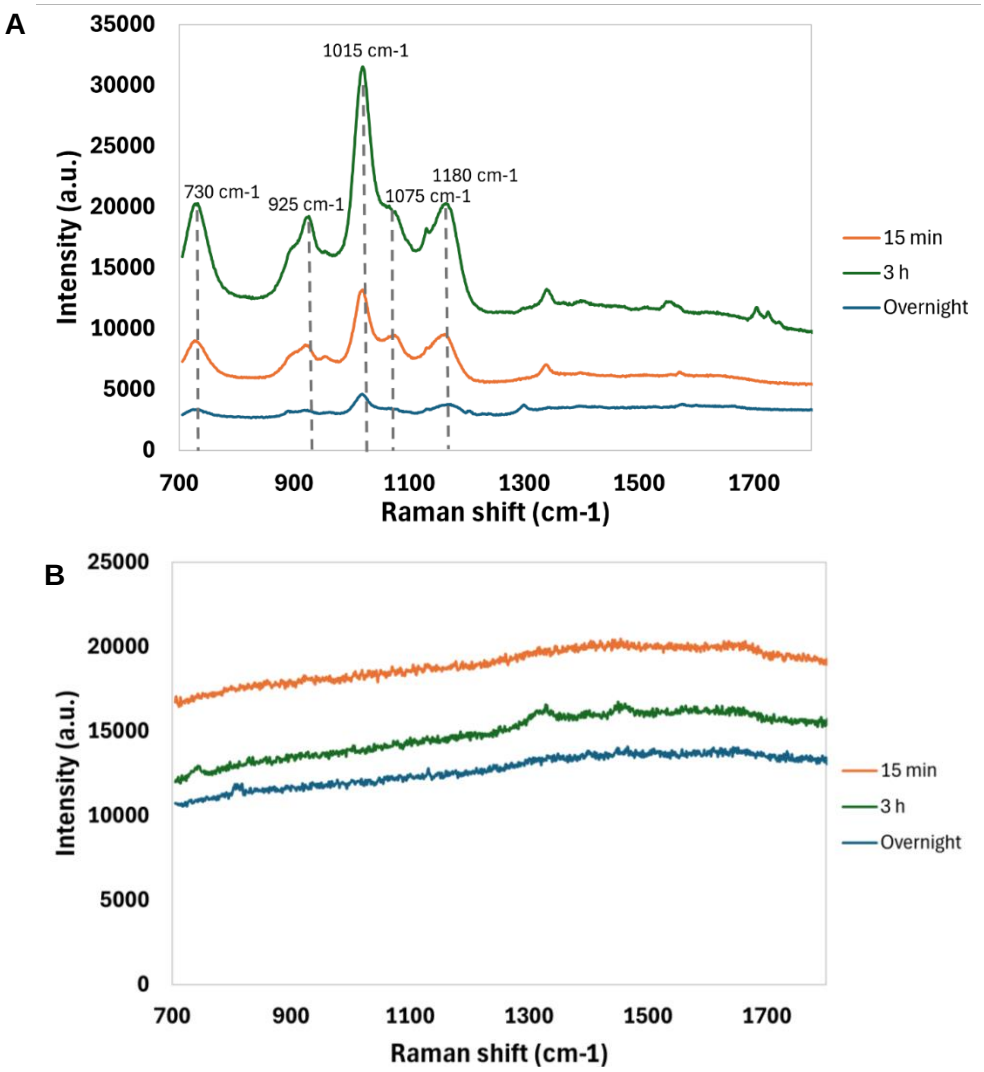

Figure 52. A. SERS spectra of 990:1 HSA:AgNS conjugate overtime on aluminium foil **B**. SERS spectra of 9.9E6:1 HSA:AgNS conjugate overtime on aluminium foil.

These findings highlight the importance of understanding how HSA binds in order to minimize its interference in SERS-based PoCT applications. By considering both dilution and incubation duration, this information can help refine preparatory strategies, ensuring optimal sensitivity and accuracy for real-world PoCT scenarios.

Figure 53A presents SERS spectra for 880:1 plasma:AgNS samples incubated for 15 minutes, 3 hours, and overnight. Spectra have extremely low intensities with barely discernible vibrational lines, worsening for higher incubations times.

Analyzing Figure 53B, depicting 8.8E6:1 plasma:AgNS, a different trend emerges. In this case, the SERS intensity increases with longer incubation times, peaking at 3 hours before slightly decreasing after overnight incubation. This suggests that this high concentrated sample, longer incubation enhances the interaction between plasma constituents and the enhancing substrate, likely due to a higher concentration of analytes being more effectively captured over time. The rise in intensity up to 3 hours may represent optimal conditions for strong SERS signals, while the slight

decrease after overnight incubation could result from saturation or changes in the analyte-substrate interaction over time. However, the data also show no significant difference between the 15-minute and 3-hour incubation times, indicating that 15 minutes could be enough to achieve high SERS intensities. For PoCT applications, where speed is crucial, a 15-minute incubation time would be ideal as it balances both signal intensity and operational efficiency.

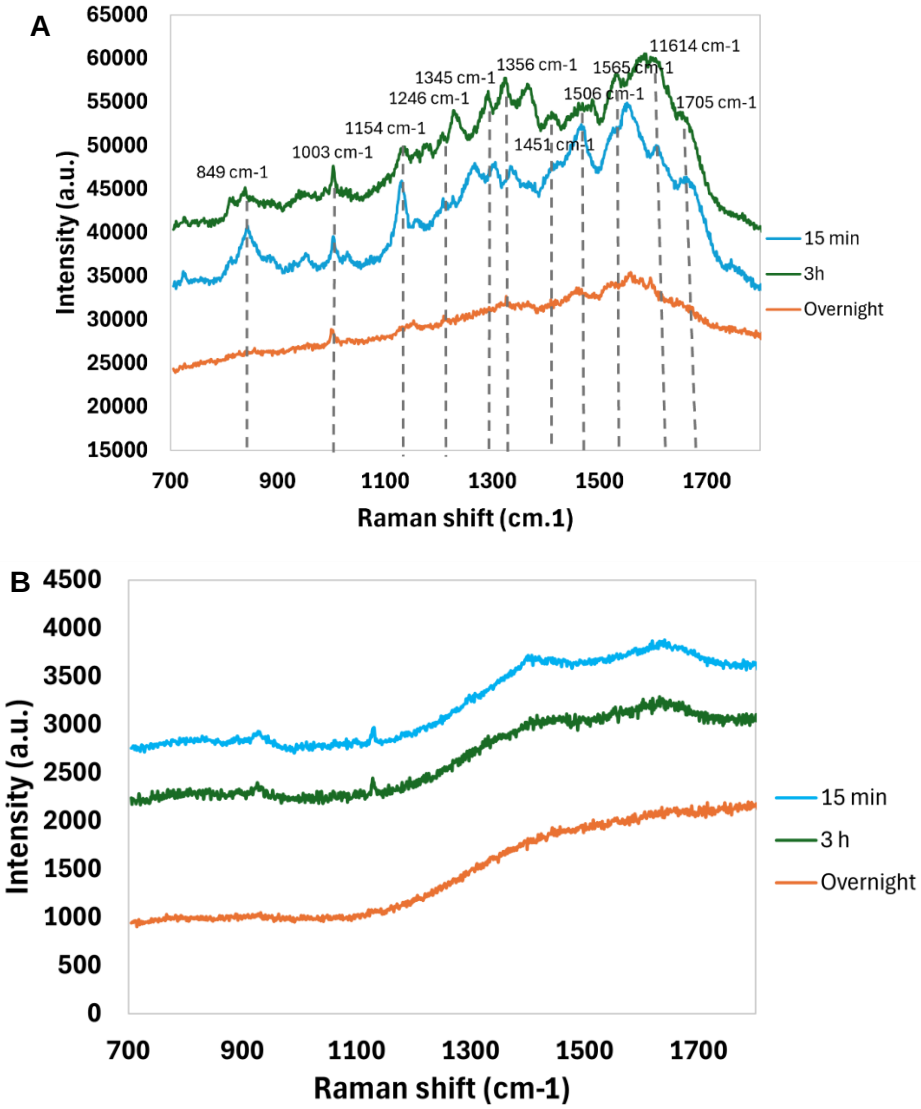

Figure 53. A. SERS spectra of plasma:AgNS conjugate overtime on aluminium foil. Plasma:AgNS ratio is 880:1 **B**. SERS spectra of 8.8E6:1 plasma:AgNS conjugate overtime on aluminium foil.

In conclusion, the results emphasize the importance of sample dilution and incubation time in optimizing SERS detection of HSA and plasma for PoCT applications. For diluted HSA samples, a 3-hour incubation yields the strongest SERS signals, allowing sufficient interaction with the AgNS substrate. However, a 15-minute incubation also produces high intensity with the characteristic HSA spectral profile. In

contrast, undiluted HSA samples show reduced SERS efficiency, likely due to overcrowding, indicating the need for careful concentration management.

For plasma samples, the optimal incubation time depends on dilution. Ration 880:1 plasma:AgNS did not yield detectable SERS peaks, while 8.8E6:1 plasma:AgNS showed the strongest signals at 3 hours; a 15-minute incubation produced similar intensity and spectral profiles. These findings suggest that incubation time and concentration should be tailored to the specific context to achieve optimal SERS performance, with 15 minutes being sufficient for rapid PoCT applications.

Overall, careful calibration of dilution and incubation parameters is crucial for accurate and sensitive detection in PoCT, maximizing the effectiveness of SERS-based diagnostics across different sample types.

3.7.2 DLS Analysis

Data presented in Figure 54 and Table 8 provides an analysis of how varying incubation times affect the Z-average (hydrodynamic diameter) and PDI of plasma:AgNS bioconjugates, which is critical for the development of PoCT applications using plasma as the biofluid for analysis.

Figure 54 shows the Z-average for Plasma:AgNS bioconjugates after incubation periods of 15 minutes, 3 hours, and overnight. Compared to the bare AgNSs, which have a Z-average of 90 nm, all plasma samples exhibit significantly larger hydrodynamic sizes. The sizes remain consistent across the three incubation times, ranging from 227 nm to 243 nm. This increase in size suggests that the plasma proteins rapidly adsorb onto the AgNS surface, forming stable bioconjugates within the first 15 minutes. The minor fluctuations in size among the different incubation times indicate that prolonged incubation does not lead to further significant growth in the hydrodynamic size, suggesting that the bioconjugation process reaches equilibrium relatively quickly.

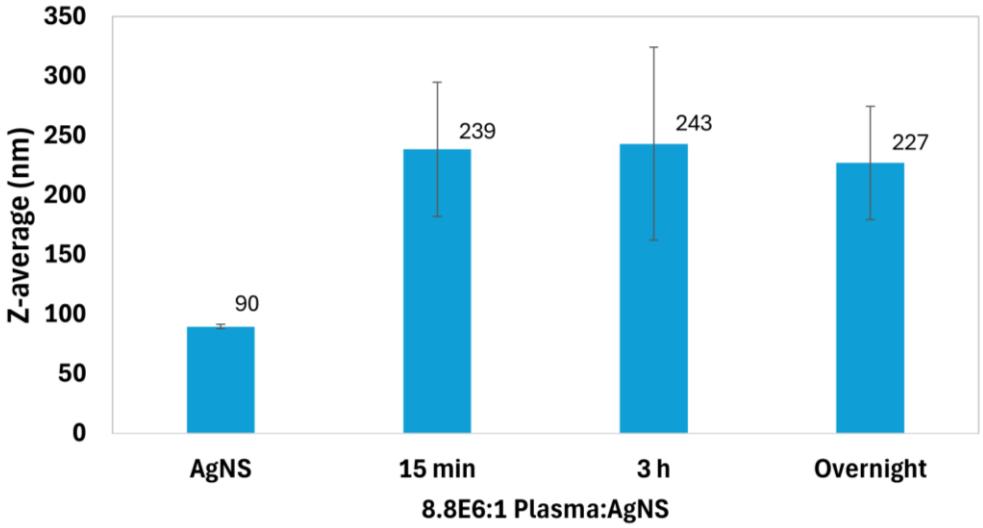

Figure 54. Z-average of 8.8E6:1 plasma:AgNS conjugate overtime (15 min, 3h and overnight).

Table 8. Polydispersity index of 8.8E6:1 plasma:AgNS conjugate over time.

	Polydispersity Index (PDI)					Average	SD
AgNS	0.108	0.257	0.372	0.294	0.053	0.22	0.12
15 min	0.146	0.04	0.331	0.033	0.367	0.18	0.14
3 h	0.185	0.233	0.118	0.282	0.304	0.22	0.07
Overnight	0.02	0.211	0.03	0.206	1.133	0.32	0.42

Table 8 summarizes the PDI values (the values for the five measurements obtained) for the same incubation periods reflecting the homogeneity of the particle size distribution. The AgNSs exhibit relatively low PDI values, indicating a narrow size distribution. The PDI for the Plasma bioconjugates, however, varies depending on the incubation time. After 15 minutes of incubation, the PDI is relatively low, suggesting that the bioconjugates are uniform in size. The PDI increases slightly for the 3-hour incubation, reflecting some degree of heterogeneity in particle size distribution. Interestingly, the overnight incubation results in a more pronounced increase in PDI, particularly in one of the measurements, which might suggest some aggregation or further interaction between plasma proteins and the AgNSs over extended incubation times.

These findings imply that a 15-minute incubation is sufficient to achieve effective bioconjugation for PoCT applications, providing a balance between achieving adequate coverage of AgNSs by plasma proteins and maintaining a low degree of polydispersity. This shorter incubation time would be advantageous in a clinical setting where rapid results are essential.

3.7.3 SDS PAGE Analysis

The SDS-PAGE presented in Figure 58, used the direct loading of plasma:AgNS bioconjugates at two different incubation times (3 hours and overnight) for three plasma:AgNS ratios (76003:1, 7.6E4:1 and 7.6E5:1 plasma:AgNS). The molecular weight (MW) marker on the left lane provides a reference for protein size. In appendix A8 figure A20 it is possible to observe a calibration curve that will determine the MW of the proteins adsorbed to the AgNS. In Table 10 MW, the different proteins observed in the SDS-PAGE is presented.

For the 3-hour incubation, distinct bands can be seen, particularly around the molecular weights of HSA (~83 kDa) and fibrinogen (~75 kDa), which align with the molecular weights reported in Table 8. The intensity of the bands suggests binding of plasma proteins to AgNS at the 7.6E5:1 and 7.6E4:1 plasma:AgNS ratios.

The gel reveals that shorter incubation times (3 hours) result in more distinct protein bands, indicating stronger and potentially more stable protein-AgNS interactions. From the gel, we can infer that the most concentrated samples provide valuable insights into the proteins adsorbed onto the AgNS. To gain a clearer understanding of

how these interactions evolve over time, the experiment should be repeated, including a 15-minute incubation period to observe the progression of protein adsorption dynamics.

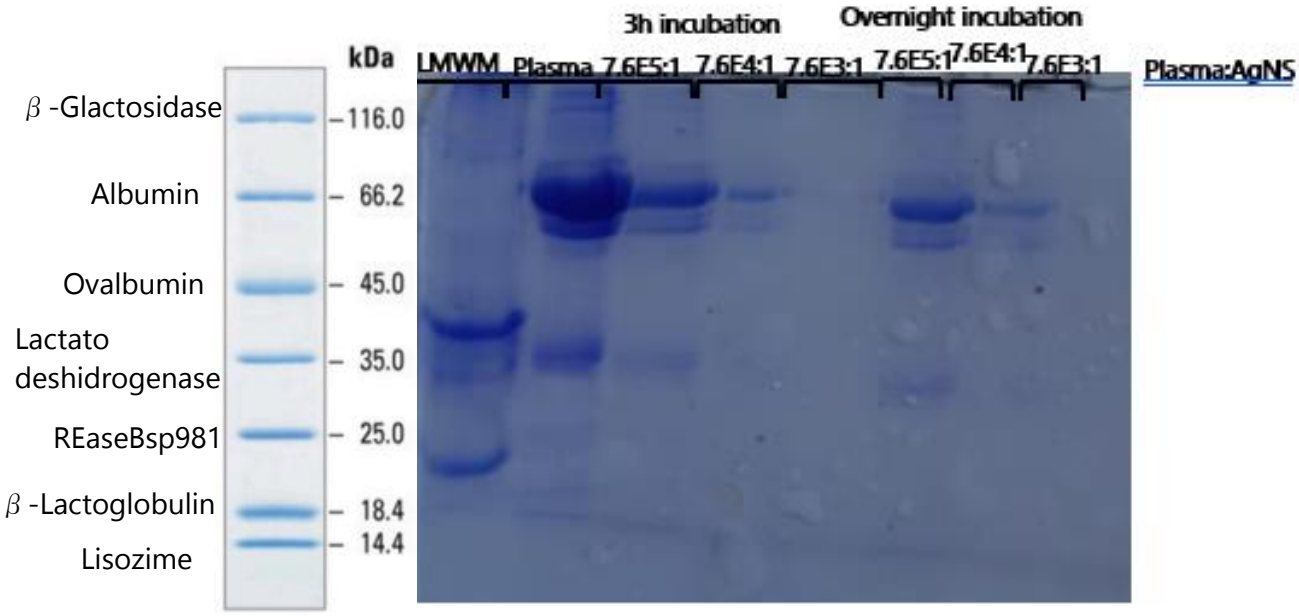

Figure 59. AgNS interaction with plasma proteins. SDS-PAGE Analysis following 3 h and overnight incubations.

Table 9. Molecular weights from proteins revealed in the SDS-PAGE from Figure 49.

Proteins	Molecular Weights (kDa)
7.6E5:1 plasma:AgNS - HSA 3h	83.48
7.6E5:1 plasma:AgNS - Fibrinogen gamma	75.69
7.6E5:1 plasma:AgNS - Carbonic anidrase	49.93
7.6E4:1 plasma:AgNS - HSA 3h	84.62
7.6E4:1 plasma:AgNS - Fibrinogen gamma	75.95
7.6E4:1 plasma:AgNS - HSA 3h	48.08
7.6E5:1 plasma:AgNS - HSA Overnight	81.56
7.6E5:1 plasma:AgNS – Fibrinogen gamma	73.17
7.6E5:1 plasma:AgNS - Carbonic anidrase	46.16
7.6E4:1 plasma:AgNS - HSA Overnight	80.97
7.6E4:1 plasma:AgNS - Fibrinogen gamma	73.26
Plasma 3.8E5 nM - HSA	82.08
Plasma 3.8E5 nM – Fibrinogen gamma	74.86
Plasma 3.8E5 nM – Carbonic anidrase	50.55

3.8 Different incubation times of GFAP to represent different HS levels

The objective of this section is to explore the varying incubation times of glial fibrillary acidic protein (GFAP) to represent different levels of hemorrhagic stroke (HS). The 0.1 ng/mL of GFAP was to mimic a low level of this protein corresponding to AIS in less than 1h and more than 3 h. The 0.5ng/mL of GFAP to mimic the HS after 3h. Lastly, 1 ng/mL to symbolize a very high level of GFAP, normally next morning after patient had an HS. Given the critical need for rapid and accurate diagnosis in PoCT, the analysis focuses on GFAP as a biomarker within the crucial first three hours following symptom onset.

3.8.1 SERS Analysis

The SERS spectra on aluminum foil in Figure 60 illustrates the analysis of GFAP at various concentrations added to plasma and incubated with AgNS for 15 minutes, 3 hours, and overnight. These are compared to bioconjugates with plasma only. Measurement parameters included a 20x objective, a laser power of 50 mW, and 3 scans with an exposure time of 5 seconds each. Five spectra were obtained for each sample.

The observed peaks suggest stronger interactions between GFAP and AgNS, likely due to higher GFAP concentrations leading to increased adsorption onto the AgNS surface. Notably, the highest SERS intensity and Raman shift areas are found in the 15-minute incubation samples across all GFAP concentrations, suggesting that shorter incubation times result in stronger signal enhancements.

The results also demonstrate that the SERS technique can detect GFAP at lower concentrations, as less intense but still identifiable peaks are observed at 0.1 ng/mL and 0.5 ng/mL. In contrast, the lowest curve, representing the plasma-only sample, shows significantly lower intensity and fewer distinct peaks compared to GFAP-containing samples. This highlights that GFAP presence substantially influences the SERS signal, though the influence does not scale directly with GFAP concentration, indicating that the GFAP signals are more pronounced than those from plasma alone.

A

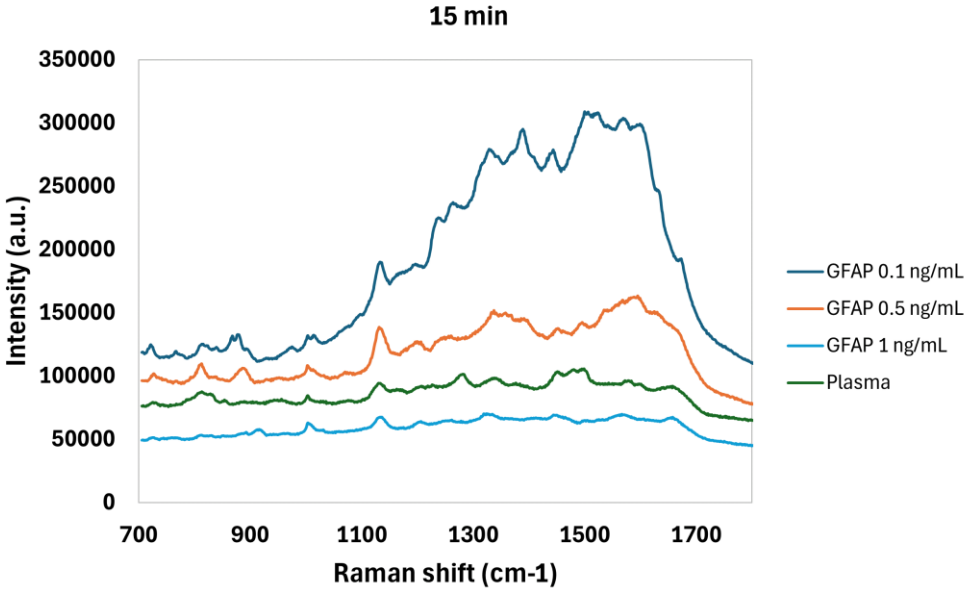
15 min
350000
300000
250000
200000
150000
100000
50000
0
Intensity (a.u.)
700
900
1100
1300
1500
1700
Raman shift (cm-1)
GFAP 0.1 ng/mL
GFAP 0.5 ng/mL
GFAP 1 ng/mL
Plasma

B

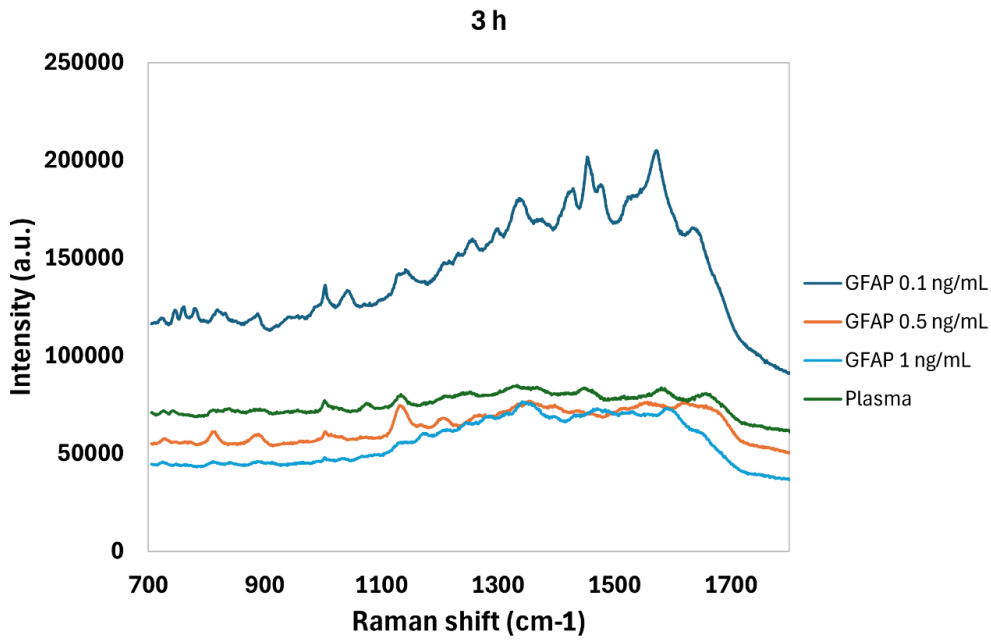
3 h
250000
200000
150000
100000
50000
0
Intensity (a.u.)
700
900
1100
1300
1500
1700
Raman shift (cm-1)
GFAP 0.1 ng/mL
GFAP 0.5 ng/mL
GFAP 1 ng/mL
Plasma

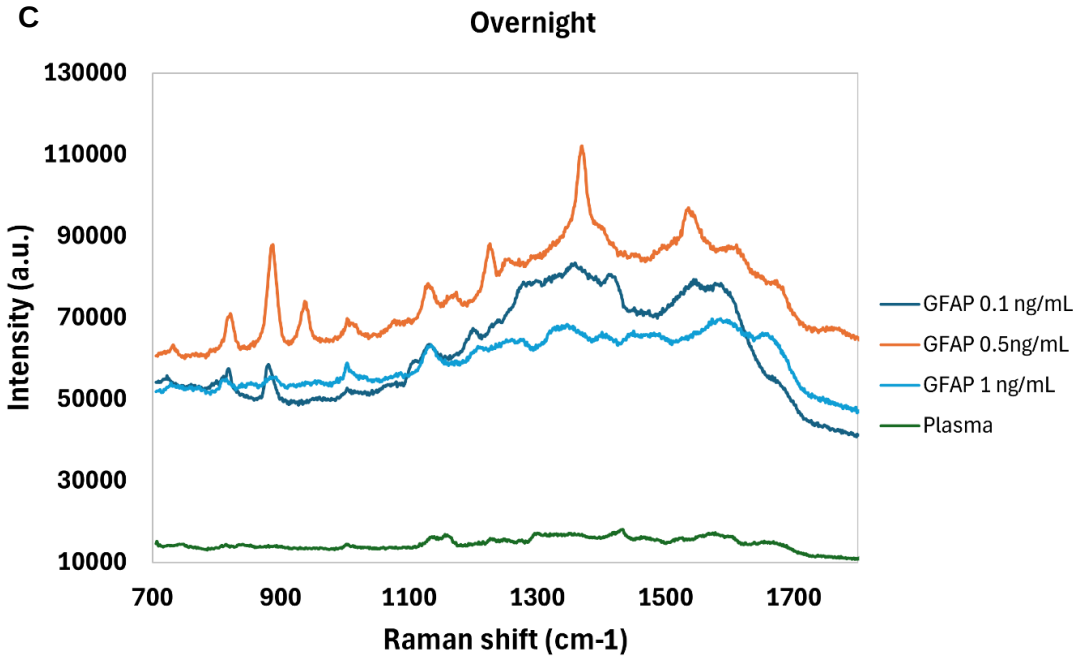

Figure 60. SERS spectra of plasma spiked with GFAP at different concentrations and then conjugated with AgNS, at different incubation times **A**. 15 min **B**. 3h **C**. Overnight.

3.8.2 DLS Analysis

In the analysis of different incubation times of GFAP to represent varying levels of hemorrhagic stroke (HS), DLS data reveals critical insights into the behavior of Plasma and Plasma spiked with GFAP bioconjugates at different concentrations and incubation times. Figure 61 shows the Z-average (hydrodynamic diameter) for plasma and PGFAP samples at different concentrations (0.1 ng/mL, 0.5 ng/mL, and 1 ng/mL) incubated for 15 minutes, 3 hours, and overnight.

For plasma-only samples (37 mg/mL), the Z-average remains relatively stable across different incubation times, ranging from 225 nm to 289 nm. This suggests that plasma proteins rapidly adsorb onto the AgNS surface, and the bioconjugation process does not undergo significant changes with extended incubation times. The 3-hour incubation generally shows the highest Z-average, with the most notable difference observed in the 10 ng/mL sample. In Appendix A10, the Z-average and zeta potential data for GFAP alone are presented. The unusually large sizes observed for these

samples suggest that issues may have occurred during the experimental procedure or processing.

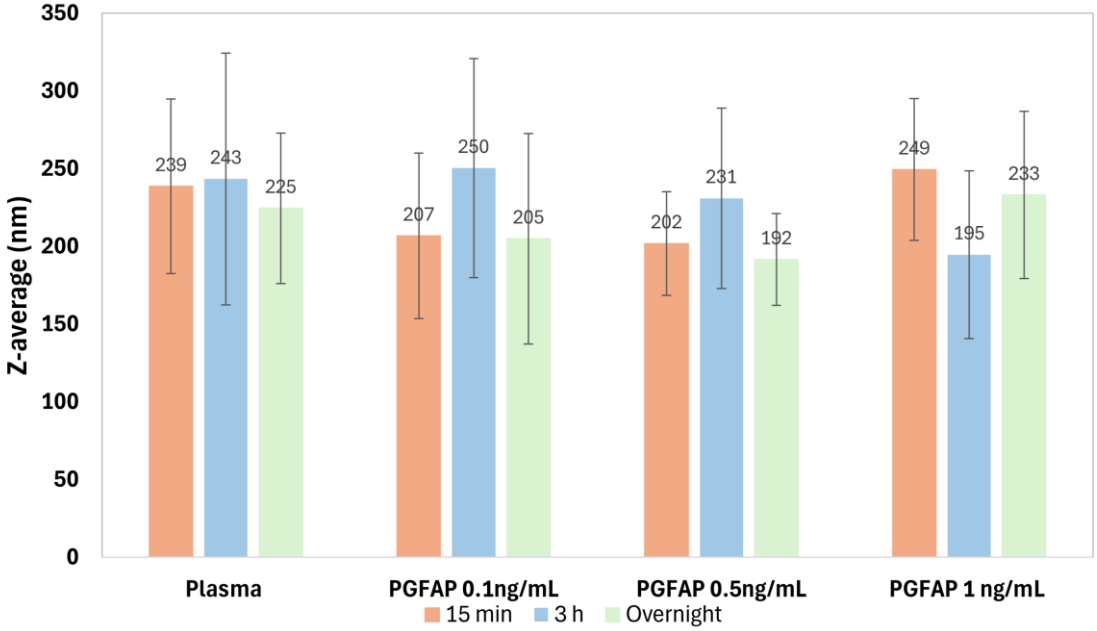

Figure 61. Z-average (nm) of plasma spiked with GFAP conjugated with AgNS at different incubation times.

Table 10. Polydispersity index (PDI) of plasma spiked with GFAP conjugated with AgNS in different incubation times.

		Polydispersity Index (PDI)					Average	SD
15 min	GFAP 0.1 ng/mL	0.23	0.269	0.264	0.038	0.317	0.22	0.10
	GFAP 0.5 ng/mL	0.147	0.019	0.26	0.113	0.15	0.14	0.08
	GFAP 1 ng/mL	0.292	0.081	0.087	0.09	0.252	0.16	0.09
	Plasma	0.146	0.04	0.331	0.033	0.367	0.18	0.14
3 h	GFAP 0.1 ng/mL	0.093	0.266	0.028	0.026	0.189	0.12	0.09
	GFAP 0.5 ng/mL	0.387	0.363	0.036	0.163	0.276	0.25	0.13
	GFAP 1 ng/mL	0.225	0.304	0.192	0.208	0.24	0.24	0.04
	Plasma	0.185	0.304	0.233	0.118	0.282	0.22	0.07
Over-night	GFAP 0.1 ng/mL	0.028	0.121	0.204	0.097	0.258	0.14	0.08
	GFAP 0.5 ng/mL	0.253	0.029	0.129	0.081	0.247	0.15	0.09
	GFAP 1 ng/mL	0.264	0.164	0.146	0.281	0.116	0.19	0.07
	Plasma	0.03	0.026	1.133	0.047	0.02	0.25	0.44

Table 10 provides PDI values for the same plasma samples, showing relatively low PDI values, which indicate a narrow size distribution and consistent bioconjugate formation. However, some aggregation occurred after overnight incubation, as evidenced by a few measurements showing PDI values greater than 0.4, which points to

the presence of aggregates. Additionally, as the concentration of GFAP spiked into plasma increases, the PDI values also tend to increase, suggesting that the presence of GFAP may lead to more heterogeneous particle sizes or induce further aggregation in the bioconjugates.

Figure 62 illustrates the zeta potential measurements of plasma samples treated with varying concentrations of GFAP (0.1 ng/mL, 0.5 ng/mL, and 1 ng/mL), GFAP, and untreated plasma. The values indicate a relatively consistent negative surface charge across all conditions, with the plasma sample exhibiting the most negative zeta potential (-32 mV). The Plasma spiked with GFAP-treated samples show slightly less negative values (-24 mV to -27 mV), with little variation between the different concentrations of PGFAP. The GFAP conjugated with AgNS sample presents a zeta potential of -28 mV, close to the untreated plasma sample but still less negative. The error bars demonstrate some variability in the measurements, though the differences between the samples are relatively small. Overall, these results suggest that the addition of Plasma spiked with GFAP or GFAP results in a slight reduction in the negative surface charge compared to untreated plasma, but the effect is relatively minimal across different concentrations.

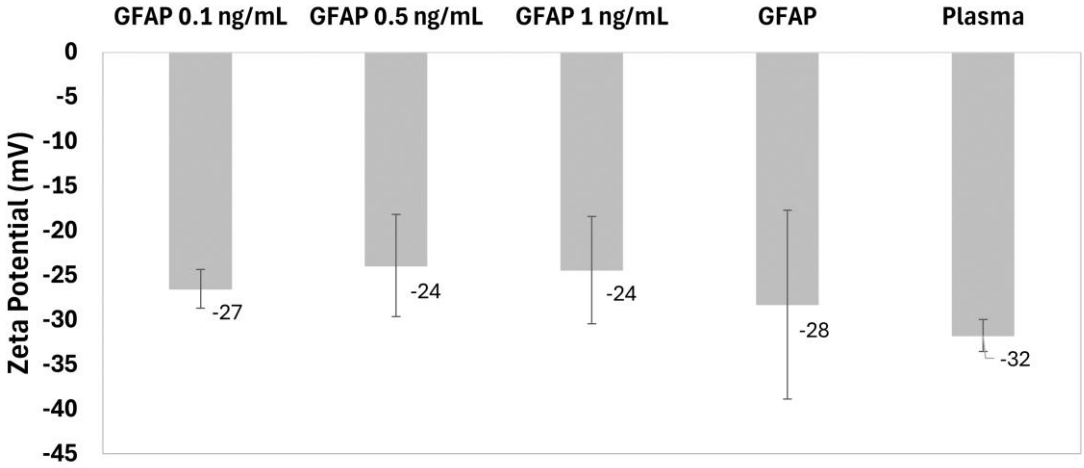

Figure 62. Zeta potential (mV) of plasma spiked with GFAP in different concentrations to represent the different levels in blood when a HS occurs, plasma and GFAP samples were used as controls.

Overall, the DLS analysis suggests that while shorter incubation times (15 minutes to 3 hours) are sufficient for stable and uniform bioconjugate formation at lower GFAP concentrations, higher concentrations of GFAP and extended incubation times lead to larger and more heterogeneous bioconjugates. This has important implications for PoCT applications, where rapid and consistent detection is critical. The increase in size and PDI at higher concentrations and longer incubation times could affect the sensitivity and reliability of the PoCT device, making it essential to optimize both the concentration of biomarkers like GFAP and the incubation times to ensure the most accurate and reproducible results. Additionally, zeta potential measurements indicate that higher GFAP and Plasma spiked with GFAP concentrations leads to a slight

reduction in the negative surface charge, suggesting potential alterations in bioconjugate stability. These findings further emphasize the importance of fine-tuning both biomarker concentrations and incubation conditions to enhance PoCT performance.

4. Conclusion and future perspectives

This dissertation presents the first steps for the development of a point-of-care test (PoCT) for stroke diagnosis using Surface-Enhanced Raman Spectroscopy (SERS) coupled with silver nanostars (AgNS) and Principal Component Analysis (PCA). The research successfully demonstrated the formation of bioconjugates evidenced by an increase in hydrodynamic size and changes in electrophoretic mobility. To explore whether albumin might obscure distinct plasma patterns measured by SERS, we compared the SERS analysis patterns of whole plasma, albumin alone, and plasma depleted of albumin.

Furthermore, we tested different SERS substrates, with aluminium foil and photocopy paper producing the most reliable and intense SERS signals, making them ideal candidates for future PoCT applications. These substrates demonstrated reduced signal-to-noise ratios and yielded spectra with high SERS intensity, narrow bands, and easily fit vibrational lines, suggesting their strong potential for integration into a diagnostic device. Additionally, key SERS parameters were optimized, including the use of a 20x laser objective, laser power between 10 and 50 mW, 3 scans, and 3 seconds of exposure time. For the plasma bioconjugates, our future matrix when translated to stroke samples, a plasma:AgNS ratio of $8.8x10^6$:1 provided optimal results, namely: narrow bands, low background noise, and measurable peaks as analysed by peak fit software. Our investigation into incubation times of different plasma:AgNS bioconjugates, a critical factor given stroke's time-dependent nature, revealed that spectra could be obtained in as little as 15 minutes. This underscores the feasibility of rapid diagnostics, which is essential for effective stroke management.

We also tested the Glial Fibrillary Acidic Protein (GFAP) as a biomarker of HS, measuring its performance at various concentrations and incubation times that reflect those seen in stroke patients. Although a more comprehensive statistical analysis is needed to determine whether plasma spiked with GFAP at different concentrations and incubation times yields distinct SERS spectra that can be distinguished by machine learning (ML). The results are promising for differentiating between stroke types using the proposed SERS-based detection method.

The application of PCA successfully distinguished between the three samples tested (HSA, Plasma, Plasma albumin-free), underscoring the potential for SERS, combined with statistical analysis, to identify stroke-related biomarkers in plasma. While more extensive data collection and machine learning (ML) optimization are needed, the integration of PCA and ML offers a path forward in developing an accurate, real-time diagnostic tool capable of distinguishing between stroke types and even stroke mimics.

Looking ahead, several important future directions can be considered. One promising avenue is to expand the biomarker panel beyond GFAP to include more stroke-related biomarkers, enhancing the diagnostic power of the SERS-based system for distinguishing between stroke types and other neurological conditions. Clinical validation is crucial; testing a broader range of clinical samples from diverse stroke patients will verify the diagnostic platform's robustness across various demographics, including gender, age, and co-morbidities.

Future research should also focus on integrating the SERS platform into portable, real-time diagnostic devices, optimizing it for use in emergency settings where rapid diagnosis is critical. Additionally, applying machine learning to enhance data analysis could improve accuracy in distinguishing stroke subtypes and predicting patient outcomes, leading to more sophisticated diagnostic tools.

As the technology approaches clinical application, establishing standardized protocols and collaborating with regulatory bodies will be necessary. Standardizing SERS substrate production, sample handling, and spectral analysis will ensure consistent and reliable diagnostic results. Longitudinal studies could explore the system's ability to diagnose strokes and provide prognostic information by monitoring biomarker levels over time, assessing recovery progress, and predicting secondary strokes. These advancements could position the research presented in this dissertation as a stepping stone toward developing a powerful, real-time diagnostic tool that could revolutionize stroke care.

5. BIBLIOGRAPHY

[1] D. Hovsepian and S.Karceski, "Stroke, tPA, and physician decision-making," *Neurology*, vol. 81, no. 13, Sep. 2013, doi: 10.1212/WNL.0B013E3182A94F3C

[2] American Heart Association, "Explaining Stroke," *National Stroke Association*, p. 43, 2018.

[3] R. G. Kowalski *et al.*, "Rapid Activation of Neuroinflammation in Stroke: Plasma and Extracellular Vesicles Obtained on a Mobile Stroke Unit," *Stroke*, vol. 54, no. 3, pp. E52–E57, Mar. 2023, doi: 10.1161/STROKEAHA.122.041422.

[4] A. Lekoubou, C. Nguyen, M. Kwon, A. D. Nyalundja, and A. Agrawal, "Post-stroke Everything," Nov. 01, 2023, *Springer*. doi: 10.1007/s11910-023-01308-9.

[5] "Global, Regional, and Country-Specific Lifetime Risks of Stroke, 1990 and 2016," *New England Journal of Medicine*, vol. 379, no. 25, pp. 2429–2437, Dec. 2018, doi: 10.1056/NEJMoa1804492.

[6] F. Shehjar *et al.*, "Stroke: Molecular mechanisms and therapies: Update on recent developments," *Neurochem Int*, vol. 162, Jan. 2023, doi: 10.1016/j.neuint.2022.105458.

[7] Luísa Fonseca, "O AVC é a principal causa de morte e incapacidade em Portugal," Sociedade Portuguesa de Medicina Interna. Accessed: Oct. 29, 2023. [Online]. Available: https://www.spmi.pt/o-avc-e-a-principal-causa-de-morte-e-incapacidade-em-portugal/

[8] M. Sousa-uva and C. M. Dias, "Prevalência de Acidente Vascular Cerebral na população portuguesa : dados da amostra ECOS 2013," *Boletim Epidemiológico INE*, vol. 9, no. 2, pp. 12–14, 2014, [Online]. Available: http://repositorio.insa.pt//handle/10400.18/2341

[9] Luísa Fonseca, "O AVC é a principal causa de morte e incapacidade em Portugal," Sociedade Portuguesa de Medicina Interna. Accessed: Oct. 29, 2023. [Online]. Available: https://www.spmi.pt/o-avc-e-a-principal-causa-de-morte-e-incapacidade-em-portugal/

[10] SNS, "Mortalidade por AVC Isquémico e Hemorrágico — Transparência," 2023. Accessed: Oct. 29, 2023. [Online]. Available:

https://transparencia.sns.gov.pt/explore/dataset/taxa-de-mortalidade-por-avc-isquemico-e-hemorragico/analyze/?flg=pt-pt&sort=tempo&q.timerange.tempo=tempo:%5B2016-01-01+TO+2023-10-29%5D&dataChart=eyJxdWVyaWVzIjpbeyJjaGFydHMiOlt7ImFsaWduTW9udGgiOnRydWUsInR

[11] "Stroke Facts | Stroke | CDC." Accessed: Sep. 18, 2024. [Online]. Available: https://www.cdc.gov/stroke/data-research/facts-stats/?CDC_AAref_Val=https://www.cdc.gov/stroke/facts.htm

[12] and B. I. National Heart, Lung, "Stroke - What Is a Stroke? | NHLBI, NIH," National Heart, Lung, and Blood Institute. Accessed: Oct. 29, 2023. [Online]. Available: https://www.nhlbi.nih.gov/health/stroke

[13] P. B. Gorelick, "Stroke Prevention." [Online]. Available: http://arch-neur.jamanetwork.com/

[14] C. Qin *et al.*, "Proteomic profiling of plasma biomarkers in acute ischemic stroke due to large vessel occlusion," *J Transl Med*, vol. 17, no. 1, Jul. 2019, doi: 10.1186/s12967-019-1962-8.

[15] J. Li *et al.*, "The role of protein glycosylation in the occurrence and outcome of acute ischemic stroke," May 01, 2023, *Academic Press*. doi: 10.1016/j.phrs.2023.106726.

[16] A. S. Zubair and K. N. Sheth, "Hemorrhagic Conversion of Acute Ischemic Stroke," *Neurotherapeutics*, vol. 20, no. 3, pp. 705–711, Apr. 2023, doi: 10.1007/S13311-023-01377-1.

[17] Y. Okada *et al.*, "Hemorrhagic Transformation in Cerebral Embolism." [Online]. Available: http://ahajournals.org

[18] M. Chawla, S. Sharma, J. Sivaswamy, and L. T. Kishore, "A method for automatic detection and classification of stroke from brain CT images," *Proceedings of the 31st Annual International Conference of the IEEE Engineering in Medicine and Biology Society: Engineering the Future of Biomedicine, EMBC 2009*, pp. 3581–3584, 2009, doi: 10.1109/IEMBS.2009.5335289.

[19] E. B. Marsh, S. Girgenti, E. J. Llinas, and A. O. Brunson, "Outcomes in Patients with Minor Stroke: Diagnosis and Management in the Post-thrombectomy Era," Apr. 01, 2023, *Springer Science and Business Media Deutschland GmbH*. doi: 10.1007/s13311-023-01349-5.

[20] K. S. Helboe, H. S. Eddelien, and C. Kruuse, "Visual symptoms in acute stroke – A systematic review of observational studies," Jun. 01, 2023, *Elsevier B.V.* doi: 10.1016/j.clineuro.2023.107749.

[21] P. Lipton, "Ischemic Cell Death in Brain Neurons," 1999. doi: 10.1152/physrev.1999.79.4.1431.

[22] C. Iadecola and J. Anrather, "The immunology of stroke: From mechanisms to translation," Jul. 2011. doi: 10.1038/nm.2399.

[23] A. Risitano and D. Toni, "Time is brain: Timing of revascularization of brain arteries in stroke," 2020, *Oxford University Press*. doi: 10.1093/EURHEARTJ/SUAA157.

[24] J. L. Saver, "Time is brain - Quantified," Jan. 2006. doi: 10.1161/01.STR.0000196957.55928.ab.

[25] J. A. Oostema, M. Nasiri, T. Chassee, and M. J. Reeves, "The quality of prehospital ischemic stroke care: Compliance with guidelines and impact on in-hospital stroke response," *Journal of Stroke and Cerebrovascular Diseases*, vol. 23, no. 10, pp. 2773–2779, 2014, doi: 10.1016/j.jstrokecerebrovasdis.2014.06.030.

[26] T. F. Hasan *et al.*, "Diagnosis and Management of Acute Ischemic Stroke," *Mayo Clin Proc*, vol. 93, no. 4, pp. 523–538, Apr. 2018, doi: 10.1016/J.MAYOCP.2018.02.013.

[27] R. Hurford, A. Sekhar, T. A. T. Hughes, and K. W. Muir, "Diagnosis and management of acute ischaemic stroke," *Pract Neurol*, vol. 20, no. 4, pp. 306–318, Aug. 2020, doi: 10.1136/practneurol-2020-002557.

[28] P. Kakkar, T. Kakkar, T. Patankar, and S. Saha, "Current approaches and advances in the imaging of stroke," Dec. 01, 2021, *Company of Biologists Ltd*. doi: 10.1242/dmm.048785.

[29] S. Misra *et al.*, "Blood biomarkers for the diagnosis and differentiation of stroke: A systematic review and meta-analysis," Oct. 01, 2020, *SAGE Publications Inc.* doi: 10.1177/1747493020946157.

[30] D. Harpaz, E. Eltzov, R. C. S. Seet, R. S. Marks, and A. I. Y. Tok, "Point-of-care-testing in acute stroke management: An unmet need ripe for technological Harvest," Aug. 03, 2017, *MDPI*. doi: 10.3390/bios7030030.

[31] CDC, "Treat and Recover from Stroke," *Centers for Disease Control and Prevention*, 2022.

[32] C. W. Tsao *et al.*, "Heart Disease and Stroke Statistics-2023 Update: A Report From the American Heart Association," *Circulation*, vol. 147, no. 8, pp. E93–E621, Feb. 2023, doi: 10.1161/CIR.0000000000001123.

[33] D. O. Kleindorfer *et al.*, "2021 Guideline for the Prevention of Stroke in Patients With Stroke and Transient Ischemic Attack: A Guideline From the American Heart

Association/American Stroke Association," Jul. 01, 2021, *Wolters Kluwer Health*. doi: 10.1161/STR.0000000000000375.

[34] F. Z. Caprio and F. A. Sorond, "Cerebrovascular Disease: Primary and Secondary Stroke Prevention," Mar. 01, 2019, *W.B. Saunders*. doi: 10.1016/j.mcna.2018.10.001.

[35] R. Sharma *et al.*, "Proteomic signature of endothelial dysfunction identified in the serum of acute ischemic stroke patients by the iTRAQ-based LC-MS approach," *J Proteome Res*, vol. 14, no. 6, pp. 2466–2479, 2015, doi: 10.1021/pr501324n.

[36] L. Catanese, J. Tarsia, and M. Fisher, "Acute Ischemic Stroke Therapy Overview," Feb. 03, 2017, *Lippincott Williams and Wilkins*. doi: 10.1161/CIRCRESAHA.116.309278.

[37] S. Tiedt *et al.*, "Circulating Metabolites Differentiate Acute Ischemic Stroke from Stroke Mimics," *Ann Neurol*, vol. 88, no. 4, pp. 736–746, 2020, doi: 10.1002/ana.25859.

[38] L. di Biase, A. Bonura, P. M. Pecoraro, S. P. Carbone, and V. Di Lazzaro, "Unlocking the Potential of Stroke Blood Biomarkers: Early Diagnosis, Ischemic vs. Haemorrhagic Differentiation and Haemorrhagic Transformation Risk: A Comprehensive Review," Jul. 01, 2023, *Multidisciplinary Digital Publishing Institute (MDPI)*. doi: 10.3390/ijms241411545.

[39] "Via Verde AVC. O socorro ultrarrápido que salva vidas quando o sangue não chega ao cérebro – Observador." Accessed: Jul. 30, 2024. [Online]. Available: https://observador.pt/especiais/via-verde-avc-o-socorro-ultrarrapido-que-salva-vidas-quando-o-sangue-nao-chega-ao-cerebro/

[40] L. Long, W. Ju, H. Y. Yang, and Z. Li, "Dimensional Design for Surface-Enhanced Raman Spectroscopy," 2022, *American Chemical Society*. doi: 10.1021/acsmaterialsau.2c00005.

[41] P. L. Stiles, J. A. Dieringer, N. C. Shah, and R. P. Van Duyne, "Surface-enhanced Raman spectroscopy," 2008. doi: 10.1146/annurev.anchem.1.031207.112814.

[42] D. M. Solís, J. M. Taboada, F. Obelleiro, L. M. Liz-Marzán, and F. J. García De Abajo, "Optimization of Nanoparticle-Based SERS Substrates through Large-Scale Realistic Simulations," *ACS Photonics*, vol. 4, no. 2, pp. 329–337, Feb. 2017, doi: 10.1021/acsphotonics.6b00786.

[43] S. Schlücker, "Surface-enhanced raman spectroscopy: Concepts and chemical applications," May 05, 2014, *Wiley-VCH Verlag*. doi: 10.1002/anie.201205748.

[44] J. Langer *et al.*, "Present and future of surface-enhanced Raman scattering," Jan. 28, 2020, *American Chemical Society*. doi: 10.1021/acsnano.9b04224.

[45] R. Peng, T. Zhang, S. Yan, Y. Song, X. Liu, and J. Wang, "Recent Development and Applications of Stretchable SERS Substrates," Nov. 01, 2023, *Multidisciplinary Digital Publishing Institute (MDPI)*. doi: 10.3390/nano13222968.

[46] B. Yang *et al.*, "Recent Development of SERS Technology: Semiconductor-Based Study," *ACS Omega*, vol. 4, no. 23, pp. 20101–20108, Dec. 2019, doi: 10.1021/acsomega.9b03154.

[47] D. Song, R. Yang, F. Long, and A. Zhu, "Applications of magnetic nanoparticles in surface-enhanced Raman scattering (SERS) detection of environmental pollutants," Jun. 01, 2019, *Chinese Academy of Sciences*. doi: 10.1016/j.jes.2018.07.004.

[48] K. Yuan, B. Jurado-Sánchez, and A. Escarpa, "Nanomaterials meet surface-enhanced Raman scattering towards enhanced clinical diagnosis: a review," Dec. 01, 2022, *BioMed Central Ltd*. doi: 10.1186/s12951-022-01711-3.

[49] Y. Yang *et al.*, "Rapid and quantitative detection of respiratory viruses using surface-enhanced Raman spectroscopy and machine learning," *Biosens Bioelectron*, vol. 217, Dec. 2022, doi: 10.1016/j.bios.2022.114721.

[50] Z. Yi *et al.*, "Arrays of ZnO nanorods decorated with Au nanoparticles as surface-enhanced Raman scattering substrates for rapid detection of trace melamine," *Physica B Condens Matter*, vol. 451, pp. 58–62, Nov. 2014, doi: 10.1016/j.physb.2014.06.026.

[51] F. J. García-Vidal and J. B. Pendry, "Collective Theory for Surface Enhanced Raman Scattering," 1996.

[52] R. F. Aroca, "Plasmon enhanced spectroscopy," *Physical Chemistry Chemical Physics*, vol. 15, no. 15, pp. 5355–5363, Apr. 2013, doi: 10.1039/c3cp44103b.

[53] M. J. Oliveira *et al.*, "Office paper decorated with silver nanostars-an alternative cost effective platform for trace analyte detection by SERS," *Sci Rep*, vol. 7, no. 1, Dec. 2017, doi: 10.1038/s41598-017-02484-8.

[54] S. Cong, X. Liu, Y. Jiang, W. Zhang, and Z. Zhao, "Surface Enhanced Raman Scattering Revealed by Interfacial Charge-Transfer Transitions," Nov. 25, 2020, *Cell Press*. doi: 10.1016/j.xinn.2020.100051.

[55] K. Wang, S. Li, M. Petersen, S. Wang, and X. Lu, "Detection and characterization of antibiotic-resistant bacteria using surface-enhanced raman spectroscopy," Oct. 01, 2018, *MDPI AG*. doi: 10.3390/nano8100762.

[56] A. Araújo *et al.*, "Highly efficient nanoplasmonic SERS on cardboard packaging substrates," *Nanotechnology*, vol. 25, no. 41, Oct. 2014, doi: 10.1088/0957-4484/25/41/415202.

[57] L. Vázquez-Iglesias *et al.*, "SERS sensing for cancer biomarker: Approaches and directions," Apr. 01, 2024, *KeAi Communications Co.* doi: 10.1016/j.bioactmat.2023.12.018.

[58] S. Laing, L. E. Jamieson, K. Faulds, and D. Graham, "Surface-enhanced Raman spectroscopy for in vivo biosensing," *Nature Reviews Chemistry 2017 1:8*, vol. 1, no. 8, pp. 1–19, Aug. 2017, doi: 10.1038/s41570-017-0060.

[59] W. Dawuti *et al.*, "Label-free surface-enhanced Raman spectroscopy of serum with machine-learning algorithms for gallbladder cancer diagnosis," *Photodiagnosis Photodyn Ther*, vol. 42, Jun. 2023, doi: 10.1016/j.pdpdt.2023.103544.

[60] R. Xiao *et al.*, "Non-invasive detection of hepatocellular carcinoma serum metabolic profile through surface-enhanced Raman spectroscopy," *Nanomedicine*, vol. 12, no. 8, pp. 2475–2484, Nov. 2016, doi: 10.1016/j.nano.2016.07.014.

[61] S. Tripathy, S. Chavva, G. L. Coté, and S. Mabbott, "Modular and handheld Raman systems for SERS-based point-of-care diagnostics," Dec. 01, 2023, *Elsevier B.V.* doi: 10.1016/j.cobme.2023.100488.

[62] K. Kneipp, H. Kneipp, and J. Kneipp, "Surface-enhanced raman scattering in local optical fields of silver and gold nanoaggregates - From single-molecule raman spectroscopy to ultrasensitive probing in live cells," *Acc Chem Res*, vol. 39, no. 7, pp. 443–450, Jul. 2006, doi: 10.1021/ar050107x.

[63] A. Kudelski, "Nanomaterials for Surface Enhanced Raman Spectroscopy," Feb. 01, 2023, *MDPI*. doi: 10.3390/nano13030402.

[64] L. M. Liz-Marzán, "Tailoring surface plasmons through the morphology and assembly of metal nanoparticles," *Langmuir*, vol. 22, no. 1, pp. 32–41, Jan. 2006, doi: 10.1021/la0513353.

[65] L. Rodríguez-Lorenzo, R. A. Álvarez-Puebla, F. J. G. De Abajo, and L. M. Liz-Marzán, "Surface enhanced Raman scattering using star-shaped gold colloidal nanoparticles," *Journal of Physical Chemistry C*, vol. 114, no. 16, pp. 7336–7340, Apr. 2010, doi: 10.1021/jp909253w.

[66] F. R. Gómez *et al.*, "Surface plasmon resonances in silver nanostars," *Sensors*, vol. 18, no. 11, Nov. 2018, doi: 10.3390/s18113821.

[67] D. B. Grys, R. Chikkaraddy, M. Kamp, O. A. Scherman, J. J. Baumberg, and B. de Nijs, "Eliminating irreproducibility in SERS substrates," *Journal of Raman Spectroscopy*, vol. 52, no. 2, pp. 412–419, Feb. 2021, doi: 10.1002/jrs.6008.

[68] M. P. de Almeida, N. Leopold, R. Franco, and E. Pereira, "Expedite SERS fingerprinting of Portuguese white wines using plasmonic silver nanostars," *Front Chem*, vol. 7, no. MAY, 2019, doi: 10.3389/fchem.2019.00368.

[69] A. Garcia-Leis, J. V. Garcia-Ramos, and S. Sanchez-Cortes, "Silver nanostars with high SERS performance," *Journal of Physical Chemistry C*, vol. 117, no. 15, pp. 7791–7795, Apr. 2013, doi: 10.1021/JP401737Y/SUPPL_FILE/JP401737Y_SI_001.PDF.

[70] M. P. de Almeida *et al.*, "Silver Nanostar-Based SERS for the Discrimination of Clinically Relevant Acinetobacter baumannii and Klebsiella pneumoniae Species and Clones," *Biosensors (Basel)*, vol. 13, no. 2, Feb. 2023, doi: 10.3390/bios13020149.

[71] "Reducing Agents in Colloidal Nanoparticle Synthesis," *Royal Society of Chemistry*, May 2021, doi: 10.1039/9781839163623.

[72] Sebastian. Schlücker, *Surface enhanced Raman spectroscopy : analytical, biophysical and life science applications*. Wiley-VCH, 2011.

[73] M. J. Oliveira *et al.*, "Office paper decorated with silver nanostars-an alternative cost effective platform for trace analyte detection by SERS," *Sci Rep*, vol. 7, no. 1, Dec. 2017, doi: 10.1038/s41598-017-02484-8.

[74] S. Farooq, F. Dias Nunes, and R. E. de Araujo, "Optical properties of silver nanoplates and perspectives for biomedical applications," *Photonics Nanostruct*, vol. 31, pp. 160–167, Sep. 2018, doi: 10.1016/j.photonics.2018.07.001.

[75] Y. Fu, M. Xin, J. Chong, R. Li, and M. Huang, "Plasmonic gold nanostars@ZIF-8 nanocomposite for the ultrasensitive detection of gaseous formaldehyde," *J Mater Sci*, vol. 56, no. 6, pp. 4151–4160, Feb. 2021, doi: 10.1007/s10853-020-05507-4.

[76] E. P. Hoppmann, W. W. Yu, and I. M. White, "Highly sensitive and flexible inkjet printed SERS sensors on paper," *Methods*, vol. 63, no. 3, pp. 219–224, Oct. 2013, doi: 10.1016/j.ymeth.2013.07.010.

[77] W. Zhao and A. Van Den Berg, "Lab on paper," 2008, *Royal Society of Chemistry*. doi: 10.1039/b814043j.

[78] W. W. Yu and I. M. White, "A simple filter-based approach to surface enhanced Raman spectroscopy for trace chemical detection," *Analyst*, vol. 137, no. 5, pp. 1168–1173, Mar. 2012, doi: 10.1039/c2an15947c.

[79] T. Shabatina, O. Vernaya, A. Shumilkin, A. Semenov, and M. Melnikov, "Nanoparticles of Bioactive Metals/Metal Oxides and Their Nanocomposites with Antibacterial Drugs for Biomedical Applications," May 01, 2022, *MDPI*. doi: 10.3390/ma15103602.

[80] "Plasma SERS DeepLearning_AdvFuncMat2021".

[81] D. R. Parachalil, J. McIntyre, and H. J. Byrne, "Potential of Raman spectroscopy for the analysis of plasma/serum in the liquid state: recent advances," Apr. 01, 2020, *Springer*. doi: 10.1007/s00216-019-02349-1.

[82] S. Lee, J. Oh, K. Lee, M. Cho, B. Paulson, and J. K. Kim, "Diagnosis of Ischemic Renal Failure Using Surface-Enhanced Raman Spectroscopy and a Machine Learning Algorithm," *Anal Chem*, vol. 94, no. 50, pp. 17477–17484, Dec. 2022, doi: 10.1021/acs.analchem.2c03634.

[83] J. P. Marto *et al.*, "Proteomics to Identify New Blood Biomarkers for Diagnosing Patients With Acute Stroke," *J Am Heart Assoc*, vol. 12, no. 22, Nov. 2023, doi: 10.1161/JAHA.123.030021.

[84] Q. Li *et al.*, "Multi-Level Biomarkers for Early Diagnosis of Ischaemic Stroke: A Systematic Review and Meta-Analysis," Sep. 01, 2023, *Multidisciplinary Digital Publishing Institute (MDPI)*. doi: 10.3390/ijms241813821.

[85] W. G. Balogun, H. Zetterberg, K. Blennow, and T. K. Karikari, "Plasma biomarkers for neurodegenerative disorders: ready for prime time?," Mar. 01, 2023, *Lippincott Williams and Wilkins*. doi: 10.1097/YCO.0000000000000851.

[86] R. Beeram, K. R. Vepa, and V. R. Soma, "Recent Trends in SERS-Based Plasmonic Sensors for Disease Diagnostics, Biomolecules Detection, and Machine Learning Techniques," Mar. 01, 2023, *MDPI*. doi: 10.3390/bios13030328.

[87] A. Bonifacio *et al.*, "Surface-enhanced Raman spectroscopy of blood plasma and serum using Ag and Au nanoparticles: A systematic study," *Anal Bioanal Chem*, vol. 406, no. 9–10, pp. 2355–2365, Apr. 2014, doi: 10.1007/s00216-014-7622-1.

[88] S. K. Das, T. S. Bhattacharya, M. Ghosh, and J. Chowdhury, "Probing blood plasma samples for the detection of diabetes using SERS aided by PCA and LDA multivariate data analyses," *New Journal of Chemistry*, vol. 45, no. 5, pp. 2670–2682, Feb. 2021, doi: 10.1039/d0nj04508j.

[89] R. Maier, M. R. Fries, C. Buchholz, F. Zhang, and F. Schreiber, "Human versus Bovine Serum Albumin: A Subtle Difference in Hydrophobicity Leads to Large Differences in Bulk and Interface Behavior," *Cryst Growth Des*, vol. 21, no. 9, pp. 5451–5459, Sep. 2021, doi: 10.1021/acs.cgd.1c00730.

[90] Z. Liu and X. Chen, "Simple bioconjugate chemistry serves great clinical advances: Albumin as a versatile platform for diagnosis and precision therapy," Mar. 07, 2016, *Royal Society of Chemistry*. doi: 10.1039/c5cs00158g.

[91] G. J. Quinlan, G. S. Martin, and T. W. Evans, "Albumin: Biochemical properties and therapeutic potential," Jun. 2005. doi: 10.1002/hep.20720.

[92] M. P. Monopoli, C. Åberg, A. Salvati, and K. A. Dawson, "Biomolecular coronas provide the biological identity of nanosized materials," *Nat Nanotechnol*, vol. 7, no. 12, pp. 779–786, 2012, doi: 10.1038/nnano.2012.207.

[93] G. Bashiri, M. S. Padilla, K. L. Swingle, S. J. Shepherd, M. J. Mitchell, and K. Wang, "Nanoparticle protein corona: from structure and function to therapeutic targeting," Jan. 19, 2023, *Royal Society of Chemistry*. doi: 10.1039/d2lc00799a.

[94] K. Nienhaus and G. U. Nienhaus, "Mechanistic Understanding of Protein Corona Formation around Nanoparticles: Old Puzzles and New Insights," Jul. 12, 2023, *John Wiley and Sons Inc*. doi: 10.1002/smll.202301663.

[95] J. H. Shannahan, X. Lai, P. C. Ke, R. Podila, J. M. Brown, and F. A. Witzmann, "Silver Nanoparticle Protein Corona Composition in Cell Culture Media," *PLoS One*, vol. 8, no. 9, Sep. 2013, doi: 10.1371/journal.pone.0074001.

[96] I. Lynch and K. A. Dawson, "Protein-nanoparticle interactions," 2008. doi: https://doi.org/10.1016/S1748-0132(08)70014-8.

[97] S. Tenzer *et al.*, "Nanoparticle size is a critical physicochemical determinant of the human blood plasma corona: A comprehensive quantitative proteomic analysis," *ACS Nano*, vol. 5, no. 9, pp. 7155–7167, Sep. 2011, doi: 10.1021/nn201950e.

[98] C. Foerch *et al.*, "Serum glial fibrillary acidic protein as a biomarker for intracerebral haemorrhage in patients with acute stroke," *J Neurol Neurosurg Psychiatry*, vol. 77, no. 2, pp. 181–184, Feb. 2006, doi: 10.1136/jnnp.2005.074823.

[99] O. S. Mattila *et al.*, "Ultra-Early Differential Diagnosis of Acute Cerebral Ischemia and Hemorrhagic Stroke by Measuring the Prehospital Release Rate of GFAP," *Clin Chem*, vol. 67, no. 10, pp. 1361–1372, Oct. 2021, doi: 10.1093/clinchem/hvab128.

[100] G. G. Buyukgoz, M. Soforoglu, N. Basaran Akgul, and I. H. Boyaci, "Spectroscopic fingerprint of tea varieties by surface enhanced Raman spectroscopy," *J Food Sci Technol*, vol. 53, no. 3, pp. 1709–1716, Mar. 2016, doi: 10.1007/s13197-015-2088-5.

[101] L. Cui *et al.*, "Deep Learning in Ischemic Stroke Imaging Analysis: A Comprehensive Review," 2022, *Hindawi Limited*. doi: 10.1155/2022/2456550.

[102] S. Lee, J. Oh, K. Lee, M. Cho, B. Paulson, and J. K. Kim, "Diagnosis of Ischemic Renal Failure Using Surface-Enhanced Raman Spectroscopy and a Machine Learning Algorithm," *Anal Chem*, vol. 94, no. 50, pp. 17477–17484, Dec. 2022, doi: 10.1021/acs.analchem.2c03634.

[103] A. H. Nguyen, E. A. Peters, and Z. D. Schultz, "Bioanalytical applications of surface-enhanced Raman spectroscopy: De novo molecular identification," *Rev Anal Chem*, vol. 36, no. 4, Jul. 2017, doi: 10.1515/revac-2016-0037.

[104] A. Sawan, M. Awad, and R. Qasrawi, "Classification of Stroke Using Machine Learning Techniques: Review Study," in *2023 International Conference on Control, Automation*

and Diagnosis, ICCAD 2023, Institute of Electrical and Electronics Engineers Inc., 2023. doi: 10.1109/ICCAD57653.2023.10152317.

[105] "nanoPartica SZ-100V2 Series Nanoparticle Analyzer - HORIBA." Accessed: Jul. 20, 2024. [Online]. Available: https://www.horiba.com/int/scientific/products/detail/action/show/Product/nanopartica-sz-100v2-series-1945/

[106] "Protein Determination by the Bicinchoninic Acid (BCA) Method." Accessed: Jul. 16, 2024. [Online]. Available: https://www.sigmaaldrich.com/PT/en/technical-documents/protocol/protein-biology/protein-quantitation/protein-determination-by-the-bicinchoninic-acid-bca-method

[107] "Pierce_BCA_Protein_Assay".

[108] J. Cortés-Ríos *et al.*, "Protein quantification by bicinchoninic acid (BCA) assay follows complex kinetics and can be performed at short incubation times," *Anal Biochem*, vol. 608, Nov. 2020, doi: 10.1016/j.ab.2020.113904.

[109] O. S. Mattila *et al.*, "Ultra-Early Differential Diagnosis of Acute Cerebral Ischemia and Hemorrhagic Stroke by Measuring the Prehospital Release Rate of GFAP," *Clin Chem*, vol. 67, no. 10, pp. 1361–1372, Oct. 2021, doi: 10.1093/clinchem/hvab128.

[110] "AlbuminOUT ™." [Online]. Available: www.GBiosciences.com

[111] Malvern Instruments Ltd., "Dynamic light scattering: An introduction in 30 minutes. Tecnical note (MRK656-01)," *Technical Note MRK656-01*, pp. 1–8, 2018, [Online]. Available: https://www.malvernpanalytical.com/en/learn/knowledge-center/technical-notes/TN101104DynamicLightScatteringIntroduction

[112] "Nanoparticle Analyzer SZ-100V2 series."

[113] L. Sun *et al.*, "Controllable synthesis of silver nanoparticle aggregates for surface-enhanced raman scattering studies," *Journal of Physical Chemistry C*, vol. 115, no. 33, pp. 16295–16304, Aug. 2011, doi: 10.1021/jp205545g.

[114] A. Rath, F. Cunningham, and C. M. Deber, "Acrylamide concentration determines the direction and magnitude of helical membrane protein gel shifts," *Proc Natl Acad Sci U S A*, vol. 110, no. 39, pp. 15668–15673, Sep. 2013, doi: 10.1073/pnas.1311305110.

[115] M. A. El-Sayed, "Some interesting properties of metals confined in time and nanometer space of different shapes," *Acc Chem Res*, vol. 34, no. 4, pp. 257–264, 2001, doi: 10.1021/ar960016n.

[116] L. Jensen and G. C. Schatz, "Resonance Raman scattering of rhodamine 6G as calculated using time-dependent density functional theory," *Journal of Physical Chemistry A*, vol. 110, no. 18, pp. 5973–5977, May 2006, doi: 10.1021/jp0610867.

[117] P. K. Jain, K. S. Lee, I. H. El-Sayed, and M. A. El-Sayed, "Calculated absorption and scattering properties of gold nanoparticles of different size, shape, and composition: Applications in biological imaging and biomedicine," *Journal of Physical Chemistry B*, vol. 110, no. 14, pp. 7238–7248, Apr. 2006, doi: 10.1021/jp057170o.

[118] K. E. Sapsford, L. Berti, and I. L. Medintz, "Materials for fluorescence resonance energy transfer analysis: Beyond traditional donor-acceptor combinations," Jul. 10, 2006, *Wiley-VCH Verlag*. doi: 10.1002/anie.200503873.

[119] S. Keskin, E. Efeoğlu, K. Keçeci, and M. Çulha, "Label-free detection of proteins in ternary mixtures using surface-enhanced Raman scattering and protein melting profiles," *J Biomed Opt*, vol. 18, no. 3, p. 037007, Mar. 2013, doi: 10.1117/1.jbo.18.3.037007.

[120] M. Mapiour and A. Amira, "Critical Influences of Plasma pH on Human Protein Properties for Modeling Considerations: Size, Charge, Conformation, Hydrophobicity, and Denaturation," *Journal of Composites Science*, vol. 7, no. 1, Jan. 2023, doi: 10.3390/jcs7010028.

[121] R. R. Neubig, M. Spedding, T. Kenakin, and A. Christopoulos, "International Union of Pharmacology Committee on Receptor Nomenclature and Drug Classification. XXXVIII. Update on Terms and Symbols in Quantitative Pharmacology," Dec. 2003. doi: 10.1124/pr.55.4.4.

[122] D. I. Bioengineering, "DEPARTMENT OF CHEMISTRY NANOSERS MICROFLUIDICS PLATFORM FOR RAPID SCREENING FOR INFECTIOUS DISEASES MARIA JOÃO QUITOLES DE OLIVEIRA Master in Biotechnology," 2022.

[123] A. Bustamante *et al.*, "Blood Biomarkers to Differentiate Ischemic and Hemorrhagic Strokes," *Neurology*, vol. 96, no. 15, pp. E1928–E1939, 2021, doi: 10.1212/WNL.0000000000011742.

[124] A. Bustamante *et al.*, "Blood Biomarkers for the Early Diagnosis of Stroke: The Stroke-Chip Study," *Stroke*, vol. 48, no. 9, pp. 2419–2425, Sep. 2017, doi: 10.1161/STROKEAHA.117.017076.

[125] J. M. Romo-Herrera *et al.*, "Paper-based plasmonic substrates as surface-enhanced Raman scattering spectroscopy platforms for cell culture applications," Jun. 01, 2021, *Elsevier B.V.* doi: 10.1016/j.mtbio.2021.100125.

[126] T. Sun *et al.*, "iTRAQ based investigation of plasma proteins in HIV infected and HIV/HBV coinfected patients — C9 and KLK are related to HIV/HBV coinfection," *International Journal of Infectious Diseases*, vol. 63, pp. 64–71, Oct. 2017, doi: 10.1016/j.ijid.2017.08.006.

[127] O. G. Pandoli *et al.*, "Ultra-highly conductive hollow channels guided by a bamboo bio-template for electric and electrochemical devices," *J Mater Chem A Mater*, vol. 8, no. 7, pp. 4030–4039, Feb. 2020, doi: 10.1039/c9ta13069a.

AN APPENDIX

A.1 SERS Spectra of Possible Contamination of AgNS with MBA.

During this project, several batches of AgNS were synthesized, with some showing a red shift in the UV-Vis spectrum, potentially due to contamination with MBA from equipment used for AuNS synthesis. The SERS spectrum (Figure A1) confirmed the presence of MBA contamination, as illustrated in Figure A2.

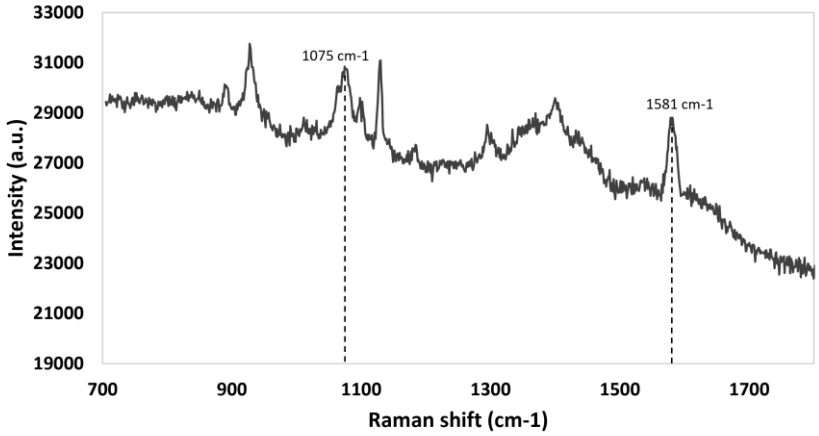

Figure A1. SERS spectrum of AgNS in aluminium foil.

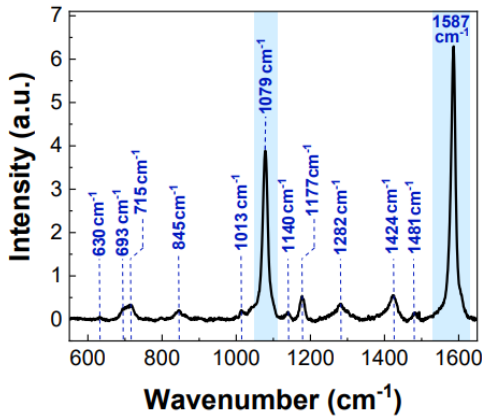

Figure A2. Raman Spectrum of MBA. Adapted from [122].

A2. Control SERS Spectra

To ensure that no other signals are influencing the obtained SERS spectra, it is important to include several controls, such as AgNS alone, the substrate used for sample placement, HSA alone, plasma alone, and the potassium phosphate buffer (KPB).

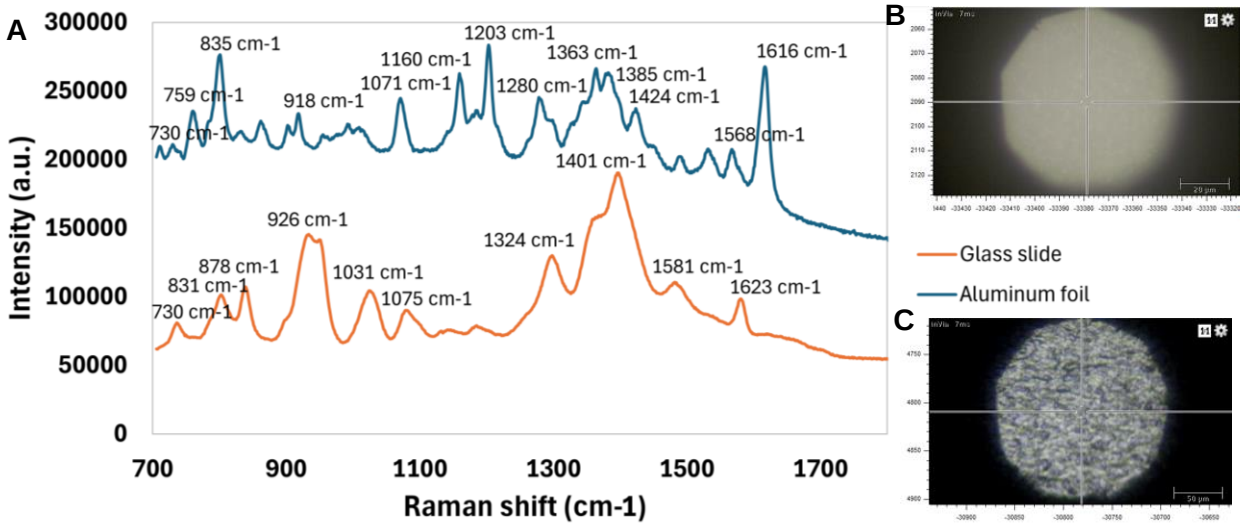

Figure A3. SERS spectrum of AgNS on glass slide (orange spectrum) and on aluminium foil (blue spectrum). **B**. Visible microscope image of AgNS on the glass slide**. C**. Visible microscope image of AgNS on aluminium foil substrate.

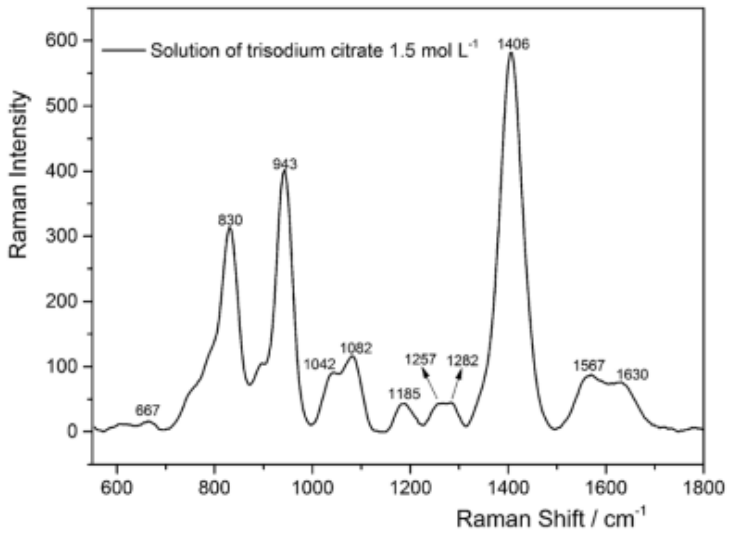

Figure A4. Raman spectra of aqueous solution of trisodium citrate. Adapted from [127].

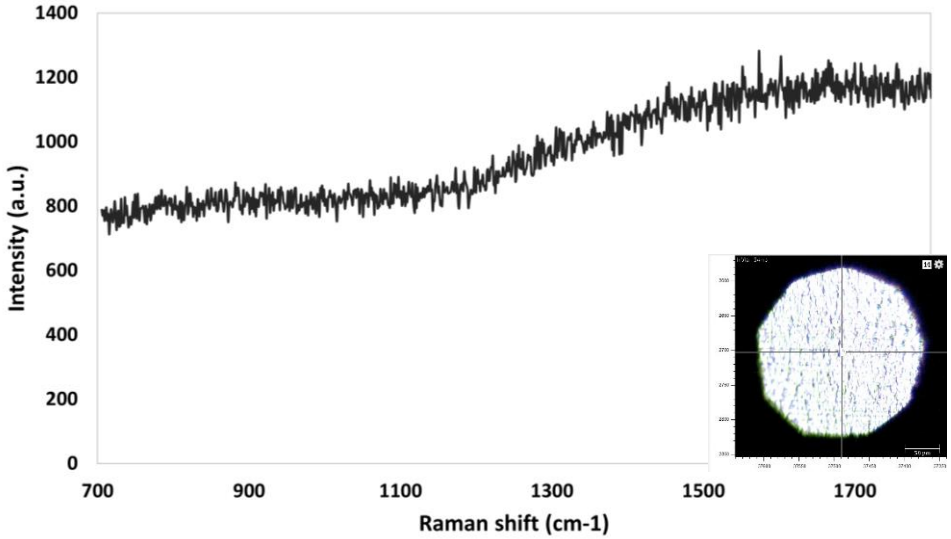

Figure A5. SERS spectrum of aluminium foil substrate and visible microscope image.

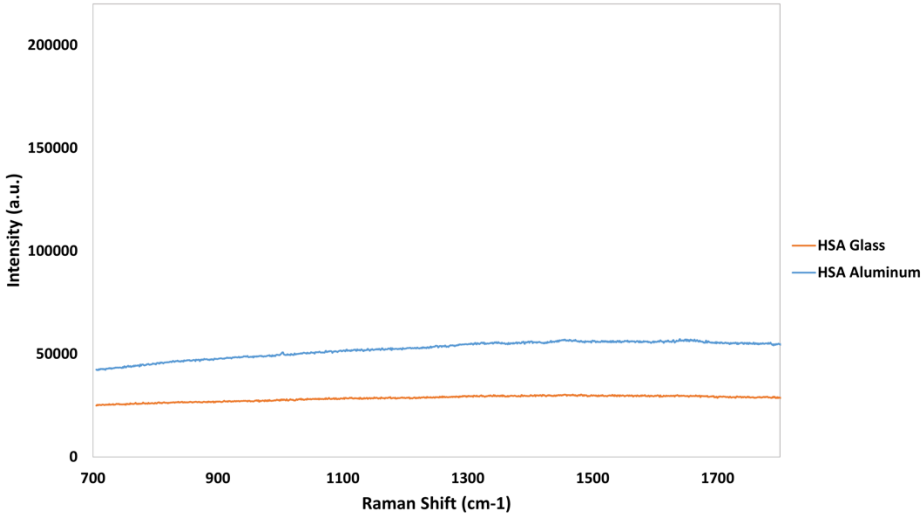

Figure A6. Raman spectrum of HSA on Aluminium foil (blue spectrum) and Raman spectrum of HSA on a glass slide (orange spectrum).

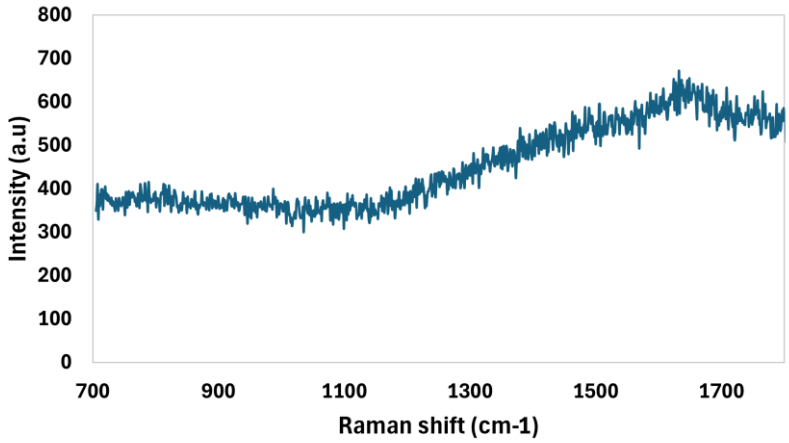

Figure A7. Raman spectrum of potassium phosphate (KPB) on aluminium foil.

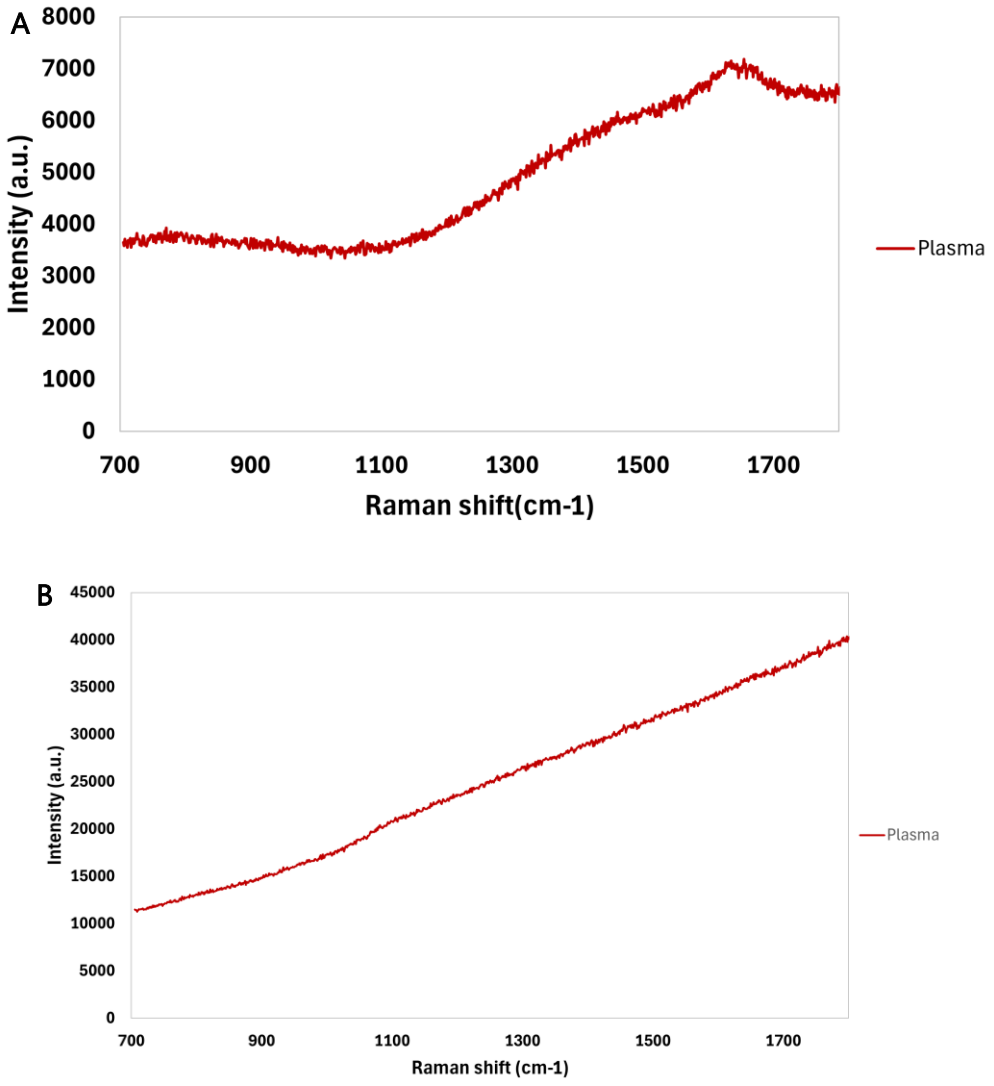

Figure A8. A. Raman spectrum of plasma (3.33 nM) on aluminium foil. **B** Raman spectrum of plasma (3.33 nM) on glass slide.

A3. DLS Data of Controls

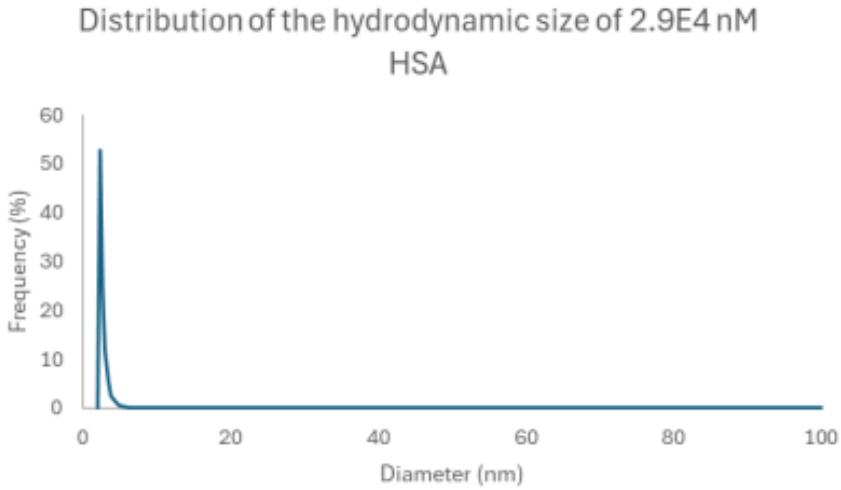

Figure A9. DLS data of HSA. Distribution of the hydrodynamic size.

A4. SERS Spectra of the Six Plasma:AgNS ratios

Due to the difference of intensity, in Figure A8 the six plasma bioconjugates are presented.

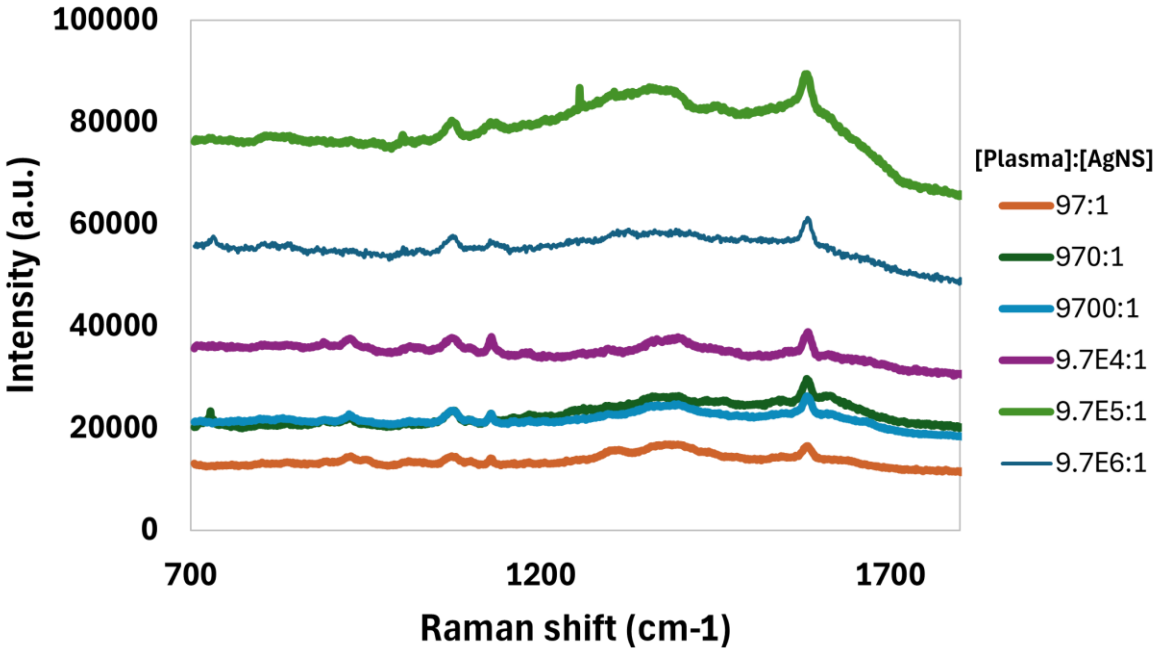

Figure A10. SERS spectra of the six plasma bioconjugates, ranging from 97:1 to 9.7E6:1 plasma:AgNS.

A5. Raman Spectra of paper substrates.

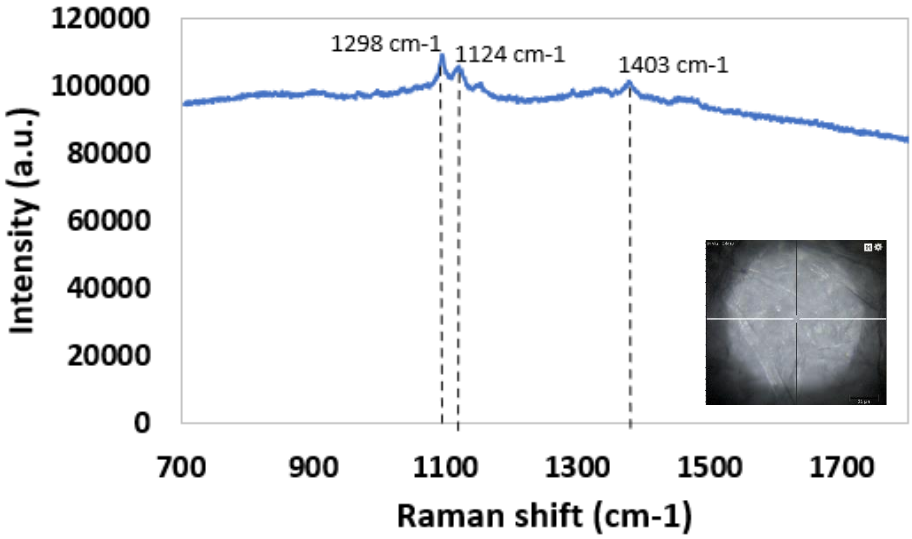

Figure A11. Raman spectrum of photocopy paper with wax framed wells.

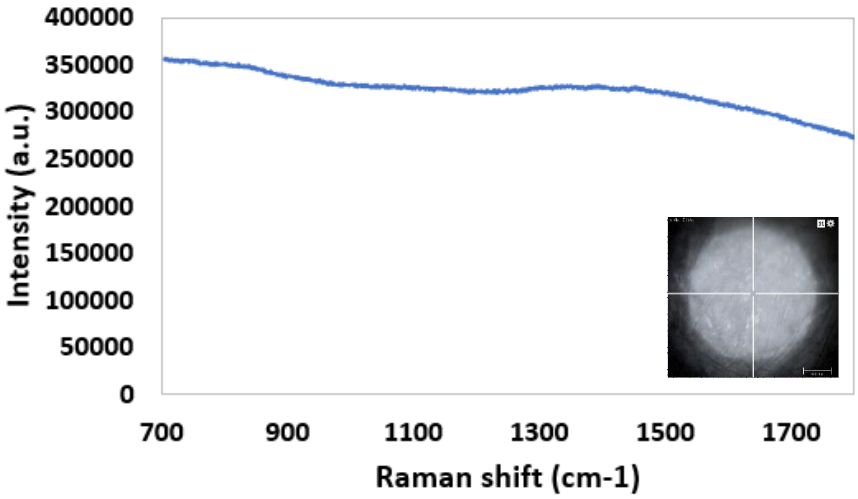

Figure A12. Raman spectrum of Whatman No.1 paper with wax framed wells.

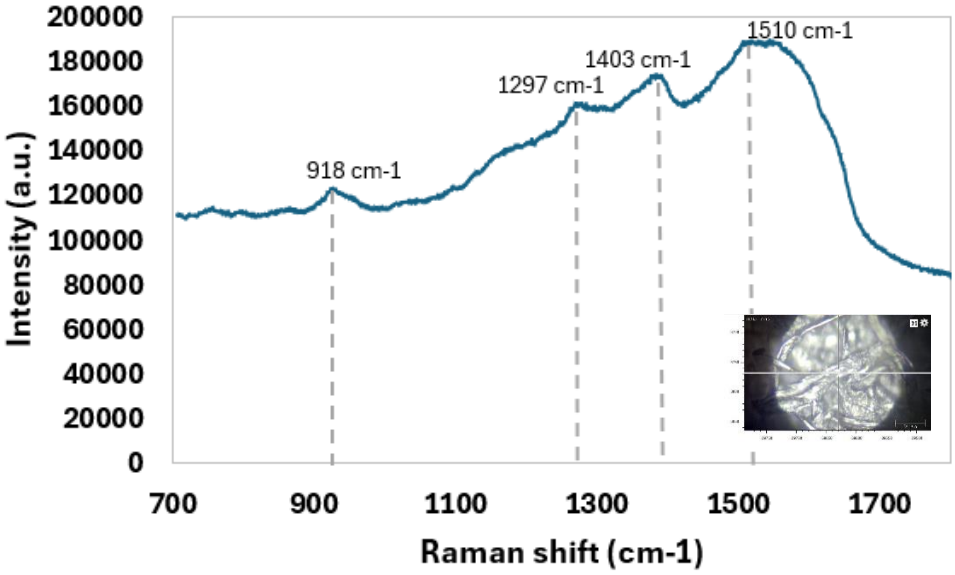

Figure A13. SERS spectrum of photocopy paper wells containing AgNP on the wells.

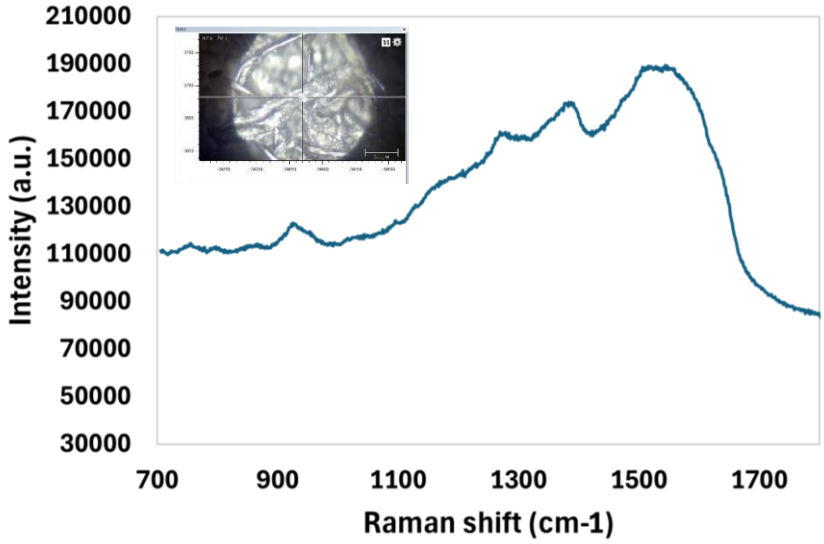

Figure A14. SERS Spectrum of Whatman No.1 paper wells containing AgNP on the wells.

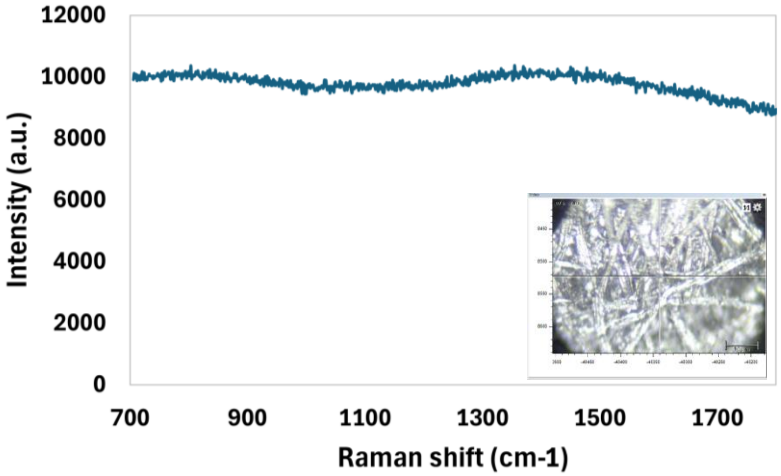

Figure A15. Photocopy paper with wells and with 100 nm Mo deposition above it.

A6. DLS analysis of 10 HSA:AgNS Ratios from Initial Screening

The hydrodynamic size analysis of ten distinct ratios of HSA bioconjugates is presented in this section. The hydrodynamic sizes for these ratios, as shown in Figure A16, indicate that the bioconjugates are mostly in the tens to hundreds of nanometers range, with a noticeable increase in size as the HSA:AgNS ratio increases. This suggests the potential for some aggregation among the bioconjugates, particularly at higher HSA:AgNS ratios, where the presence of more protein may enhance interparticle interactions, leading to aggregation. The largest hydrodynamic size, averaging 135 nm, is observed in the bioconjugates at the highest HSA ratio (1000:1 HSA:AgNS), which is significantly larger than the AgNS control (90 nm). This trend is likely due to the increased formation of protein corona surrounding the nanoparticles. Additionally, the asymmetric morphology of the AgNS further complicates the accurate quantification of the HSA forming the protein corona, highlighting the influence of nanoparticle shape on aggregation behavior.

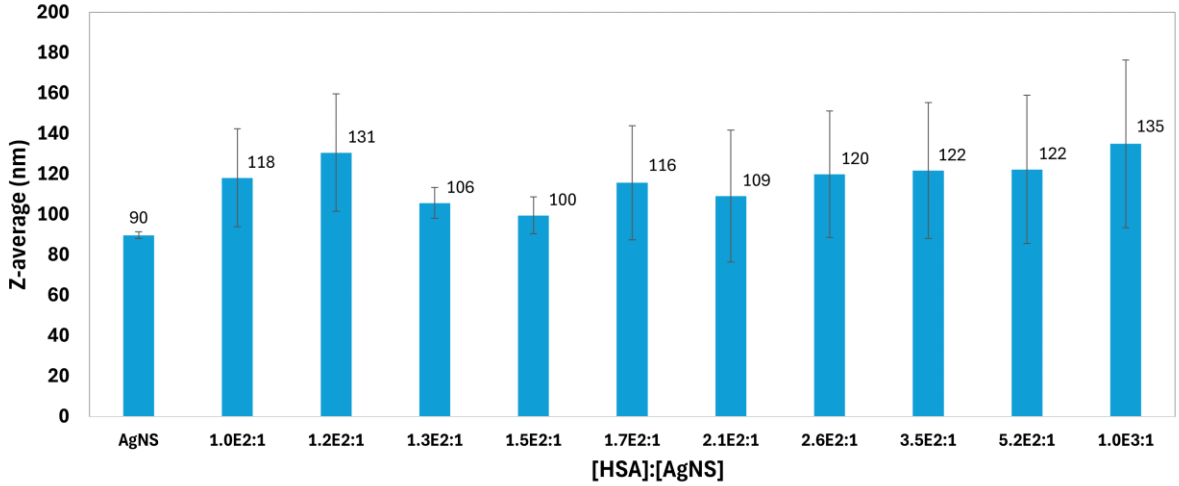

Figure A16. Z-average of HSA and AgNS at varying HSA:AgNS ratios.

Table A1. Polydispersity index (PDI) of AgNS and Plasma bioconjugates.

[HSA:AgNS]	Polydispersity index (PDI)					Average	SD
0 (AgNS alone)	0.108	0.257	0.372	0.294	0.053	0.22	0.12
100:1	0.049	0.203	0.109	0.311	0.272	0.19	0.10
120:1	0.185	0.197	0.073	0.257	0.13	0.17	0.06
130:1	0.273	0.122	0.105	0.139	0.281	0.18	0.08
150:1	0.106	0.255	0.106	0.115	0.116	0.14	0.06
170:1	0.02	0.196	0.251	0.337	0.178	0.20	0.10
210:1	0.129	0.27	0.02	0.109	0.274	0.16	0.10
260:1	0.229	0.119	0.021	0.2	0.229	0.16	0.08
350:1	0.076	0.021	0.322	0.295	0.224	0.19	0.12
520:1	0.112	0.257	0.055	0.021	0.109	0.11	0.08
1000:1	0.256	0.477	0.021	0.094	0.022	0.17	0.17

Further insights into the homogeneity of these bioconjugates are provided by the PDI values, as shown in Table A1. The PDI values reveal a broad range of sample homogeneity, from very low (0.02) to moderately high (0.477). For example, the 10003:1 HSA:AgNS ratio exhibits a high PDI of 0.477, indicating a wide size distribution and substantial aggregation, likely due to uneven corona formation caused by excessive protein coverage. In contrast, the 170:1 HSA:AgNS ratio has a low PDI of 0.02, signifying a more uniform size distribution with less aggregation, which is advantageous for stability and reproducibility in SERS applications.

The bar graph in Figure A17 presents the zeta potential values for various HSA:AgNS bioconjugate ratios, ranging from 100:1 to 1000:1 HSA:AgNS, as well as a control sample of AgNS alone. The zeta potential for the bare AgNS shows a highly negative value of -72 mV, indicating strong electrostatic stability. However, upon the addition of HSA, the zeta potential becomes less negative across all bioconjugate ratios, suggesting a partial neutralization of surface charge due to protein adsorption.

Notably, the ratio 130:1 HSA:AgNS shows the least negative zeta potential at -12 mV, which might indicate significant protein coverage and a potential shift in particle behavior. The other ratios (100:1, 120:1, and 150:1) maintain moderately negative values in the range of -45 to -54 mV, while higher HSA concentrations (170:1 and beyond) yield zeta potential between -57 mV and -64 mV, indicating relatively stable bioconjugates, although less stable than the AgNS alone.

These results suggest that increasing HSA concentrations generally result in more negative zeta potentials, except for the 130:1 HSA:AgNS ratio, which exhibits a significant deviation from the trend. This may lead to changes in colloidal stability and particle interaction dynamics due to the varying degrees of protein adsorption and surface coverage.

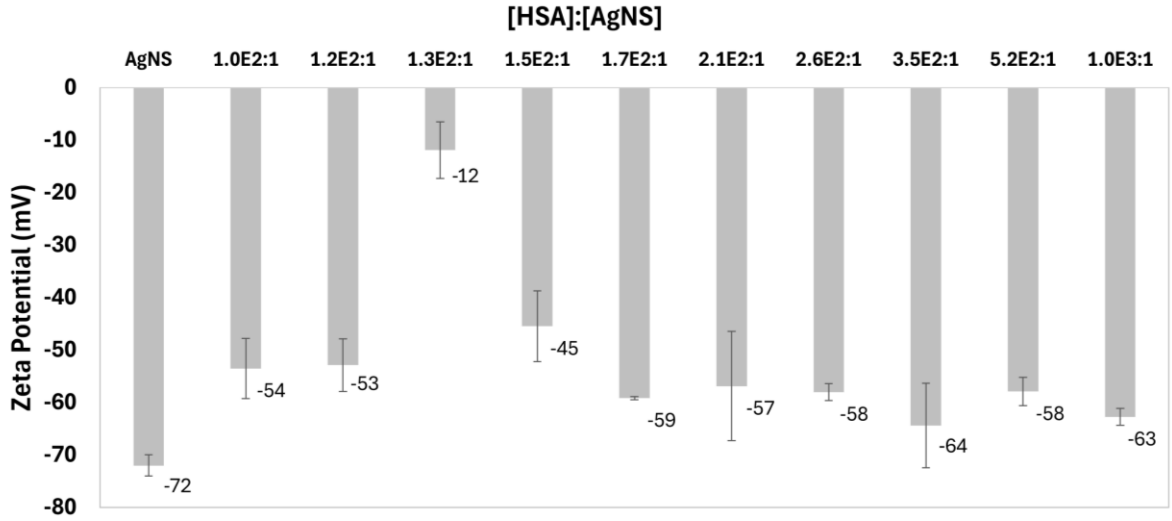

Figure A17. Zeta Potential (mV) of HSA:AgNS bioconjugates of ten different ratios.

A7. DLS Analysis of 10 Plasma:AgNS Ratios from Initial Screening

Figure A18 displays the Z-average (hydrodynamic diameter) measurements for bare AgNS and various plasma:AgNS ratios. For comparison, the Z-average value for the bare AgNS is 90 nm. Among the plasma-conjugated samples, the highest Z-average value of 139 nm is observed for the 60:1 plasma:AgNS ratio, indicating more extensive protein binding or potential aggregation, leading to larger particle sizes. In contrast, samples such as 75:1 and 200:1 plasma:AgNS exhibit smaller increases in Z-average, measuring 105 nm and 102 nm, respectively, suggesting more stable dispersions or less extensive bioconjugation.

Other plasma-conjugated samples, including ratios 660:1, 1200:1, and 850:1 plasma:AgNS, show Z-average values ranging from 130 to 137 nm, indicating similar levels of bioconjugation with no significant changes in particle size. The variations in Z-average across different plasma:AgNS ratios underscore the influence of plasma concentration on the bioconjugation process. Higher Z-average values for ratios like 1200:1 and 60:1 plasma:AgNS may indicate the onset of aggregation, or a saturation point where additional plasma does not significantly increase particle size. Conversely, lower Z-average values for ratios such as 75:1 plasma:AgNS suggest that certain plasma concentrations may produce more stable bioconjugates with minimal size increase.

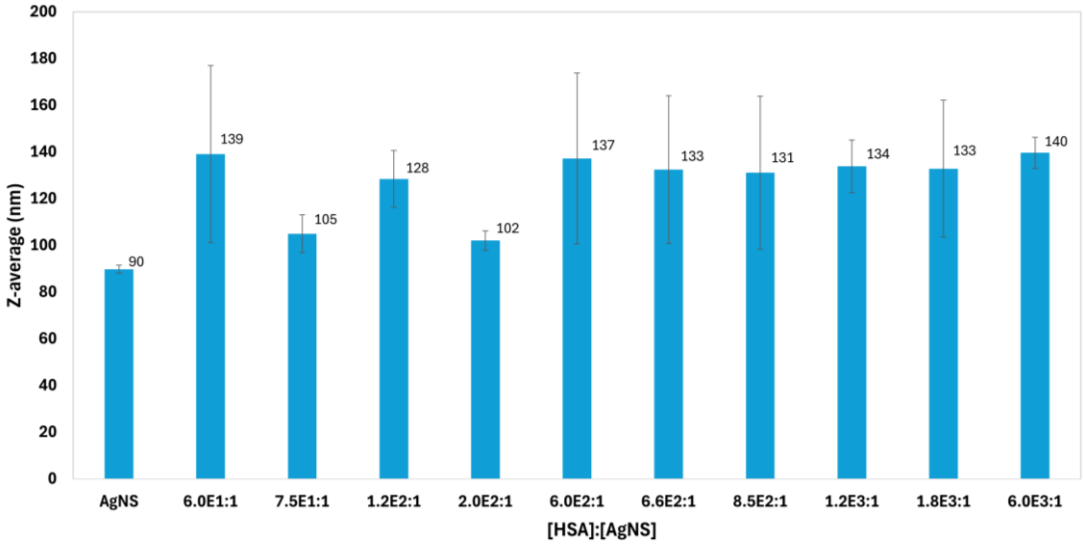

Figure A18. Z-average of Plasma and AgNS at varying Plasma:AgNS ratios.

Table A2. Polydispersity index (PDI) of AgNS and Plasma bioconjugates.

[Plasma]:[AgNS]	Polydispersity index (PDI)					Average	SD
0 (AgNS alone)	0.108	0.257	0.372	0.294	0.053	0.22	0.12
60:1	0.274	0.308	0.022	0.209	0.021	0.17	0.12
75:1	0.116	0.294	0.141	0.278	0.208	0.21	0.07
120:1	0.081	0.075	0.091	0.154	0.014	0.08	0.04
200:1	0.242	0.294	0.006	0.257	0.198	0.20	0.10
600:1	0.023	0.125	0.081	0.079	0.123	0.09	0.04
660:1	0.071	0.359	0.123	0.099	0.633	0.26	0.21
850:1	0.349	0.183	0.086	0.022	0.082	0.14	0.11
1200:1	0.285	0.001	0.061	0.071	0.089	0.10	0.10
1800:1	0.028	0.121	0.112	0.366	0.022	0.13	0.13
6000:1	0.159	0.178	0.281	0.206	0.032	0.17	0.08

DLS analysis highlights the importance of optimizing plasma:AgNS ratios to achieve the desired bioconjugate size, which is crucial for applications requiring specific particle sizes for optimal performance. The PDI of the AgNS and plasma bioconjugates is summarized in Table A2, reflecting the uniformity of particle size distribution across the samples.

The AgNS sample exhibits moderate polydispersity with PDI values ranging from 0.053 to 0.372 plasma:AgNS, indicating some size variation. In certain conditions, plasma-to-AgNS ratios such as 1200:1 and 660:1 plasma:AgNS yield low PDI values, pointing to more uniform particle sizes. In other conditions, higher PDI values are observed, indicating more heterogeneous size distributions.

Figure A19 presents the zeta potential measurements for AgNS and plasma:AgNS bioconjugates at various plasma:AgNS ratios. The negative values

suggest that all samples exhibit a negative surface charge, with pure AgNS showing the most negative zeta potential (-77 mV).

As the plasma:AgNS ratio increases, the zeta potential becomes less negative, indicating a decrease in the surface charge magnitude, which suggests that plasma proteins are adsorbing onto the AgNS surface and neutralizing part of the surface charge. Ratios such as 60:1, 75:1, and 120:1 plasma:AgNS demonstrate a moderate decrease in zeta potential (-54 mV and -60 mV), while higher ratios (850:1, 1800:1) show a more significant shift towards less negative values (-30 mV and -31 mV).

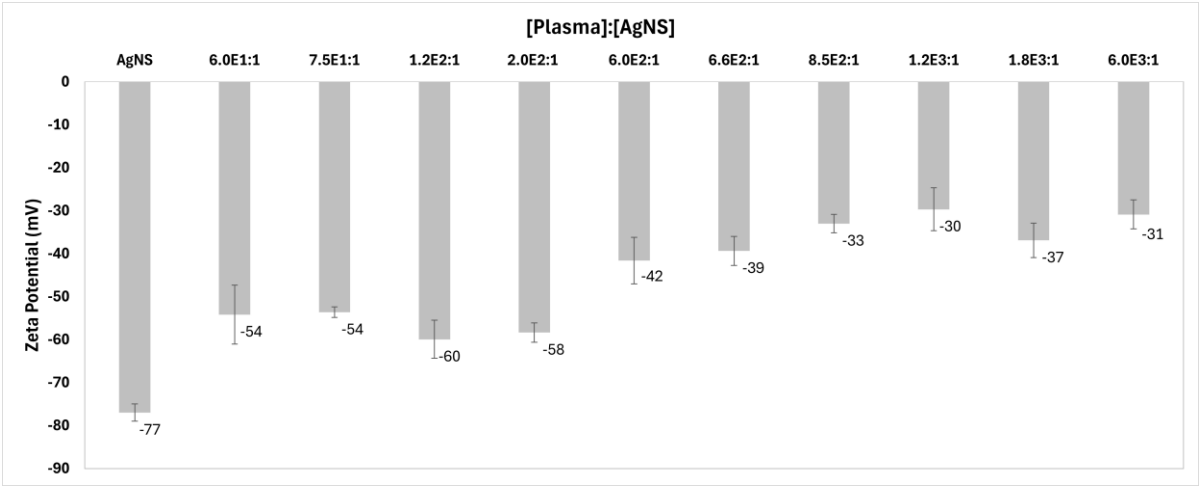

Figure A 19. Zeta potential (mV) of the ten plasma:AgNS ratios.

A8. SDS-PAGE calibration curve

Calibration curve obtained from the SDS-PAGE, using the MM (low weight) as standards for building the calibration curve.

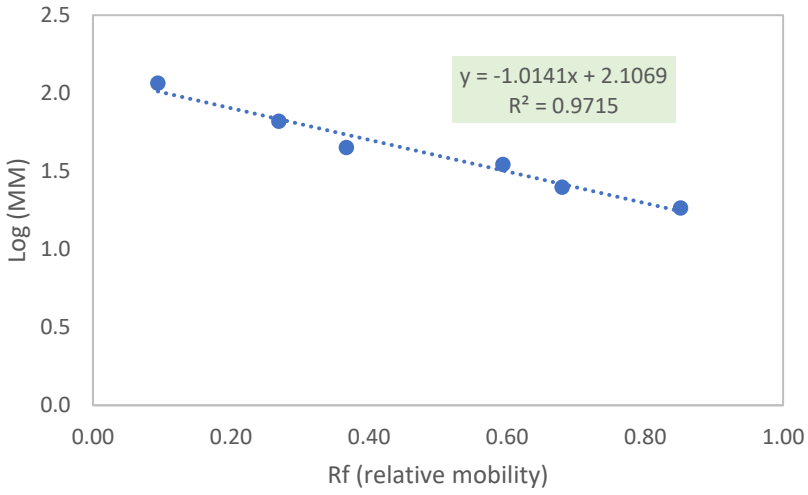

Figure A20. Calibration curve obtained from the SDS-PAGE for plasma and plasma without albumin samples.

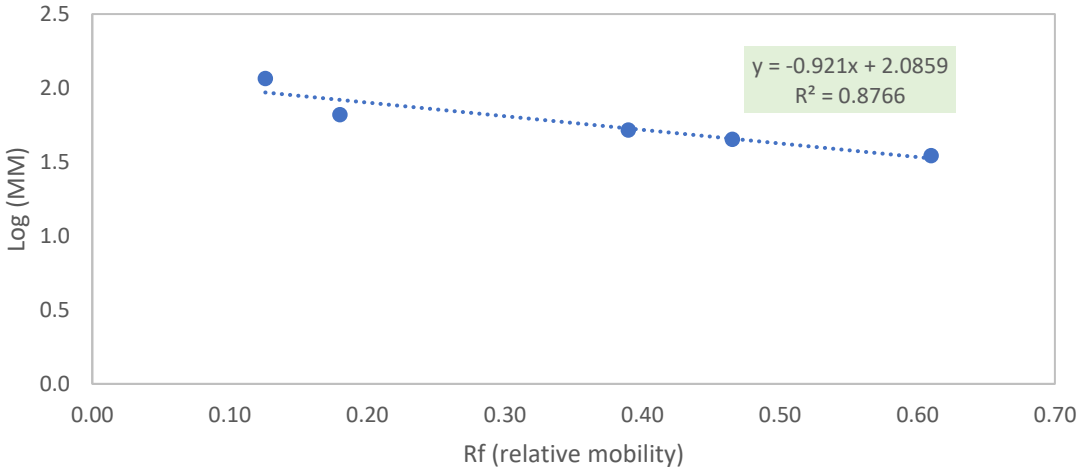

Figure A21. Calibration curve obtained from the SDS-PAGE for the plasma:AgNS bioconjugate after 3h and overnight incubation.

A9. Raman control of Plasma without Albumin

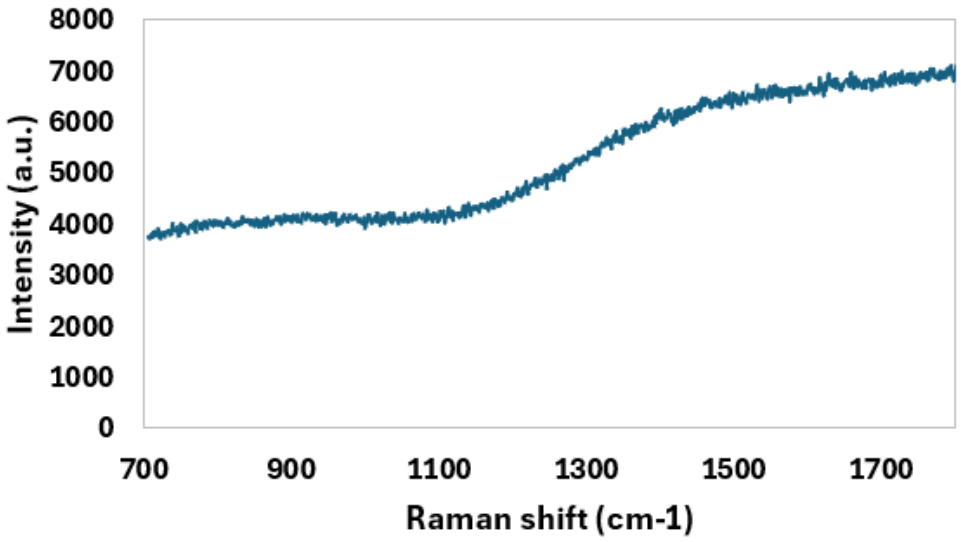

Figure A22. Raman Spectrum of plasma without albumin on aluminium foil substrate.

A10. DLS of GFAP:AgNS

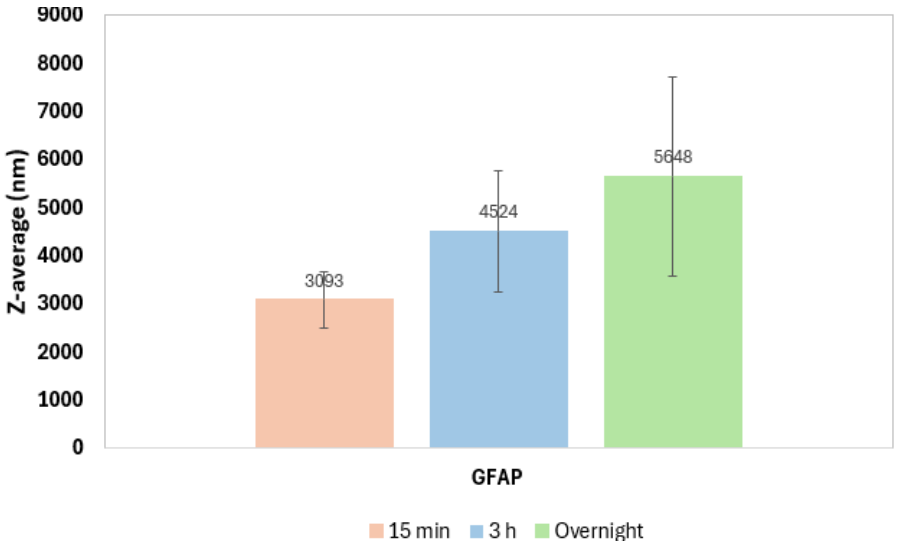

Figure A23. Z-average (nm) of GFAP:AgNS over time.

Table A3. Polydispersity index (PDI) of GFAP:AgNS over time.

	Polydispersity index (PDI)					Average	SD
GFAP 15 min	0.355	0.283	0.176	0.264	0.328	0.28	0.06
GFAP 3h	0.257	0.346	0.323	0.352	0.422	0.34	0.05
GFAP over	0.662	0.616	0.48	0.605	0.143	0.50	0.19